Nieuwe methoden voor lichtsturing en aanpasbare lenzen met vloeibare kristallen

New Approaches to Liquid Crystal Beam-Steering and Tunable Lensing

Oliver Willekens

Promotoren: prof. dr. ir. J. Beeckman, prof. dr. ir. K. Neyts
Proefschrift ingediend tot het behalen van de graad van
Doctor in de ingenieurswetenschappen: fotonica

UNIVERSITEIT
GENT

Vakgroep Elektronica en Informatiesystemen
Voorzitter: prof. dr. ir. R. Van de Walle
Faculteit Ingenieurswetenschappen en Architectuur
Academiejaar 2016 - 2017

ISBN 978-90-8578-968-0
NUR 924, 959
Wettelijk depot: D/2017/10.500/3

Ghent University
Faculty of Engineering and Architecture
Liquid Crystals and Photonics

Promoters

Prof. Dr. Ir. J. Beeckman

Ghent University, Department of Electronics and Information Systems,
Liquid Crystals and Photonics (LCP),

Prof. Dr. Ir. K. Neyts

Ghent University, Department of Electronics and Information Systems,
Liquid Crystals and Photonics (LCP),

Other Members of the Examination Committee

Prof. Dr. Ir. Patrick De Baets *Chairman*

Ghent University,
Department of Electrical Energy, Systems and Automation.

Prof. Dr. Ir. Herbert De Smet *Secretary*

Ghent University,
Department of Electronics and Information Systems.

Prof. Dr. Ir. Bart Kuyken

Ghent University,
Departement of Information Technology.

Prof. Dr. Ir. Ing. Michael Vervaeke

Vrije Universiteit Brussel (VUB),
Brussels Photonics Team (B-Phot).

Prof. Dr. Tim Wilkinson

University of Cambridge,
Department of Engineering.

A Dissertation Submitted in Partial Fulfillment of the Requirements for the Degree of
Doctor of Photonics Engineering
Academic Year 2016–2017

Copyright

Special Thanks

While a dissertation is usually written by a single person, many people will have had a hand in all the work presented in the document. Throughout my years within the Liquid Crystals and Photonics research group, I have received support from many people, support that can be as simple as a place to vent research-related frustrations or as extensive as contributions to fabricated devices. I am deeply thankful for that support and wish to put these contributors in the spotlight.

For starters, Jeroen and Kristiaan, my promotor and co-promotor. I am very grateful to you both: not only have you given me the chance to perform challenging scientific research in a well-equipped technological environment, but you have given me the freedom to direct my own focus. Through your many years as promotors, you have also obtained the skill to direct that focus, when required. I saw your gentle nudges to steer the projects in the right direction, to obtain publish-worthy output. I appreciate the many times you have come to the lab to discuss my findings and discuss with me the subsequent steps. Thank you for your valuable time.

A lot of scientific support has also come from the members of the LCP research group, former and current. Glenn, you have been my mentor at the start. You taught me how to process liquid crystal cells properly and your eye to detail is unfailing. You never hesitated to explain the way things work and you could see certain links so easily, something for which I admire you. I consider you a genius. Our conversations about proving handedness, working out transmission spectra models and rainbow color maps have been both enriching and enjoyable. Have you noticed I snuck in a few rainbow color maps in this thesis, by the way? Properly used, of course. John, your contributions to this thesis in terms of processing are without doubt enormous. Thanks to your hard and time-consuming work, I received excellent samples with which I could demonstrate a technology that has never been seen before. You are an amazingly hard worker and your ability to do cleanroom work so many hours in a row is truely impressive. I am proud to share a paper with

you. Toon and Woesty, you have imparted your knowledge of cleanroom processes and mask design with me. While that was useful, it is not what I will remember you for: you two were terrific assets to the group. Helpful, knowledgeable and sociable, you two have made those initial years very enjoyable. “Uncle boss” Filip, while you were not my promotor, you have guided me on many occasions as well. I appreciate you taking time from your own schedule to talk to someone who is further away from your field. The people who work under you, appreciate you, like a friend, as do I. Stijn, when Toon left you had to pick up many of his responsabilities. I think you did a great job, and came up with several nice innovations to our group’s tooling, as well as our website. Filip Strubbe, thank you for the time you always made to explain me things about finite elements. It gave me great pleasure to see that you took your time to explain things, often with pen and paper. Inge, I respect your ability to separate business and pleasure. When you are at the office, you are *at the office*. Moreover, your consideration for people’s schedules is highly professional too. Michiel, I learnt a few things from the way you negotiated with manufacturers. Thanks for prioritizing the metallization of a good number of samples near the end of my PhD and for not only being a colleague, but also a friend.

Aside from the scientific support, I have also received moral support from the members of the group — doing a PhD can be quite stressy and demotivating at times! Hearing someone say “you’re doing fine” can be uplifting — thanks Varsenik, Serena, Manoj and a couple of the others, you know who you are. Caspar, thanks for providing amusing tidbits anytime I entered the “tweezer office”. Samira, whenever something not work-related was troubling me, I knew I could come to you. Your gentle demeanor and wisdom are there for anyone who seeks you out, and I know several who have found in you their confidante. To Xiaoning, whom I often describe as my protégé, I have seen such a formidable growth in you, both professionally as well as personally. The greatest gift you have given me was your trust. “Can I talk to you?” With those words you have made me aware of a new role for me in our group as well.

When I look beyond the support of the people I have known in the LCP research group, but within our department, I cannot overlook Pankaj. Finding someone locally who can be a sort of sparring partner for blue phase related topics has been such a relief. Those talks have helped me in understanding

the matter much faster. Pankaj, you are also a great inspirational source: you came up with so many things to try, to investigate, but you never lost your down-to-earth mentality. I am proud to be listed on one of your articles.

Karen and Marnix, your logistic support has allowed me to focus on my research. Ronny and Michiel, I hope that whenever you two saw one of my e-mails coming in, you did not sigh. Your technical support has made it easier for me to run processes from home when I was too ill to come to work or when working at a different computer was just too cumbersome. I was able to speed up many things thanks to you two.

Looking outside of the university, I have received moral support from a whole slew of people. Three of them have gone above and beyond moral support: my good friend David, I want to express my sincerest thanks to you. You displayed genuine interest in the contents of my research and I enjoyed talking about it with you anytime I went to meet up with the gang. I also want to thank you once more for making the time to render the lens schematic and discussing improvements to it with me, after your working hours. My dear mother, you are in this list too. You may not think so, but your support throughout these years has helped me *so much*. You are one of my confidantes and a terrific counselor. Thanks for making my life easier those many weekends where I was working hard and had little time for anything else. Finally, my darling, Christina. Our paths crossed at a summer school on a tangent between our studies. Because of the similarities between our studies, we understand the adventures that we face. It feels great to be able to talk with you about work and knowing that you understand, or to share ideas and doing scientific experiments. You have helped me in so many ways during the last months of my PhD, you have truely been a tremendous support. I know those months were not easy for you too. Worse sleep and a housemate who is physically there, but mentally is not. You have sacrificed and done so much for me. From the bottom of my heart, thank you.

Oliver Willekens
Jan. 2nd, 2017

Table of Contents

List of Figures

List of Tables

List of Publications

The author of this work has contributed to scientific research in more than what is presented in this dissertation. Some of those contributions have lead to publications in peer-reviewed journals and technical papers that have been presented at conferences, both of which are listed below, together with publications that are the direct result of this work.

Journal articles

1. **Willekens, O.**, X. Jia, M. Vervaeke, X. Shang, T. Baghdasaryan, *et al.*, "Reflective liquid crystal hybrid beam-steerer", *Optics Express*, vol. 24, no. 19, pp. 21 541–21 550, 2016. [Online].
2. **Willekens, O.**, J. Puthenparampil George, K. Neyts, and J. Beeckman, "Ferroelectric thin films with liquid crystal for gradient index applications", *Optics Express*, vol. 24, no. 8, pp. 8088–8096, 2016. [Online].
3. Dadalyan, T., R. Alaverdyan, I. Nys, Z. Ninoyan, **Willekens, O.**, *et al.*, "Tuning the lasing wavelength of dye-doped chiral nematic liquid crystal by fluid flow", *Liquid Crystals*, p. 7, 2016. [Online].
4. Claus, H., **Willekens, O.**, O. Chojnowska, R. Dabrowski, J. Beeckman, *et al.*, "Inducing monodomain blue phase liquid crystals by long-lasting voltage application during temperature variation", *Liquid Crystals*, vol. 43, no. 5, pp. 688–693, 2016. [Online].
5. Joshi, P., J. De Smet, X. Shang, **Willekens, O.**, D. Cuypers, *et al.*, "Long term stability of polymer stabilized blue phase liquid crystals", *Journal of Display Technology*, vol. 11, no. 9, pp. 703–708, 2015. [Online].
6. Shang, X., J. Y. Tan, **Willekens, O.**, J. De Smet, P. Joshi, *et al.*, "Electrically controllable liquid crystal component for efficient light steering", *IEEE Photonics Journal*, vol. 7, no. 2, p. 14, 2015. [Online].
7. Mantashyan, P., R. Drampyan, J. Beeckman, **Willekens, O.**, and K. Neyts, "Optical induction of bessel-like lattices in methyl-red doped liquid crystal cells", *Optics Communications*, vol. 338, pp. 467–472, 2015. [Online].

Conference proceedings

1. **Willekens, O.**, K. Neyts, and J. Beeckman, "Liquid crystal devices with continuous phase variation based on high-permittivity thin films", in *SPIE Proceedings; Volume 9769; Emerging Liquid Crystal Technologies XI; Electro-Optical Processes*, Chien, L.-C.,

D. J. Broer, H. Kikuchi, and N. V. Tabiryan, Eds., vol. 9769, United States of America, California, San Francisco, Moscone Center, 2016, 97690P:97690P-1–97690P:97690P-7. [Online].

2. **Willekens, O.**, J. Puthenparampil George, K. Neyts, and J. Beeckman, "Pzt-based transmissive liquid crystal lens approach", in *SID Symposium Digest of Technical Papers*, vol. 46, ″het Pand″, Ghent, Belgium, 2015, S1.3:7–S1.3:7. [Online].

3. **Willekens, O.**, J. Puthenparampil George, K. Neyts, and J. Beeckman, "High dielectric constant materials for low power liquid crystal tunable lenses", in *FEA Research Symposium 2015, Abstracts*, Zebrastraat, Ghent, 2015.

4. Shang, X., J. De Smet, P. Joshi, D. Cuypers, J. Y. Tan, *et al.*, "Switchable liquid crystal devices for efficient light steering", in *SID Symposium Digest of Technical Papers*, vol. 46, Ghent, Belgium: Society for Information Display, 2015, S3.4:16–S3.4:16.

5. Cuypers, D., X. Shang, J. De Smet, J. Pankaj, J. Beeckman, *et al.*, "Liquid crystal beam steering components for display applications", in *15th International Meeting on Information Display, Abstracts*, Daegu, Korea: KIDS, SID, 2015, pp. 246–246.

6. Neyts, K., **Willekens, O.**, I. Nys, Y. Xie, M. Mohammadimasoudi, *et al.*, "Liquid crystal patterns originating from structured alignment", in *Photoalignment and Photopatterning in Soft Materials : Basic Understanding and Applications, Abstracts*, Hong Kong, China: Hong Kong University of Science and Technology, 2014, pp. 7–7.

7. **Willekens, O.**, J. Beeckman, and K. Neyts, "Electrically tunable and polarization independent liquid crystal lens", in *14th FEA PhD Symposium, Abstracts*, Ghent, Belgium, 2013.

8. **Willekens, O.**, J. Beeckman, and K. Neyts, "Modelling the electro-optic behavior of liquid crystal lenses with multiple electrodes", in *XX Conference on Liquid Crystals, Abstracts*, Mikołajki, Poland, 2013.

9. Beeckman, J., S. Lambert, W. De Cort, **Willekens, O.**, K. Neyts, *et al.*, "Trimming of photonic components", in *13th International Symposium on Colloidal and Molecular Electrooptics, Abstracts*, Ghent, Belgium, 2012.

10. Verstringe, T., P. Van Torre, I. Nys, **Willekens, O.**, K. Neyts, *et al.*, "Image recognition controlled usb multichannel liquid crystal driver", in *Proceedings of the International Liquid Crystal Conference, 2016*, United States of America, Ohio, Kent State University, 2016.

11. Beeckman, J., **Willekens, O.**, J. Puthenparampil George, J. Xiaoning, and K. Neyts, "Liquid crystals on ferroelectric thin films", in *Molecular Crystals and Liquid Crystals, volume to be determined*, United States of America, Ohio, Kent State University, 2016.

12. Beeckman, J., **Willekens, O.**, X. Jia, J. Puthenparampil George, and K. Neyts, "Bridging the electrode gap with ferroelectric thin films", in *Workshop on Liquid Crystals for Photonics: Book of Abstracts*, Slovenia, Ljubljana, Jozef Stefan Institute, 2016.

Samenvatting

Vele ontdekkingen gebeuren bij toeval.

In 1888 deed Friedrich Reinitzer, een Oostenrijkse plantkundige, eeen toevallige ontdekking. Terwijl hij cholesteryl benzoaat bestudeerde, een stof die hij extraheerde uit wortelen, stelde hij een merkwaardige overgang tussen de vaste en vloeibare aggregatietoestand van de stof vast. Die observatie was de start van een onderzoeksdiscipline zonder dewelke onze wereld er vandaag helemaal anders zou uitzien.

Sinds hun ontdekking worden vloeibare kristallen bestudeerd voor hun unieke eigenschappen. Die eigenschappen hebben tot het ontstaan van een hele reeks toestellen geleid: we vinden ze terug in bijvoorbeeld onze uurwerken, thermometers, mobiele apparaten en beeldschermen. De lijst met toepassingen wordt elk jaar langer. De beeldschermindustrie levert een belangrijk bijdrage aan onderzoek naar vloeibare kristallen. Met de komst van 3D-cinema is er nood aan beeldschermen die sneller zijn en meer functionaliteit hebben: stereoscoop zicht vereist dat elk oog een lichtjes verschillend beeld te zien krijgt. Voor een realistische 3D-ervaring moeten de beelden die onze ogen waarnemen ook afhangen van de hoek waaronder we kijken. Een beeldscherm zou daarom in staat moeten zijn om verschillende beelden in verschillende richtingen te sturen en idealiter zelfs wanneer kijkers rond het scherm bewegen: een display moet licht in de correcte richting kunnen “sturen”.

De afgelopen decennia hebben toepassingen voor lichtsturing hun opmars gemaakt in verscheidene toepassingsdomeinen. Projectiesystemen, multiplexers voor telecommunicatie en optische netwerken zijn voorbeelden van toepassingen waar snelle en nauwkeurige controle over de richting waarin licht propageert nodig is. Apparaten die licht kunnen sturen en gebaseerd zijn op vloeibare kristallen hebben tragere, mechanische lichtsturingsapparaten vervangen in een reeks domeinen, zoals gezondheidszorg en biologie, en zullen dit blijven doen omwille van hun unieke eigenschappen en het voortdurende onderzoek ernaar in de scheikunde en natuurkunde, onderzoek dat gedreven

wordt door onze drang om huidige technologieën te verbeteren en door onze maatschappelijke noden.

In dit werk wordt een overzicht gegeven van hedendaagse lichtsturings- en lenstechnologieën gebaseerd op vloeibare kristallen, en hun beperkingen. Veelbelovend onderzoek wordt momenteel gevoerd naar polarizatiegratings, toestelletjes die steunen op de eigenschappen van vloeibare kristallen en fotoalignering. Onze aandacht gaat uit naar lichtsturingstechnologieën waar een gradiënt in de optische padlengte (OPL) van een lichtgolf, die door het vloeibaar kristal propageert, wordt geïnduceerd.

Om het toepassingspotentieel van lichtsturingscomponenten gebaseerd op vloeibare kristallen te verbreden, wordt een nieuw fabricageproces gehanteerd waarin microscopisch gestructureerde optische substraten snel kunnen worden nagemaakt op basis van “embossing”, of blinddruk. Fotoalignering, een recent ontwikkelde contactloze aligneringstechnologie voor vloeibare kristallen, wordt gebruikt om een homogene alignering van het vloeibaar kristal op de microgestructureerde substraten te bekomen. Deze microstructuren vormen, omwille van hun “blazed grating”-vorm, een elegante oplossing van het probleem om een gradiënt in de OPL te bekomen. Complexe elektrische sturingsmechanismen worden op deze manier vermeden. De hoekafwijking van een lichtbundel invallend op deze apparaten, wordt analytisch berekend, zowel in transmissie als in reflectie, en het wordt aangetoond dat deze proportioneel is met het product van de helling van de grating en de dubbelbrekendheid van het vloeibaar kristal. Een goede overeenkomst tussen de metingen op een reflectieve grating en de analytische berekeningen wordt aangetoond: voor een blazed grating met een helling van 10° wordt in combinatie met een vloeibaar kristal met een dubbelbrekendheid van 0.21, een uitwijking van een loodrecht invallende laserstraal gevonden van bijna 5.3°. Die uitwijking wordt teweeg gebracht door het aanleggen van een elektrische spanning van 10 V over het vloeibaar kristal. Sturing naar tussengelegen hoeken wordt ook gedemonstreerd. Hoewel deze hoeken niet indrukwekkend lijken, worden lichtsturingsapplicaties gebaseerd op vloeibare kristallen die over een continu bereik aan grote hoeken kunnen sturen, zoals van 45° tot $-45°$, altijd gerealiseerd door de combinatie van op zijn minst één kleine-hoek lichtsturingscomponent, die over een continu bereik kan sturen, en minstens één brede-hoek lichtsturingscomponent, die licht enkel kan sturen

naar een beperkt aantal voorbepaalde hoeken. Brede-hoek lichtsturingscomponenten worden niet behandeld in dit werk, maar hun werkingsprincipes worden wel uitgelegd. De gerealiseerde grating wordt ook gebruikt in een hybride-opstelling waarin de gereflecteerde lichtbundel kan gestuurd worden over verscheidene diffractieordes, maar ook volledig langs de grating kan worden gestuurd door totale interne reflectie (TIR). Dit kan handig zijn in bv. noodverlichting die ook dienst doet als richtbaar omgevingslicht.

Om de experimentele resultaten te staven, worden numerieke simulaties veelvuldig gebruikt. Ze dienen daarnaast ook als middel om snel ideeën te kunnen verifiëren. Als onderdeel van het gesubsidieerd onderzoek werd een software-uitbreiding geschreven voor de op eindige-elementen gebaseerde software van de onderzoeksgroep die toelaat om het gedrag van vloeibare kristallen in de nabijheid van een resistieve elektrode met arbitraire conductiviteit te kunnen simuleren. Dit laat een nauwkeurige modellering toe van lichtsturende apparaten die op vloeibare kristallen zijn gebaseerd en die gebruik maken van elektrodes met hoge resistiviteit om een gradiënt in het elektrisch veld door het vloeibaar kristal te bekomen, een aanpak die wordt onderzocht door enkele onderzoeksgroepen.

Daarnaast wordt een nieuwe technologie verkend die een van de beperkingen van multi-elektrode apparaten overkomt: het beperkte gebied waarin een vloeibaar kristal wordt beïnvloed door een kleine elektrode. De hier voorgestelde technologie gebruikt diëlektrica die een hoge permittiviteit vertonen en die kunnen gedeponeerd worden door middel van sol-gel depositie over een rij elektrodes die op een glazen substraat zijn gelegen. Het effect van de diëlektrische laag op de ruimtelijke verdeling van de director van het vloeibaar kristal in een multi-elektrode planair lichtsturingsapparaat wordt geanalyseerd met behulp van een polarisatiemicroscoop en elektro-optische simulaties. De technologie wordt gebruikt om een lichtsturingsapparaat gebaseerd op vloeibare kristallen te vergelijken met een gelijkaardig toestel waarin de diëlektrische laag niet aanwezig is: waardat het referentieapparaat nauwelijks een lichtbundel kan sturen, kan het apparaat met de diëlektrische laag een invallende laserstraal doen afwijken over iets meer dan 4°.

Ten slotte wordt een vlakke lens gebaseerd op vloeibare kristallen gedemonstreerd. De brandpuntsafstand van de lens kan elektrisch worden aangepast.

De lens is voorzien van een beperkt aantal elektroden, om de complexiteit van de adressering te beperken, maar gebruikt de technologie met diëlektrische lagen om de gradiënt in het elektrisch veld tussen de ver uiteenliggende elektrodes te verbeteren. Analyse van de retardatie tussen elektrodes door middel van de polarisatiemicroscoop bevestigt de waardigheid van het gebruik van diëlektrische lagen met hoge permittiviteit als mogelijk alternatief voor transparante geleidende metaaloxides, zoals indium tin oxide (ITO), in toepassingen gebaseerd op vloeibare kristallen waar een oppervlak wordt onderverdeeld in kleinere eenheden die op dezelfde elektrische potentiaal moeten staan. De analyse toont ook dat domeinmuren in vloeibare kristallen, die typisch voorkomen aan de rand van een elektrode, kunnen worden voorkomen. Dit wordt numeriek geverifieerd en een aantal ontwerpregels om de gradiënt van het elektrische veld in multi-elektrode apparaten te verbeteren, worden voorgelegd. De lenswerking wordt geverifieerd door een gecollimeerde lichtbundel te focusseren tot een kleine stip. De grootte van die stip wordt opgemeten en vergeleken met de stipgrootte van een door diffractie gelimiteerde lens. Verder wordt de aanpasbaarheid van de focale lengte aangetoond door dezelfde lens een straal te doen focusseren op een afstand van 4.4 cm en 7.4 cm van de lens.

De combinatie van een materiaal met hoge diëlektrische constante en een vloeibaar kristal werd voor de eerste keer aangetoond in dit werk: bij ons beste weten is het niet eerder gedemonstreerd. De techniek illustreert dat het elektrisch veld in een vloeibaar kristal homogener kan worden gemaakt door een dunne diëlektrische coating die een hoge diëlektrische permittiviteit bezit, wat een gelijkaardig effect heeft als een geleider tussen de elektrodes, maar niet zo energieverbruikend is.

Summary

Many discoveries are made by accident.

In the year 1888 Friedrich Reinitzer, an Austrian botanist, made an accidental discovery. While studying cholestery benzoate, a substance he extracted from carrots, he noticed an unusual transition between the solid and liquid state of matter. That observation was the start of research without which our world would look entirely different.

Since their discovery, liquid crystals (LCs) have been studied by researchers for their unique properties. These properties have led to the creation of a multitude of devices: we can find them e.g. in our watches, thermometers, mobile phones and monitors. The list of applications becomes longer every year. As a mass-consumer item, displays provide an incentive to fund liquid crystal research. With the advent of 3D cinema, we need displays to be faster and to have more functionality: stereoscopic vision requires that each eye observes a slightly different image. For a realistic 3D experience, the images served to our eyes should also depend on the viewing angle. A display should therefor be able to shine different images to different directions and ideally when viewers are moving: a display should “steer” light in the right direction.

Over the last few decades, beam-steering applications have made their way into the mainstream market. Projection systems, telecommunication multiplexers and optical switchboards are all applications where accurate and fast control over the direction in which light propagates is desired. Liquid crystal beam-steering devices have been replacing slower, mechanical beam-steering technologies in a number of fields, like healthcare and biology, and will continue to do so because of their unique properties and continuous research in their chemistry and physics, research that is driven by our desire to improve current technologies and societal needs.

In this work, an overview will be presented of current-day LC beam-steering and lensing technologies and their limitations. Exciting progress is being made with polarization gratings (PGs), devices that rely on the anisotropic properties of liquid crystals and photoalignment. Our attention will be focused on beam-steering technologies where a gradient in the optical

path length (OPL) of a light wave propagating through the LC structure will be induced.

To extend the application potential of LC-based light steering components, a new fabrication process is utilized in which microstructured optical substrates can be replicated fast through embossing. Photoalignment, a recently developed non-contact liquid crystal alignment technology is used to ensure homogeneous alignment of LC on top of the microstructured substrates. Due to their shape, these microstructures, blazed gratings, form an elegant solution to the problem of generating a gradient OPL. Complex electronic addressing schemes of the liquid crystal are avoided. The beam deviation angle for this class of devices, when used in transmission as well as reflection, is calculated analytically and shown to be proportional to the product of the slope of the grating and the birefringence of the liquid crystal. Good agreement between the measurements on a reflective grating configuration and the analytical calculations is found: for a blazed grating with a slope of 10° in combination with a liquid crystal with birefringence 0.21, a normally incident laser beam is deflected over nearly 5.3° by applying 10 V over the device. Steering to intermediate diffraction orders is also demonstrated. While these angles may not seem impressive, liquid crystal beam-steering devices that steer over a continuous range of large angles, say 45° to −45°, are always implemented using at least one small-angle continuous beam-steerer and at least one wide-angle beam-steering device that steers only to a limited number of predefined angles. Wide-angle beam-steering devices are not pursued in this work, but their principles are explained. The fabricated grating is also used in a hybrid configuration where the reflected beam can be steered over several diffraction orders, but can also be deflected entirely along the grating due to total internal reflection (TIR). This could prove useful in e.g. emergency lighting that also doubles as directed ambient lighting.

To support the experimental findings and serve as tools for rapid idea verification, numerical simulations will be used extensively. As part of the funded research, an extension to the research group's finite-element method (FEM) numerical codebase has been written that allows simulating the behaviour of the liquid crystal in the presence of an electrode with an arbitrary conductivity. This allows an accurate modelling of LC beam-steering devices that utilize highly resistive electrodes to generate a gradient in the electric field flowing through the liquid crystal, an approach that is still being

pursued by several research groups.

Further, a new technology is explored that overcomes one of the limitations of multi-electrode LC devices: the limited range in which a liquid crystal can be influenced by a small electrode. The technology proposed here utilizes high-κ dielectrics that can be deposited over an array of electrodes lying on top of a glass substrate by means of chemical solution deposition (CSD). The effect of the dielectric layer on the liquid crystal's director distribution in a multi-electrode LC planar beam-steering device is analysed using polarized light microscopy and electro-optical simulations. The technology is used to create an LC beam-steering device that is compared to a similar device without the high-κ dielectric layer: whereas the reference beam-steerer shows almost no beam deflection, the device with the high-κ material coating deflects an incident laser beam over a bit more than 4°.

Finally, a liquid crystal lens with electrically tunable focal length is demonstrated. It features a limited number of electrodes, to keep the addressing complexity low, but uses the high-κ dielectric layer to improve the gradient in the electric field between the widely spaced electrodes. Analysis of the retardation between electrodes using polarized light microscopy confirms the viability of using high-κ dielectrics as a possible alternative to transparent conductive metal oxides, such as indium tin oxide (ITO), in LC applications where an area is subdivided in smaller units that should be at the same potential. The analysis also shows that domain walls in liquid crystals, which occur typically at the edge of an electrode, can be prevented. This has been verified numerically and a number of design rules to improve the electric field gradient in multi-electrode LC devices are provided as a result of these simulations. The lensing operation is verified by focusing a beam down to a narrow spot. The spot size is measured and compared to the spotsize of a diffraction limited lens. Furthermore, the tunable focal length feature is demonstrated by having the same lens, about half a millimeter in diameter, focus a beam at a distance of 4.4 cm and 7.4 cm from the LC lens.

The combination of high-κ materials with liquid crystals is a first: to the best of our knowledge, it has not been demonstrated earlier. The technique illustrates that the electric field in a liquid crystal cell can be made more homogeneous by a thin high-κ material coating, similar to the effect of a conductive material between electrodes, but because of its dielectric nature, not as power consuming.

Glossary

AC	alternative current
ASIC	application specific integrated circuit
BPM	beam propagation method
CSD	chemical solution deposition
CW	continuous wave
DC	direct current
DMD	digital micromirror device
DMF	dimethylformamide
FD-BPM	finite-difference BPM
FDTD	finite-difference time-domain
FD-VBPM	finite-difference vector BPM
FEA	finite-element analysis
FE-BPM	finite-element BPM
FEM	finite-element method
FWHM	full width at half maximum
GRIN	gradient index
GUI	graphical user interface
HeNe	helium-neon
IAC	industrial advisory committee
IC	integrated circuit
ITO	indium tin oxide
LC	liquid crystal
LCD	liquid crystal display

LCOPA	liquid crystal optical phased array
LED	light emitting diode
MBBA	N-(4-Methoxybenzylidene)-4-butylaniline
MEMS	microelectromechanical systems
NMP	N-methyl-2-pyrrolidone
OPA	optical phased array
OPD	optical path difference
OPL	optical path length
PEDOT:PSS	poly(3,4-ethylenedioxythiophene) polystyrene sulfonate
PG	polarization grating
PI	polyimide
PMMA	poly(methyl methacrylate)
PSLC	polymer-stabilized liquid crystal
PVD	physical vapor deposition
PZT	lead zirconate titanate
RC	resistance–capacitance
ROI	region of interest
SEM	scanning electron microscope
SLM	spatial light modulator
TE	transverse electric
TIR	total internal reflection
TM	transverse magnetic
UV	ultraviolet
VFS	vertical field switching

1

Introduction

The goal of this chapter is to provide context and motivation of this work. An introduction to liquid crystals and current beam-steering technologies is also provided, without going into mathematical details.

1.1 Applications involving beam-steering

1.1.1 The need for beam-steering

In the modern world, humanity has discovered ways to manipulate electromagnetic waves to improve the comfort in our daily lives. We can tune into a television stream sent down from a satellite by using directional receiver antennas, send control signals through the electrical network of our houses, listen to radio signals that are being broadcast continuously and switch between different radio signals all with the flick of a button. In these examples, we rely on modulating the *frequency* or *amplitude* of electromagnetic waves.

We can also manipulate other properties of electromagnetic waves. Light, being an electromagnetic wave, is a good example, because we all have a basic familiarity with it. Who hasn't used a lens to image some scenery? Or used a mirror to look at their own reflection? These two examples are the simplest forms of manipulating the *direction* of light. But in our modern world, changing the direction of light is done for a great variety of reasons and on scales that range from the extraterrestrial down to the microscopic world: satellites intercommunicate using lasers that scan regions of space [1–5], the internet backbone runs through optical fibers that allow laser signals to travel over the ocean floors and resurface on a different continent [6], solar energy farms track the position of the sun and rotate mirrors accordingly and novel

endoscopes allow readjusting the focal plane without moving the endoscope itself [7, 8]. Even closer to home are laserprinters in which a laser continuously scans lines of the paper or compact zoom lens technology that could be used in the next-generation mobile devices [9–11]. Many technologies are being developed where being able to redirect light plays an important role.

In these examples beams or light rays are being steered in a broad sense of the word "beam-steering". In the case of the optical fiber backbone of the internet though, the "steering" is done passively: light inside the fiber is merely guided through it and resurfaces at the other end, we do not exert control over the direction in which it radiates, unless we mechanically reposition the fiber end. In this dissertation, beam-steering has a narrower meaning: to affect the direction in which light propagates by altering its phase spatially.

Some of the phase-changing technologies given earlier rely on a mechanical intervention to redirect light. The solar energy farms for example, use electricity to drive motors that rotate the mirrors. The use of mechanical components has several downsides: the components degrade due to their exposure to the elements and normal wear and tear, so recurring maintenance is required. The speed with which they redirect light is proportional to the size of the mechanics: microelectromechanical systems (MEMS) suchs as digital micromirror devices (DMDs) can flip microscopically small mirrors in several microseconds [12], while the full rotation of radiowave antennas used in radar systems is on the order of tens of seconds [13, p. 404].

A technology exists where the emission or redirection of an electromagnetic wave does not require any mechanical intervention. Instead, electrical signals that are slightly out of phase with one another are applied to an array of antennas. The resulting wave pattern can be radiated into a specific direction by adjusting the phase. Even mechanical waves, such as waves in water, can be directed using a similar mechanism: in an undeep bath of water tapping one's fingers at the same time repeatedly in the water creates a wave that propagates away from the hand, perpendicular to the line of fingers. Yet, by tapping one finger in the water, e.g. the index, and a split second later its neighbor and then the neighbor of that neighbor and so on, one creates a wave that propagates in a different direction. In antenna theory, this is known as a *phased array* antenna [14] and stems from Huygens' principle that every point on a wavefront acts as a source for secondary waves. *Optical phased arrays* are the optical analogue of this technology. Beam-steering using optical phased

arrays (OPAs), can be done in a variety of ways, such as mechanically, using e.g. pistons in deformable mirrors, magnetically [15] or thermally [16]. In this dissertation, we only consider electro-optic beam-steering. In this latter category, liquid crystals (LCs) play an important role.

1.1.2 State of the art

In the current landscape, several manufacturers have brought devices to the market that excel in some aspects of beam-steering or in the closely related field of tunable lensing. The aspects that are usually compared are the switching speed, the power requirements or the required voltages, the resolution, the tunable range and the aperture size. With that many aspects to compare, it is difficult to find a single device that performs well in all categories. Tables 1.1 and 1.2 highlight a number of recent applications and list their published results. What these tables show is that light beams can already be steered to very large space angles, even fairly wide beams. Tunable lenses have been demonstrated that can go from an unfocussed state to one where the focal length is typically a few times the size of the clear aperture diameter.

Table 1.1: State of the art beam-steering devices

Company / Product	Technology / working principle	Field of View	Switching speed	Notes
Boulder Nonlinear Systems [17]	Liquid crystal polarization grating	$80° \times 80°$	<10 ms at 1550 nm	5 cm $\times$ 5 cm input beams, 1° resolution using a small-angle beam-steering device possible, high efficiency
Vescent Photonics / SEEOR [18, 19]	Liquid crystal cladded waveguide	$30° \times 5°$	50 ms	purely analog steering in a waveguide

Table 1.2: Comparison of some commercially available tunable lens devices

Company / Product	Technology / working principle	Clear Aperture	Focal length range	Switching speed	Power / voltage requirements
Optotune /EL-10-30 [20]	Shape changing polymer lenses	10 mm–25 mm	120 mm to 15 mm	2.5 ms	0 W to 1.1 W, 0 mA to 300 mA, 5 V
Holochip / APX1007 [21]	Shape changing polymer lenses	10 mm	400 mm to 1000 mm	10 ms	$<$ 175 mA and 5 V, so $\pm$1 W
Lensvector[22]	Liquid crystal	$\sim$ 2 mm	∞ to 10 cm	1 s	unspecified
Varioptic / Arctic 39N0 family [23]	Electrowetting	$\sim$ 4 mm	∞ to 7 cm	$\sim$ 30 ms	38 V–60 V

1.1.3 Purpose of this work

The work presented in this thesis focuses on optical components for switching, steering and focusing light using liquid crystals. In particular, new techniques are studied that enable the coming of a new generation of liquid crystal beam-steering devices and tunable lenses. Strengths and weaknesses of these techniques are listed, as a guide for possible follow-up research. How the liquid crystal performs using these new techniques and what the implications are of that on several beam-steering parameters is studied using both numerical simulations and experimental results, all of which are listed in this dissertation.

All of the work presented is also used in the Strategic Basic Research project SECONDOS, in which “Smart electro-optical components for the direction of solid-state light” are researched and which is funded by the Flemish Institute for Science and Technology (IWT) under grant number SBO 120019.

In the SECONDOS project 3 academic partners, CMST (Ghent University), the Center for MicroSystems Technology, LCP (Ghent University), the Liquid Crystals and Photonics group and B-Phot (Vrije Universiteit Brussel), the Brussels Photonics team, collaborate with the industrial partner ETAP to “extend the application potential of light steering components based on liquid crystal material, by demonstrating devices that overcome the main limitations of the current state-of-the-art components” [24]. The partners are counseled from an industrial insight by the industrial advisory committee (IAC), which consists of the following companies: Anteryon, LC-Tec, TP Vision, Barco, ADB Lighting Technologies, KLA-Tencor, EcoNation, and Schréder. Representatives of the project Groen Licht Vlaanderen are also included in the IAC.

The work is also performed under the umbrella of the electro-optical particle manipulation driver of the Center for Nano- and Biophotonics at Ghent University. The work has also received funding from the Interuniversity Attraction Poles program of the Belgian Science Policy Office (IAP P7-35).

1.2 Introducing liquid crystals

The work presented in this thesis assumes the reader has basic familiarity with nematic liquid crystals. Those who are familiar with the matter may skip this subchapter and head over to the next subchapter that provides relevant information on the current state of beam-steering technologies in which liquid crystals play a role.

This subchapter will only provide the most basic background information to understand the devices and simulations discussed in the next chapters. For more information, the reader is referred to the excellent literature already available on the topic [25, 26].

1.2.1 Nematic liquid crystals

Most people are familiar with three states of matter that are commonly observed in daily life. These are the solid, liquid and gas states, of which ice, water and water vapour are prime examples. Some may even be familiar with the plasma state, which is not observed as often as the others, but may easily be produced in a microwave oven when a sharp metallic object is inside it. The stars, including the sun, are also plasmas, as are candle flames.

A liquid crystal (LC) is a material that is in a liquid state: it cannot be easily compressed, but flows and assumes the form of the container it is in, like water in a bottle. Unlike water though, it also exhibits properties of a solid, like anisotropy and optical birefringence. Because of this, liquid crystals are also known as mesomorphic phases: they are an intermediate form between solid and liquid.

Figure 1.1 shows the chemical structure of N-(4-Methoxybenzylidene)--4-butylaniline (MBBA), a molecule of an organic compound that exhibits a liquid crystalline phase at room temperature. The molecule has a rather large aspect ratio: it is much longer than it is wide. This anisotropic shape gives rise to preferred orientations of nearby molecules. So although the molecules are not fixed in space like with a solid, they tend to point in the same direction, so they exhibit a certain degree of orientational order. The chemical structure also reveals a large cluster of electrons that are delocalized in the conjugated system that exists of the overlapping p-orbitals in the two aromatic rings and the p-orbital in the double bond of nitrogen, which is used as a linking group between the two rings. Because the electrons in such a system can be delocalized easily, the molecule is said to have a large electric polarizability, α, which expresses the tendency to have the charges displaced by an electric field. The polarizability is bigger along the axis of the molecule, $\alpha_{\parallel} > \alpha_{\perp}$, so the molecule's properties are anisotropic as well. These two features, the anisotropic molecular shape and large molecular polarizability, are characteristic for liquid crystals.

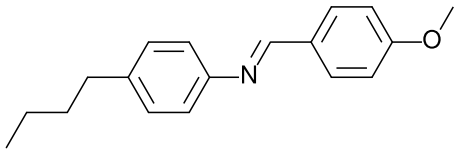

Fig. 1.1: Chemical structure of N-(4-Methoxybenzylidene)-4-butylaniline (MBBA), an organic substance that exhibits a nematic liquid crystalline phase.

Nematic liquid crystals are one of many mesomorphic phases that exist in nature. The orientation in a small volume is represented by what is known as the director, $\vec{L}$, a headless vector ($\vec{L} = -\vec{L}$) that indicates the spatial and temporal average of the orientation of the liquid crystal molecules. The director is often drawn schematically as a cylinder, or rotationally symmetric stick, which stresses its main properties.

Conceptually, nematic liquid crystals, or nematics, are the easiest mesophase to understand: there is only long-range orientational order of the director. In other mesophases, the director may be stratified, like with smectic liquid crystals, or may rotate about an axis, like with chiral nematics. Figure 1.2 shows conceptually what order in these phases is like. Many more liquid crystal phases exist, but in this thesis, only ordinary nematic LCs are considered for simulations and experiments. They are often found in displays.

When the director points in the same direction throughout the liquid crystal, the LC is said to be undeformed. Deformations of the director occur often and can be induced by applying e.g. an electric field over the liquid crystal. The deformations can be described in terms of three basic types,

(a) (b) (c)

Fig. 1.2: Schematic illustration of mesogens in several liquid crystal phases: (a) ordinary nematic phase, (b) smectic A phase, (c) chiral nematic phase. Images retrieved from [27], made by Kebes, licensed under CC BY-SA 3.0.

which are known as splay, twist and bend deformations and are illustrated in figure 1.3.

1.2.2 Birefringence

Because of the tendency of liquid crystal molecules to align their long axis in the same direction, liquid crystals exhibit anisotropic properties on a macroscopic scale. One such property is birefringence, which is related to a material's refractive index, n. The refractive index of a medium is a measure for the speed of light as it propagates through that medium. It plays an important role when light refracts at an interface between two media and leads to the observation that a spoon in a half-filled glass of water appears sharply bent. The refractive index of a material can be related to the electric polarizability of the molecules of that medium, so for a medium with anisotropic molecular polarizability where the molecules tend to point in the same direction, the refractive index is expected to be different along different directions as well. If the refractive index of a material depends on the polarization and propagation direction of light, the material is said to be birefringent.

A simple experiment can be used to illustrate birefringence in a liquid crystal: shine the beam of a laser pointer on a wedge filled with homogeneously aligned liquid crystal and rotate the laser pointer about its axis, as shown in figure 1.4. At specific rotation angles a single beam emerges from the wedge, but in general there are two beams emerging. If the cell were filled with an isotropic material, only a single beam would emerge.

The beams from laser pointers are often polarized*, meaning the electric field of the light beam oscillates in a specific plane. The reason the beam splits in two orthogonally polarized beams is that the part of the electric field that oscillates in a plane parallel to the director experiences a refractive index

(a) (b) (c)

Fig. 1.3: The three basic deformations in nematics: (a) splay, (b) twist and (c) bend deformation.

*Laser pointers are not always polarized though, in which case the two beams in the experiment shown in figure 1.4 will always be visible, no matter the rotation angle.

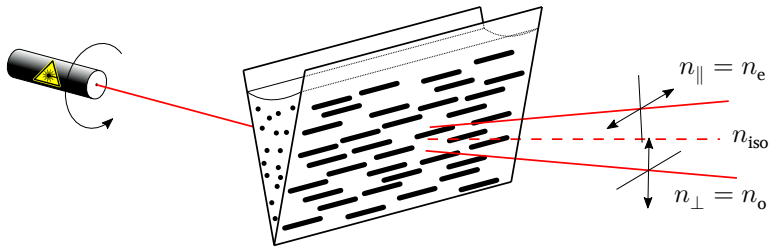

Fig. 1.4: Birefringence visualized: two beams emerge from a wedge cell filled with a homogeneously aligned nematic LC. The beams have orthogonal polarizations, as indicated by the arrows. By heating up the LC to above its nematic–isotropic transition temperature, only a single beam will be present, which is at an angle in between the angles of the extraordinary and ordinary beam.

$n_{\parallel}$, whereas the part that oscillates in a plane perpendicular to the director experiences a refractive index $n_{\perp}$. These indices are also referred to as the extraordinary and ordinary refractive index of the liquid crystal, n_{e} and n_{o} respectively. At the interface between the liquid crystal and the wedge, the different indices cause these orthogonal polarizations to propagate in different directions, in accordance with Snell's law.

1.2.3 Liquid crystal alignment

The wedge described in figure 1.4 illustrates a homogeneously aligned nematic. There are several ways in which the alignment of a liquid crystal can be affected. The methods used in this thesis are described here shortly.

A. *By means of an alignment layer*

An alignment layer imposes a preferential orientation of the LC director. It is applied to an interface that is in contact with the LC. Within the neighborhood of that interface, the liquid crystal director is fixed. It takes a certain amount of energy to change the director orientation near the interface.

B. *By means of an electric field*

The orientation of the director can be changed by applying an electric field over the liquid crystal. The electric polarizability of the liquid crystal molecules allows the applied electric field to induce a dipole moment (or change it if already present). In the presence of the field, a torque is exerted on the

dipole moment that reorients the molecules so as to minimize the torque, as illustrated in figure 1.5. For liquid crystals with positive dielectric anisotropy ($\varepsilon_{\parallel} > \varepsilon_{\perp}$), the molecules tend to align their long axes with the electric field lines. Hence, the director will also align more with the electric field. For nematic liquid crystals the time needed to reorient the director, to "switch" the liquid crystal, is proportional to the square of the thickness of the cell, so LC layers are usually made a few micrometers thin [28].

1.3 Current approaches to optical phase manipulation using liquid crystals

As explained in section 1.2.2, light experiences a certain refractive index when it propagates through a liquid crystal. In beam-steering and lensing applications, the experienced refractive index is ideally a well-controlled continuously varying function across the LC. It is achieved by having the LC director change orientation smoothly, which can be done in several ways.

1.3.1 Beam-steering

A. *Small-angle beam-steering*

Classical liquid crystal beam-steering approaches affect the phase of an electromagnetic plane wave by changing the optical path length (OPL) over a region in space. The optical path length is the product of the experienced refractive index and the thickness of the material through which it propagates. Because the experienced refractive index in a liquid crystal is limited to the

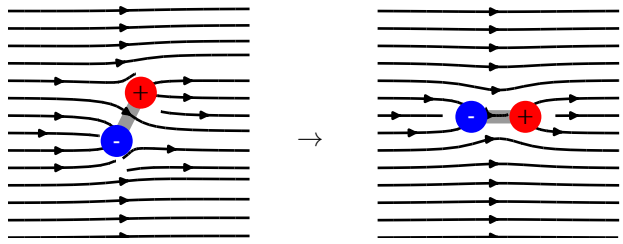

Fig. 1.5: A dipole in an electric field experiences a torque that tends to align the dipole with the electric field. The dipole also changes the electric field locally.

range between the extraordinary and ordinary index of the LC, there is a limit on the OPL as well that is defined by the LC and the thickness of that layer. In practice, the LC layer is rarely more than a few tens of microns thick, to reduce switching times, as explained earlier, and to keep the costs low*.

For monochromatic light, this limit on the OPL is not a problem: because light is a sinusoidally varying electromagnetic wave, an abrupt phase difference of one wavelength or a multiple thereof has no effect on the wave, as illustrated in figure 1.6. Broadband light will experience diffraction though, because the phase matching condition is not fulfilled.

In their excellent review paper, McManamon et al. categorize narrow-band beam-steering devices based on the way this sawtooth-like phase wrapping is achieved [31]: either the period is altered, which changes the blaze angle α as well, or the blaze angle is altered, but the period is kept constant. Both approaches allow us to steer the wavefronts in the desired direction. McManamon et al. name these approaches the variable period approach and variable blaze approach. With variable blaze beam-steering, one cannot steer light to a continuum of angles, because the phase jumps have to be a multiple of the wavelength.

The beam-steering efficiency, being the ratio of light that is steered in the desired direction relative to the incident light power, in devices that rely on this change in the OPL [32–35] is limited by two factors. The first is the non-ideal phase jump that occurs at the flyback region, the region where the phase is reset. This is because the liquid crystal deforms continuously [36] due

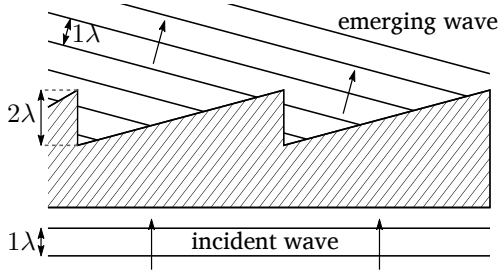

Fig. 1.6: A plane monochromatic wave travels through a blazed grating. When the optical path length difference is a multiple of the wavelength, λ, the wave is perfectly transmitted to one of the diffraction orders.

*For comparison, at the time of writing, one gram of gold is worth about 37 € [29]. One gram of MBBA, the LC mesogen seen earlier, costs about 15 € [30].

to visco-elastic forces. In the flyback region, fringing fields further prevent the appearance of an ideal phase reset [37]. The devices discussed in chapters 2 and 3 of this thesis are also limited by fringing fields. The second limiting factor according to McManamon et al. is the discrete nature of the phase steps. Multielectrode devices indeed apply a staircase-like voltage profile over the LC. As long as the electrodes can be made small and are closely packed this is not so much of a problem, because the visco-elastic forces of the LC will smoothen out the phase steps. The fabrication of very thin electrodes requires expensive technology though and the electronic addressing of a large number of electrodes individually is challenging. Several researchers have circumvented the loss in steering efficiency due to the discrete phase steps by generating a linear ramp in the electric field up to the flyback regions [32, 38–41]. This technique is used in both chapters 2 and 3 as well.

The main limitation lies with the non-ideal phase jump. It is shown that to obtain high steering efficiency in sawtooth-like beam-steering devices, the steering angle should be limited [31]: due to the fringing field effect, a device featuring a 5° steering angle has a theoretical efficiency of 56.5 %, whereas a 1° steering angle device has slightly over 90 % maximal efficiency.

For that reason, the continuous angle beam-steering devices are considered small-angle beam-steerers. To obtain much larger angles they are often put in tandem with devices that can steer efficiently to a discrete set of large angles. Such combinations lead to devices that allow continuous steering over a wide angular range.

B. *Wide-angle beam-steering*

Wide-angle beam-steering approaches using liquid crystals can be found in three varieties. In the first, a holographic medium is used to which an array of holographic patterns have been imprinted. Each pattern is the result of mixing a reference beam at a steering angle of interest with a signal beam. By illuminating this pattern with a signal beam, the reference beam will be reproduced, travelling at the original angle of interest [42, 43]. By placing a small-angle beam-steering device in front of this holographic medium, steering to large angles ($\pm 45°$) can be achieved by illuminating the hologram that generates the desired reference beam [44]. Note that another small-angle beam-steering device is required after the hologram to allow continuous

beam-steering.

The second wide-angle beam-steering class of devices is based on the spatial separation of orthogonal polarizations in birefringent prisms. A Wollaston prism e.g. separates unpolarized light into two orthogonal linear polarizations, as illustrated in figure 1.7. This can be exploited by having a liquid crystal polarization rotator before the prism, which transforms the incident polarization into the type required to be steered to one of the two possible angles. The angular separation depends on the wavelength of light and the prism wedge angle, which implies that the prisms will be fairly thick to obtain steering to large angles. As with the hologram, a small-angle beam-steering device is placed before the polarization rotator–prism combination, to allow continuous steering. This time however the deflection changes continuously with the angle of incidence as well, so there is no need for another small-angle beam-steerer after the prisms.

The third class is one of the most recent and exciting innovations to the field of beam-steering devices: polarization gratings (PGs). Their functionality is quite similar to that of the birefringent gratings, but they can be made much thinner as they use a liquid crystal layer that need only be half a wavelength thick. Polarization gratings deflect circularly polarized beams to the positive or negative first diffraction order of the grating with efficiencies close to 100 % [17, 46, 47]. When the grating configuration is removed electrically by aligning the director uniformly across the LC cell, the device can also transmit to the zeroth order.

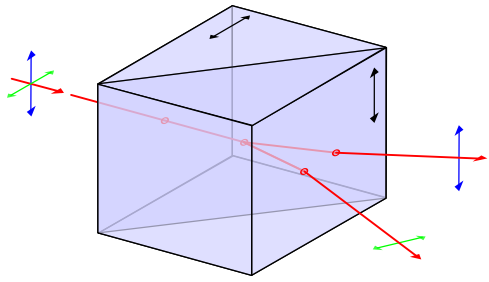

Fig. 1.7: A Wollaston-prism spatially separates unpolarized light in two orthogonal, linearly polarized waves. The c-axis of the birefringent prisms has been annotated with black arrows. Image retrieved from [45], made by Fgalore, licensed under CC BY-SA 3.0.

1.3.2 Lensing

Lensing is very similar to beam-steering. The main difference is that rather than attempting to generate a linear, possibly wrapped, phase shift across a LC cell, the phase shift should be parabolic. That means that a centro-symmetric director distribution is required in LC lenses.

Traditionally, lens operation is achieved by applying a radially varying electric field, which changes the OPL in a similar way as with beam-steering devices. The first liquid crystal lens that operated on this principle appeared in 1979 [48]. It featured a liquid crystal layer that was trapped between a planar electrode and a curved one. Variations on the curved electrode design that allow the liquid crystal layer to be flat, which is desirable from a manufacturing point of view, have been demonstrated since [49–52].

An alternative to the curved electrode approach is given by the patterned electrode design. Such devices feature two parallel, planar electrodes, one of which is patterned. The patterned electrode can take very simple forms, such as a single hole [53–55] or a series of concentric electrodes [56–58]. Both approaches realize a spatially non-uniform electric field, but the desired electric field variation is harder to achieve with hole-patterned electrodes. The multi-electrode approach can avoid optical aberrations, at the cost of a more complex electronic driver.

A third category of electric gradient inducing lenses is given by planar LC devices, with uniform electrodes, where the gradient OPL is achieved by having a gradient in the polymer concentration of a polymer-stabilized liquid crystal (PSLC) [59]. PSLC has also been used in beam-steering applications [39].

When the used liquid crystal in these three techniques is a nematic, these devices only act as lenses for one linear polarization component of the light so that a polarizer is necessary. However, since the recent interest in blue phases [60, 61], polarization independent lenses using gradient electric fields have been proposed [62–64] and one, based on the hole-patterned electrode approach, has already been demonstrated [65].

Most lens approaches have focused on generating a centro-symmetric director distribution using electrical fields, but with the recent advances in photoalignment, the director distribution can be azimuthally and radially varying without the need for applying voltages, similar to the polarization

gratings mentioned earlier. This advancement has lead to q-plates [66], devices with an azimuthal distribution of the local optical axis, having a topological charge q at its center defect and lenses. The various demonstrated lenses include Fresnel zone plates that reach efficiencies of 35 % and more [67, 68], which is close to the theoretical maximum of 41 %, as well as lenses with continuously varying director profiles [69], some of which are polarization independent [70] or broadband [71].

1.4 Outline of this dissertation

In chapter 2, information related to the simulation programs and the used fabrication technologies is provided to ensure the reader has sufficient background to understand and reproduce the results from the chapters that follow. Results from the different simulation programs are explained in a logical way, using a specific beam-steering device as an example.

Chapter 3 is about a simple beam-steering device that can be produced with means that allow for rapid replication. The performance of the device is discussed analytically and numerically in transmissive and reflective configurations. A reflective configuration is fabricated and its performance measured and compared to theoretical results.

In chapter 4 the influence of coating a substrate having multiple addressable electrodes with a material having a high dielectric constant on the beam-steering capabilities of a liquid crystal beam-steerer is studied. This technology of combining liquid crystals and materials with a large dielectric constant in this way is demonstrated for the first time by fabricating a one-dimensional beam-steering device and comparing its performance to an uncoated reference device.

Chapter 5 builds further on the results from chapter 4. The technology discussed in chapter 4 is used to create a liquid crystal lens of which the focal length can be tuned. The performance of the fabricated lens devices is studied using convential methods.

Chapter 6 bundles the main conclusions drawn in the preceding chapters and presents perspectives for future research.

1.5 References

1. Ziemkiewicz, M., S. R. Davis, S. D. Rommel, D. Gann, B. Luey, *et al.*, "Laser-based satellite communication systems stabilized by non-mechanical electro-optic scanners", in *SPIE Defense + Security*, International Society for Optics and Photonics, 2016, pp. 982 808–982 808 (cited on p. 1).
2. Guelman, M., A. Kogan, A. Kazarian, A. Livne, M. Orenstein, *et al.*, "Acquisition and pointing control for inter-satellite laser communications", *IEEE Transactions on Aerospace and Electronic Systems*, vol. 40, no. 4, pp. 1239–1248, 2004. [Online] (cited on p. 1).
3. Stockley, J. and S. Serati, "Multi-access laser terminal using liquid crystal beam steering", in *2005 IEEE Aerospace Conference*, IEEE, 2005, pp. 1972–1977 (cited on p. 1).
4. Geday, M., X. Quintana, E. Otón, B. Cerrolaza, D. Lopez, *et al.*, "Development of liquid crystal based adaptive optical elements for space applications", in *Proc. Intl. Conf. on Space Optics ICSO 2010*, 2010 (cited on p. 1).
5. Rademakers, L. and D. Coleman, *Spinoff 2011, Nasa technologies benefit society*. U.S. Government Printing Office, 2011 (cited on p. 1).
6. Carter, L., *Submarine cables and the oceans: Connecting the world*, 31. UNEP/Earthprint, 2009 (cited on p. 1).
7. Chen, H.-S. and Y.-H. Lin, "An endoscopic system adopting a liquid crystal lens with an electrically tunable depth-of-field", *Opt. Express*, vol. 21, no. 15, pp. 18 079–18 088, 2013. [Online] (cited on p. 2).
8. Hassanfiroozi, A., Y.-P. Huang, B. Javidi, and H.-P. D. Shieh, "Hexagonal liquid crystal lens array for 3d endoscopy", *Optics express*, vol. 23, no. 2, pp. 971–981, 2015 (cited on p. 2).
9. Kim, H., J. Park, N. H. Chuc, H. R. Choi, J. D. Nam, *et al.*, "Development of dielectric elastomer driven micro-optical zoom lens system", vol. 6524, 2007, pp. 65241V–65241V–10. [Online] (cited on p. 2).
10. Chen, W.-H., J.-S. Lu, and G.-D. J. Su, "Ionic polymer metal composite for an optical zoom in a compact camera", *Opt. Express*, vol. 23, no. 10, pp. 13 265–13 277, 2015. [Online] (cited on p. 2).
11. Kim, B.-C., H. Kim, H. C. Nguyen, M. S. Cho, Y. Lee, *et al.*, "Development of a dry actuation conducting polymer actuator for micro-optical zoom lenses", vol. 6927, 2008, pp. 69271M–69271M–7. [Online] (cited on p. 2).
12. Dudley, D., W. M. Duncan, and J. Slaughter, "Emerging digital micromirror device (dmd) applications", in *Micromachining and Microfabrication*, International Society for Optics and Photonics, 2003, pp. 14–25 (cited on p. 2).
13. Petersen, J. K., *Handbook of surveillance technologies*. CRC press, 2012 (cited on p. 2).
14. Hansen, R. C., *Phased array antennas*. John Wiley & Sons, 2009, vol. 213 (cited on p. 2).

15. Brousseau, D., E. F. Borra, and S. Thibault, "Wavefront correction with a 37-actuator ferrofluid deformable mirror", *Opt. Express*, vol. 15, no. 26, pp. 18 190–18 199, 2007. [Online] (cited on p. 3).

16. Van Acoleyen, K., W. Bogaerts, J. Jágerská, N. Le Thomas, R. Houdré, *et al.*, "Off-chip beam steering with a one-dimensional optical phased array on silicon-on-insulator", *Opt. Lett.*, vol. 34, no. 9, pp. 1477–1479, 2009. [Online] (cited on p. 3).

17. Kim, J., C. Oh, M. J. Escuti, L. Hosting, and S. Serati, "Wide-angle, nonmechanical beam steering using thin liquid crystal polarization gratings", in *Proc. SPIE*, vol. 7093, 2008, p. 709 302 (cited on pp. 4, 13).

18. Davis, S. (2011). Electro-optic steering of a laser beam, [Online] (visited on 12/17/2016) (cited on p. 4).

19. Opli. (2015). Vescent photonics introduces cots non-mechanical beam steering device, [Online] (visited on 12/17/2016) (cited on p. 4).

20. Blum, M., M. Büeler, C. Grätzel, and M. Aschwanden, "Compact optical design solutions using focus tunable lenses", in *SPIE Optical Systems Design*, International Society for Optics and Photonics, 2011, 81670W–81670W (cited on p. 4).

21. *2012 product brochure*, http://www.holochip.com/pdf/APx-1007+Brochure.pdf, Holochip, 2012 (cited on p. 4).

22. Wilson, A. (2010). Tunable optics, [Online] (visited on 12/17/2016) (cited on p. 4).

23. Jacques-Sermet, O., *Arctic 39n family*, Varioptic, 2016 (cited on p. 4).

24. De Smet, H. (2012). Secondos, [Online] (visited on 07/01/2013) (cited on p. 5).

25. Khoo, I., *Liquid crystals*, ser. Wiley Series in Pure and Applied Optics. Wiley, 2007. [Online] (cited on p. 6).

26. Yang, D.-K., *Fundamentals of liquid crystal devices*. John Wiley & Sons, 2014 (cited on p. 6).

27. Wikipedia. (2016). Liquid crystal — Wikipedia, the free encyclopedia, [Online] (visited on 09/22/2016) (cited on p. 7).

28. Schiekel, M., K. Fahrenschon, and H. Gruler, "Transient times and multiplex behavior of nematic liquid crystals in the electric field", *Applied physics*, vol. 7, no. 2, pp. 99–105, 1975 (cited on p. 10).

29. GoldBroker. (2016). Gold price today – eu, [Online] (visited on 10/16/2016) (cited on p. 11).

30. Sigma-Aldrich. (2016). Liquid crystals. Price for 5g, [Online] (visited on 10/16/2016) (cited on p. 11).

31. McManamon, P. F., P. J. Bos, M. J. Escuti, J. Heikenfeld, S. Serati, *et al.*, "A review of phased array steering for narrow-band electrooptical systems", *Proceedings of the IEEE*, vol. 97, no. 6, pp. 1078–1096, 2009 (cited on pp. 11, 12).

32. Matic, R. M., "Blazed phase liquid crystal beam steering", in *OE/LASE'94*, International Society for Optics and Photonics, 1994, pp. 194–205 (cited on pp. 11, 12).

33. McManamon, P. F., T. A. Dorschner, D. L. Corkum, L. J. Friedman, D. S. Hobbs, *et al.*, "Optical phased array technology", *Proceedings of the IEEE*, vol. 84, no. 2, pp. 268–298, 1996 (cited on p. 11).

34. Sharp, R., D. Resler, D. Hobbs, and T. A. Dorschner, "Electrically tunable liquid-crystal wave plate in the infrared", *Optics letters*, vol. 15, no. 1, pp. 87–89, 1990 (cited on p. 11).

35. Resler, D., D. Hobbs, R. Sharp, L. Friedman, and T. Dorschner, "High-efficiency liquid-crystal optical phased-array beam steering", *Optics letters*, vol. 21, no. 9, pp. 689–691, 1996 (cited on p. 11).

36. Beeckman, J., K. Neyts, and P. J. Vanbrabant, "Liquid-crystal photonic applications", *Optical Engineering*, vol. 50, no. 8, pp. 081 202–081 202, 2011 (cited on p. 11).

37. Apter, B., U. Efron, and E. Bahat-Treidel, "On the fringing-field effect in liquid-crystal beam-steering devices", *Applied optics*, vol. 43, no. 1, pp. 11–19, 2004 (cited on p. 12).

38. Wang, X., D. Wilson, R. Muller, P. Maker, and D. Psaltis, "Liquid-crystal blazed-grating beam deflector", *Applied Optics*, vol. 39, no. 35, pp. 6545–6555, 2000 (cited on p. 12).

39. Ren, H., Y.-H. Fan, and S.-T. Wu, "Prism grating using polymer stabilized nematic liquid crystal", *Applied Physics Letters*, vol. 82, no. 19, pp. 3168–3170, 2003. [Online] (cited on pp. 12, 14).

40. Shang, X., A. M. Trinidad, P. Joshi, J. De Smet, D. Cuypers, *et al.*, "Tunable optical beam deflection via liquid crystal gradient refractive index generated by highly resistive polymer film", *IEEE Photonics Journal*, vol. 8, no. 3, pp. 1–11, 2016. [Online] (cited on p. 12).

41. **Willekens, O.**, X. Jia, M. Vervaeke, X. Shang, T. Baghdasaryan, *et al.*, "Reflective liquid crystal hybrid beam-steerer", *Opt. Express*, vol. 24, no. 19, pp. 21 541–21 550, 2016. [Online] (cited on p. 12).

42. Kogelnik, H., "Coupled wave theory for thick hologram gratings", *Bell System Technical Journal*, vol. 48, no. 9, pp. 2909–2947, 1969 (cited on p. 12).

43. Collier, R., *Optical holography*. Elsevier, 2013 (cited on p. 12).

44. Smith, I. and M. Holz, *Wide-angle beam steering system*, US Patent 7,215,472, 2007. [Online] (cited on p. 12).

45. Wikipedia. (2016). Wollaston prism — Wikipedia, the free encyclopedia, [Online] (visited on 10/15/2016) (cited on p. 13).

46. Nersisyan, S. R., N. V. Tabiryan, L. Hoke, D. M. Steeves, and B. Kimball, "Polarization insensitive imaging through polarization gratings", *Opt. Express*, vol. 17, no. 3, pp. 1817–1830, 2009. [Online] (cited on p. 13).

47. Nys, I., J. Beeckman, and K. Neyts, "Switchable 3d liquid crystal grating generated by periodic photo-alignment on both substrates", *Soft matter*, vol. 11, no. 39, pp. 7802–7808, 2015 (cited on p. 13).

48. Sato, S., "Liquid-crystal lens-cells with variable focal length", *Japanese Journal of Applied Physics*, vol. 18, no. 9, p. 1679, 1979 (cited on p. 14).

49. Wang, B., M. Ye, M. Honma, T. Nose, and S. Sato, "Liquid crystal lens with spherical electrode", *Japanese Journal of Applied Physics*, vol. 41, no. 11A, p. L1232, 2002. [Online] (cited on p. 14).

50. Ren, H., Y.-H. Fan, S. Gauza, and S.-T. Wu, "Tunable-focus flat liquid crystal spherical lens", *Applied physics letters*, vol. 84, no. 23, pp. 4789–4791, 2004 (cited on p. 14).

51. Asatryan, K., V. Presnyakov, A. Tork, A. Zohrabyan, A. Bagramyan, *et al.*, "Optical lens with electrically variable focus using an optically hidden dielectric structure", *Optics express*, vol. 18, no. 13, pp. 13 981–13 992, 2010 (cited on p. 14).

52. Ren, H., D. W. Fox, B. Wu, and S.-T. Wu, "Liquid crystal lens with large focal length tunability and low operating voltage", *Optics Express*, vol. 15, no. 18, pp. 11 328–11 335, 2007 (cited on p. 14).

53. Nose, T. and S. Sato, "A liquid crystal microlens obtained with a non-uniform electric field", *Liquid Crystals*, vol. 5, no. 5, pp. 1425–1433, 1989 (cited on p. 14).

54. Naumov, A. F., G. D. Love, M. Y. Loktev, and F. L. Vladimirov, "Control optimization of spherical modal liquid crystal lenses", *Opt. Express*, vol. 4, no. 9, pp. 344–352, 1999. [Online] (cited on p. 14).

55. Ye, M. and S. Sato, "Optical properties of liquid crystal lens of any size", *Japanese journal of applied physics*, vol. 41, no. 5B, p. L571, 2002 (cited on p. 14).

56. Riza, N. A. and M. C. Dejule, "Three-terminal adaptive nematic liquid-crystal lens device", *Optics letters*, vol. 19, no. 14, pp. 1013–1015, 1994 (cited on p. 14).

57. Chan, W. W. and S. T. Kowel, "Imaging performance of the liquid-crystal-adaptive lens with conductive ladder meshing", *Applied optics*, vol. 36, no. 34, pp. 8958–8969, 1997 (cited on p. 14).

58. Li, L., D. Bryant, T. Van Heugten, and P. J. Bos, "Near-diffraction-limited and low-haze electro-optical tunable liquid crystal lens with floating electrodes", *Optics express*, vol. 21, no. 7, pp. 8371–8381, 2013 (cited on p. 14).

59. Presnyakov, V., K. Asatryan, T. Galstian, and A. Tork, "Polymer-stabilized liquid crystal for tunable microlens applications", *Optics express*, vol. 10, no. 17, pp. 865–870, 2002 (cited on p. 14).

60. Kikuchi, H., "Liquid crystalline blue phases", in *Liquid crystalline functional assemblies and their supramolecular structures*, Springer, 2007, pp. 99–117 (cited on p. 14).

61. Kitzerow, H.-S., "Blue phases come of age: A review", vol. 7232, 2009, pp. 723205–723205–14. [Online] (cited on p. 14).

62. Li, Y., Y. Liu, Q. Li, and S.-T. Wu, "Polarization independent blue-phase liquid crystal cylindrical lens with a resistive film", *Applied optics*, vol. 51, no. 14, pp. 2568–2572, 2012 (cited on p. 14).

63. Lee, C.-T., Y. Li, H.-Y. Lin, and S.-T. Wu, "Design of polarization-insensitive multi-electrode grin lens with a blue-phase liquid crystal", *Opt. Express*, vol. 19, no. 18, pp. 17 402–17 407, 2011. [Online] (cited on p. 14).

64. Li, Y. and S.-T. Wu, "Polarization independent adaptive microlens with a blue-phase liquid crystal", *Opt. Express*, vol. 19, no. 9, pp. 8045–8050, 2011. [Online] (cited on p. 14).

65. Lin, Y.-H., H.-S. Chen, H.-C. Lin, Y.-S. Tsou, H.-K. Hsu, *et al.*, "Polarizer-free and fast response microlens arrays using polymer-stabilized blue phase liquid crystals", *Applied Physics Letters*, vol. 96, no. 11, p. 113 505, 2010 (cited on p. 14).

66. Ji, W., C.-H. Lee, P. Chen, W. Hu, Y. Ming, *et al.*, "Meta-q-plate for complex beam shaping", *Scientific reports*, vol. 6, 2016 (cited on p. 15).

67. Huang, Y.-H., S.-W. Ko, S.-C. Chu, and A. Y.-G. Fuh, "High-efficiency fresnel lens fabricated by axially symmetric photoalignment method", *Applied optics*, vol. 51, no. 32, pp. 7739–7744, 2012 (cited on p. 15).

68. Wang, X. Q., F. Fan, T. Du, A. M. W. Tam, Y. Ma, *et al.*, "Liquid crystal fresnel zone lens based on single-side-patterned photoalignment layer", *Appl. Opt.*, vol. 53, no. 10, pp. 2026–2029, 2014. [Online] (cited on p. 15).

69. Zhao, C.-X., F. Fan, L.-Y. Shi, V. Chigrinov, and H. S. Kwok, "P-118: Low voltage driving tunable liquid crystal lens using photoalignment method", *SID Symposium Digest of Technical Papers*, vol. 46, no. 1, pp. 1611–1613, 2015. [Online] (cited on p. 15).

70. Fuh, A. Y.-G., S.-W. Ko, S.-H. Huang, Y.-Y. Chen, and T.-H. Lin, "Polarization-independent liquid crystal lens based on axially symmetric photoalignment", *Opt. Express*, vol. 19, no. 3, pp. 2294–2300, 2011. [Online] (cited on p. 15).

71. Tabiryan, N. V., S. V. Serak, S. R. Nersisyan, D. E. Roberts, B. Y. Zeldovich, *et al.*, "Broadband waveplate lenses", *Opt. Express*, vol. 24, no. 7, pp. 7091–7102, 2016. [Online] (cited on p. 15).

2

Used methods

Many of the results presented later in this work rely on knowledge of computer programs, such as meshing and simulation software, and fabrication aspects of liquid crystal devices. In order not to repeat the simulation settings that are common for the results presented here and to provide the reader with a better background, these frequently used methods are discussed in this chapter.

Some paragraphs in the technology section will be intentionally short, as they deal with well-known fabrication techniques to which the work presented here made no contributions and that are discussed in far more depth in the literature. Some of the processing parameters are varied between runs, but the settings listed in section 2.3 provide the parameter sets that give good and reproducible results.

The chapter is started with a description of polarized modes, as these are used commonly in electromagnetic propagation problems to simplify the analysis.

2.1 Transverse modes at an interface

When an electromagnetic wave such as light is obliquely incident on an interface, scientists will often describe the wave as a superposition of transverse modes, the transverse electric (TE) and transverse magnetic (TM) mode. These two modes arise naturally in the study of reflection and refraction problems as a set of uncoupled linearly polarized waves [1, chapter 6.2]. The modes can be superimposed to yield any incident wave polarization, which allows us to reduce problems of arbitrary waves to the study using these two modes.

To understand the meaning of these terms, consider figures 2.1a and 2.1b. Both figures share the same plane of incidence, which is the plane that

encompasses the wave vector $\vec{k}$ and the normal to the interface, $\vec{n}$. In a TM mode, the magnetic field, $\vec{H}$, is perpendicular to the plane of incidence. Light in this mode is said to be p-polarized, because the electric field is parallel to the plane of incidence. The interface conditions that can be derived from Maxwell's equations in integral form indicate that upon refraction at a surface without surface currents present, the wave remains p-polarized, so naming it a "mode" is an apt description. For the TE mode, the electric field is perpendicular to the plane of incidence. Light in the TE mode is said to be s-polarized, from the German word "senkrecht", meaning perpendicular. Light that is s-polarized also retains that property upon refraction between two media because of the continuity of the tangential component of the electric field at an interface.

When the wave is normally incident to an interface, both the electric and magnetic field in an isotropic medium are tangential to the interface and we speak of a "TEM" mode. It is sometimes useful to keep the notion of TE and TM in this case, to indicate the orientation of the electric field relative to a reference plane, which is usually the plane of the drawing.

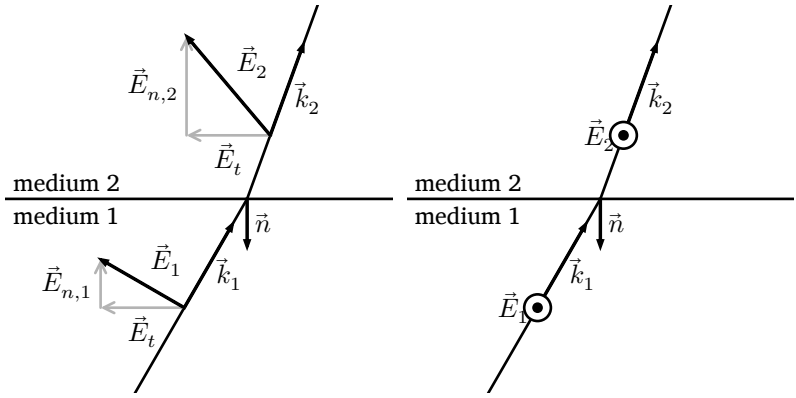

(a) TM mode or a p-polarized wave.

(b) TE mode or an s-polarized wave.

Fig. 2.1: An electromagnetic plane wave refracts at an interface between an isotropic medium (medium 1) and an anisotropic one, such as a liquid crystal (medium 2). The electromagnetic wave can always be written as a linear combination of two modes, the TM mode, shown in (a) and the TE mode shown in (b). Light is said to be p-polarized in (a) and s-polarized in (b). The electric field vectors shown in (b) are perpendicular to the plane of incidence, they are shown head-on.

2.2 Design software

In many engineering disciplines design software is used to evaluate the performance of a device before time is spent on actually fabricating it. Civil engineers e.g. might need to know if a beam of a bridge supports a certain load and where the beam experiences the strongest forces, so that it could be strengthened. There are many advantages to modelling beforehand, but it does require good models and familiarity with the software. In this section, the different programs used for modelling the liquid crystal beam-steering devices that are the subject of this thesis are listed and their goals and output briefly explained. A conceptually simple beam-steering device that uses parallel, planar electrodes will be used throughout the following paragraphs to visualize the simulation results from the various pieces of software.

2.2.1 Simulating the director field with the finite-element method

The finite-element method (FEM) is a numerical technique that approximates the solution of a differential equation on a domain, Ω, that has an edge, Γ. It does this by subdividing the domain Ω into smaller and simpler elements, which are called "finite elements" and choosing a set of simpler functions, the shape or basis functions, within each element to approximate the true function. The differential equation is simplified on the smaller elements, leading to a set of element equations. Finally, the element equations are assembled into larger system equations that model the entire structure and are solved numerically [2].

One of the great advantages of the finite-element method is the ability to model complex geometries accurately and improve the approximation in regions of interest without overly increasing the computational requirements. Because topological defects can occur in liquid crystals, this feature is highly interesting in the study of LCs. The LCP group of Ghent University uses FEM software to simulate the distribution of the director in a liquid crystal.

A. *Mesh generation*

Common examples of finite elements in two dimensions are triangles and rectangles, and tetrahedra and prisms in three dimensions. Dividing a geometry into finite elements is a process that is known as meshing. Software that uses

the FEM, does not necessarily incorporate meshing capabilities, instead leaving it to third party software. Comsol Multiphysics is an example of finite-element analysis (FEA) software that includes a module for meshing the geometry. The software the LCP group of Ghent University uses to simulate the director profile of a liquid crystal relies on third party software for meshing geometries, such as the commercial software Gid [3]. It is often desirable to run programs like these non-interactively and without the graphical user interface (GUI) ("headless"), merely passing it an input file that describes in a textual format the geometry to be meshed and passing it options that determine the mesh size. This functionality is used for example in chapter 5, where a "parameter sweep" is executed over the height of a glass layer to determine the error when simulating a director field. A parameter sweep is a series of simulations where the different simulations vary only in a few parameters. Gmsh [4] is an open-source mesh generator that I considered more useful because it not only has this headless and non-interactive functionality, but also has advanced scripting possibilities to generate geometries and meshes more efficiently. It is the meshing software that has been used throughout these PhD studies after a short period in which it was compared to GiD.

As an example of the meshing process, consider figure 2.2, which shows a two-dimensional geometry and the generated mesh that is related to it. The geometry of figure 2.2a corresponds to a liquid crystal encapsulated between two glass substrates. The interface between the LC medium and the glass medium at the top is covered by a homogeneous electrode. This electrode is referred to as the ground or common electrode as all other electric potentials are given relative to the electric potential of this electrode. The glass–LC interface at the other side is only partly covered by electrodes, the so-called "steering electrodes". The glass and electrodes are covered by an alignment layer, which is not shown in figure 2.2. Because the alignment layers and the electrodes are very thin compared to the LC layer, their structure can not be distinguished in the generated mesh, even though some of the edges have been labelled in the software (and the figure) as having the properties of an electrode, alignment layer or both. Electrodes are typically less than 50 nm thick and alignment layers about 100 nm, which is at least an order of magnitude smaller than typical LC layer thicknesses (1 µm–10 µm), so the thickness of these layers often does not have to be modelled in the mesh. Even for thin LC layers, the thickness of alignment layers could be ignored, provided

their voltage shielding effect is taken into account [5]. Figure 2.2a shows that the steering electrodes consist of three pieces: a large electrode that is in contact with two smaller electrodes at its sides. The smaller electrodes are referred to as the "addressing electrodes", because the electric potential is defined on them and they are assumed to be excellent conductors. The larger electrode is assumed to have a higher resistivity and so the electric potential over it is a function of the potential of the addressing electrodes and the LC layer over it, which acts as a distributed capacitor. By applying different electric potentials to the smaller electrodes, an electric current will flow between them through the larger electrode which then acts as a potential divider. For energy reasons, it is desirable to make this current small, so the bridge electrode is ideally highly resistive. The two addressing electrodes should be sufficiently conductive to ensure that their potentials match the externally applied voltages closely.

Remark that the mesh is inherently unitless: meaning to the x and y coordinates is given by the simulation software, just like various material properties are associated to the different domains through their labels.

When creating the mesh, it is not always necessary to model the entire structure. In this case e.g., only one unit cell of the periodic structure needs to be modelled: periodic boundary conditions are applied to the left and right edges of the mesh. The upper glass substrate also does not need be modelled, because the electric field above the ground electrode does not influence the electric field in the LC region. This is the reason the mesh in figure 2.2b does not include that part. Due to the limited size of the lower electrode, the lower glass substrate is required however, and just how big this domain should be is a matter of iteration and experience. In chapter 4 a study of the required thickness will be presented, which is a parameter sweep of the thickness of the lower glass layer that makes heavy use of the possibility to script the meshes generated with Gmsh.

B. *Simulation of a director field*

In the numerical treatment of liquid crystals, the equilibrium solution of the liquid crystal orientation is sought by minimizing the free energy of a liquid crystal, $\mathcal{F}$. It is defined as the volume-integral of the elastic energy density, f_d, the electrostatic energy density, f_e, and the surface-integral of the surface

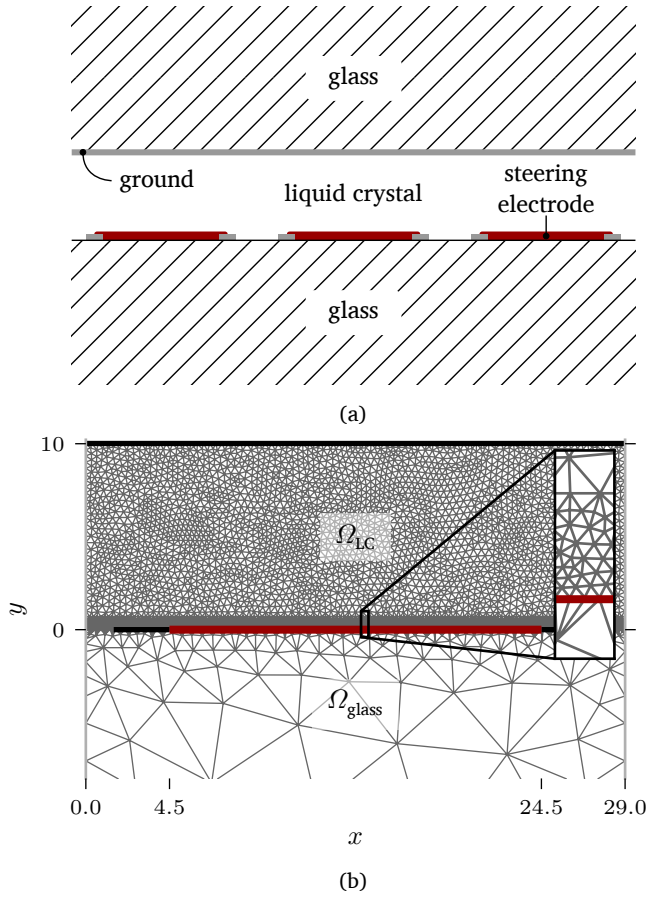

Fig. 2.2: A liquid crystal cell geometry and its representation as an unstructured mesh. The geometry is assumed to be periodic in the horizontal direction and the glass layers extend in the vertical direction. The mesh only represents one period. The red electrode material is characterized by a sheet resistance (material with limited conductivity). The narrow grey or black electrodes are perfect conductors.

anchoring energy, f_s [6]:

$$\mathcal{F} := \int_{\Omega} \{f_d - f_e\} + \int_{\Gamma} f_s. \tag{2.1}$$

The electrostatic energy density,

$$f_e := \frac{1}{2}\varepsilon_0 \left(\vec{E} \cdot \bar{\bar{\varepsilon}} \cdot \vec{E}\right), \tag{2.2}$$

describes the energy associated with quasi-static electric fields, $\vec{E}$, that permeate the liquid crystal. The permittivity tensor of the liquid crystal, $\overline{\overline{\varepsilon}}$, is a second order tensor that describes the dielectric properties of the anisotropic LC. The Oseen–Frank elastic energy density describes the energy associated with elastic deformations of the LC. It can be written in terms of the director, $\vec{L}$, or in terms of the Q-tensor. The Q-tensor, also known as the order parameter tensor, is a symmetric and traceless matrix that describes the orientation of a liquid crystal, which can be biaxial, and the local order parameters [7]. It can be written as:

$$\overline{\overline{Q}} = \begin{pmatrix} q_1 & q_2 & q_3 \\ q_2 & q_4 & q_5 \\ q_3 & q_5 & -q_1 - q_4 \end{pmatrix}, \tag{2.3}$$

in which the elements take the following form:

$$\begin{aligned}
q_1 =& S_1 \cos^2\theta \cos^2\phi + S_2(\sin\phi\cos\psi - \cos\phi\sin\psi\sin\theta)^2 - \frac{1}{3}(S_1 + S_2) \\
q_2 =& S_1 \cos^2\theta \sin\phi\cos\phi \\
& - S_2(\cos\phi\cos\psi + \sin\phi\sin\psi\sin\theta)(\sin\phi\cos\psi - \cos\phi\sin\psi\sin\theta) \\
q_3 =& S_1 \sin\theta\cos\theta\cos\phi + S_2 \sin\psi\cos\theta(\sin\phi\cos\psi - \cos\phi\sin\psi\sin\theta) \\
q_4 =& S_1 \cos^2\theta \sin^2\phi + S_2(\cos\phi\cos\psi + \sin\phi\sin\psi\sin\theta)^2 - \frac{1}{3}(S_1 + S_2) \\
q_5 =& S_1 \cos\theta\sin\theta\sin\phi - S_2 \sin\psi\cos\theta(\cos\phi\cos\psi + \sin\phi\sin\psi\sin\theta)
\end{aligned}$$

The parameters S_1 and S_2 are the scalar order parameters that quantify the degree of order about the directors of a biaxial LC. The angles θ, ϕ and ψ are the Tait–Bryan angles, sometimes also referred to as the Euler angles, and are illustrated in figure 2.3. Figure 2.3 also shows the relation between these angles and the directors of a biaxial LC. If the liquid crystal were uniaxial it would be represented by a cylinder rather than a board and there would be only one director, which is given by:

$$\vec{L} = (\cos\theta\cos\phi, \cos\theta\sin\phi, \sin\theta)^T \tag{2.4}$$

The angles θ and ϕ are referred to as the tilt and twist of the director respectively.

Describing the distortion energy density in terms of the director is more straight-forward, but the Q-tensor approach has the advantage of retaining

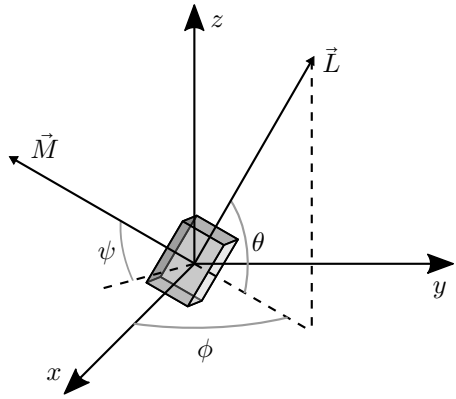

Fig. 2.3: The orientation of two directors, $\vec{L}$ and $\vec{M}$, of a biaxial liquid crystal (represented as a board) relative to a reference frame (the orthonormal xyz-axes) can be given in terms of the Tait–Bryan angles ϕ, θ and ψ.

the equivalence of $\vec{L}$ and $-\vec{L}$, as well as allowing biaxial LCs to be modeled. A downside of the Q-tensor is that it cannot be easily visualized, so conversion to the director is often still required: the Q-tensor, that is given on the nodes of the unstructured mesh, is interpolated onto a rectangular grid, after which conversion of the Q-tensor to the director is performed for post-processing and visualization. The order in which these conversion steps are performed (interpolation followed by transformation) is important: the other way around could lead to non-sensible results, because of the inversion symmetry of the director, $\vec{L} = -\vec{L}$.

The LCP group of Ghent University uses the Q-tensor FEA program developed by R. James et al. [8] for this purpose. This software, written partly in Matlab, partly in C++, calculates the five non-redundant elements of the Q-tensor in each of the nodes of the unstructured mesh.

Other than a mesh, the software requires only two configuration files, one that holds the properties of the liquid crystal used in the simulation and another, the mesh description file, that assigns meaning to the labelled elements of the mesh: what is the anchoring strength of the alignment layers, what orientation do they impose to the director, what electric voltages are applied to the electrodes, …. In all FEM simulations shown hereafter, the liquid crystal domain has the properties of the liquid crystal mixture known as E7. In [9], P. Yeh and C. Gu list the quasi-static electric field properties that are used in all these simulations. These values are reproduced in table 2.1 for

easier referencing. The refractive indices at 633 nm and at room temperature are listed in table 2.2, together with the glass transition temperature and clearing temperature.

As part of this PhD, the Q-tensor program has been extended and now has the possibility to model resistive electrodes: electrodes on which the electric potential is a continuous function of space. Continuing the example that was used at the end of section 2.2.1.A, the bridge electrode is labelled in the software as a resistive electrode, on which the electric potential varies linearly between the potentials defined at the addressing electrodes at its sides. A linear variation of the potential follows from neglecting the capacitive current (to charge the LC) in comparison to the conductive current in the resistive electrode. This is valid for the case of low frequencies. A homogeneous current density leads to a linear variation in the potential. The addressing electrodes are set at 0 V and 10 V, relative to the common electrode, values that are given in the mesh description file.

The output of the Q-tensor program applied to this beam-steering device with a resistive electrode is visualized in figure 2.4. The small black sticks represent the orthogonal projection of the director, $\vec{L}$, on the xy-plane. The inset axes shows the original director profile of a section that has been enlarged 6 times. It illustrates that the Q-tensor program calculates the director not only in the nodes of the triangular mesh, but also midway each side of the triangles. This is known as an unstructured mesh with second order elements. On the main axes, the director profile is visualized on a rectangular grid. In both the main axes and the inset, the electric potential distribution is shown through contourlines and -surfaces. Because the range of electric potential shown in the inset is small, a different color scheme is used to allow distinction between lower and higher potentials. The electrodes have been drawn over the result set, in bright green for the fixed potential electrodes and bright

Table 2.1: Quasi-static electric field properties of the nematic liquid crystal E7

$\varepsilon_\perp$	$\varepsilon_\parallel$	k_1 (pN)	k_2 (pN)	k_3 (pN)
5.1	19.6	11	10.2	16.9

Table 2.2: Refractive indices of E7 [10] and its transition temperatures [11].

$n_\mathrm{e}(633\,\mathrm{nm}, 25\,^\circ\mathrm{C})$	$n_\mathrm{o}(633\,\mathrm{nm}, 25\,^\circ\mathrm{C})$	T_g (°C)	$T_{\mathrm{N-I}}$ (°C)
1.7302	1.5188	−64	61

red for the resistive electrode. The reader is reminded that they do not have any thickness in the mesh, the overlay merely serves as a visual aid to locate the electrodes. Note that the equipotential lines cut the resistive electrode at regularly spaced intervals, which is a consequence of making the electric potential linearly related to the potentials at the side electrodes.

Figure 2.4 clearly shows that the director is more perpendicular to the two glass–LC interfaces on the right side, where the potential over the liquid crystal is larger. This is a consequence of the positive dielectric anisotropy of E7: when $\varepsilon_{\parallel} > \varepsilon_{\perp}$, the director will preferentially be oriented along the electric field, which is perpendicular to the equipotential lines, as $\vec{E} = -\nabla V$. So the tilt, θ, which is the angle between the director's main axis and a reference plane, in this work always chosen to be the plane of the ground electrode, increases from left to right in figure 2.4. This influences the optical path length (OPL) as light travels through this LC slab and thus also the phase of the wave. The phase of an x-polarized plane wave as it propagates from the bottom glass through the LC can be visualized by using the Jones matrix formalism.

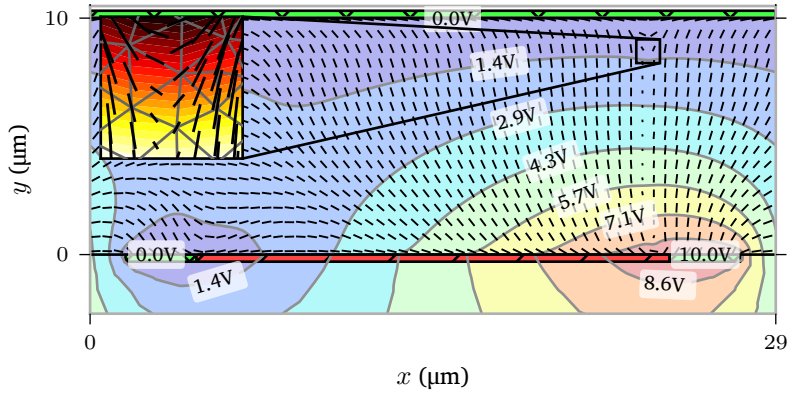

Fig. 2.4: An illustration of the director field, $\vec{L}(\vec{r})$, shown as a series of little black sticks, overlaid on the isopotential contours of the electric potential distribution, $V(\vec{r})$. The inset shows the original dataset defined on the triangular mesh and illustrates a topological defect of charge -1/2. A $+1/2$ defect can be found to the left of the addressing electrode that is held at 10 V.

2.2.2 Simulating light propagation

The propagation of light through anisotropic media can be simulated with a variety of techniques. During this PhD, three numerical techniques were used which are described in sections 2.2.2.A to 2.2.2.C. In section 2.2.2.D the output of the previous paragraphs will be used to obtain the distribution of light at a plane far away from the simulated device.

A. *Jones formalism*

The Jones matrix formalism is a simple technique that represents a wave, $A\cos(\omega t - kz)$, as a phasor, $A\exp(jkz)$, one for each component of the electric field, and allows calculating the phasor representation of the wave after it has propagated through some medium. Several useful properties can be derived from it, such as transmitted intensity and type of polarization. In a geometry such as the one shown in figure 2.4, it can be used to calculate the phase and intensity of the x- and z-component of the electric field of light when it emerges from the structure, assuming it was fully polarized upon incidence.

It is not necessary to understand all details of the Jones formalism to understand its output. Only the basis is touched here and the reader is referred to the literature for a more in-depth explanation ([12, chapter 2.2], [13, pages 57-62]). In the Jones matrix formalism, the electric field from a wave propagating along the y-axis, is represented by a 2×1 column vector, $\mathbf{J} = [E_x, E_z]^T$. Any layer through which it propagates is represented by a 2×2 matrix, $\mathbf{M}$ and the result of propagating through that layer is obtained by matrix multiplication: $\mathbf{J}_{\text{out}} = \mathbf{M} \cdot \mathbf{J}_{\text{in}}$. A plane wave travelling along the y-axis and incident on the LC slab from figure 2.4 can be thought of as a series of beams with different x-coordinates travelling along the y-axis that each encounter a slightly different material. The Jones matrix for one such columnar material can be calculated by cutting the column up in small vertically stacked pieces, where each piece is assumed to have a homogeneous director orientation. The Jones matrices of these small pieces are multiplied to obtain the Jones system matrix for one beam travelling along the y-axis. So in order to use the Jones matrix formalism, the inhomogeneous LC medium has essentially been approximated by a system of simpler homogeneous sublayers. Using the director field obtained from the quasi-static electrical simulation

of the LC and the refractive indices from table 2.2, the phase of the wave at the upper glass–LC interface is calculated and shown in figure 2.5. The figure shows the phase of both transverse components of the electrical field of the optical beam, as well as the intensity of the x-component of the electric field relative to the intensity of the incident x-polarized light. The location of the addressing electrodes is illustrated by the green patches that span a range of 3 µm, just like in figure 2.4. The figure shows that a small fraction of the incident x-polarized light is converted to z-polarized light near the addressing electrode on the right, which is clear from the steep decrease of $|E_x|^2$. This sharp dip is due to the rapid reorientation of the director at that location, which is shown in figure 2.4, and is the result of conflicting orientations imposed by the electric field and the pretilt. As the figure shows, a nearly vertical line exists where the director's tilt changes rapidly from nearly 90° to 0° and back to 90° as the line is crossed from left to right in the figure. Linearly polarized incident light will experience a change in polarization there.

The x-polarized light experiences a larger OPL closer to the left electrode so the phase there lags behind the phase on the right side. The figure reveals that this phase lag amounts to about 6π, which is very close to the theoretical value of the optical path difference (OPD) expressed in radians, being $2\pi\Delta nd/\lambda$. Finally, there is a region over the resistive electrode, which lies between the green boundaries, where the phase is approximately linearly increasing. The wavefront in this region makes an angle with the glass substrate equal to $\arctan(\Delta\phi/(2\pi\Delta x))$. This implies that the x-polarized light at the output is directed at an angle of about 3.6° relative to the glass–LC normal. This is an optimistic scenario: the performance of this resistive beam-steerer will be decreased due to the non-linearity in the overall slope, which will result in an angular spread of the emerging light.

The Jones matrix formalism is often used because of its simplicity. It is ill-suited for 3D problems though and even for 2D problems where the thickness of the LC layer approaches the lateral dimensions, because the formalism does not take into account beam deflection within a medium.

B. *Beam propagation method*

The beam propagation method (BPM) is a numerical technique that allows simulating the propagation of guided waves in inhomogeneous media and

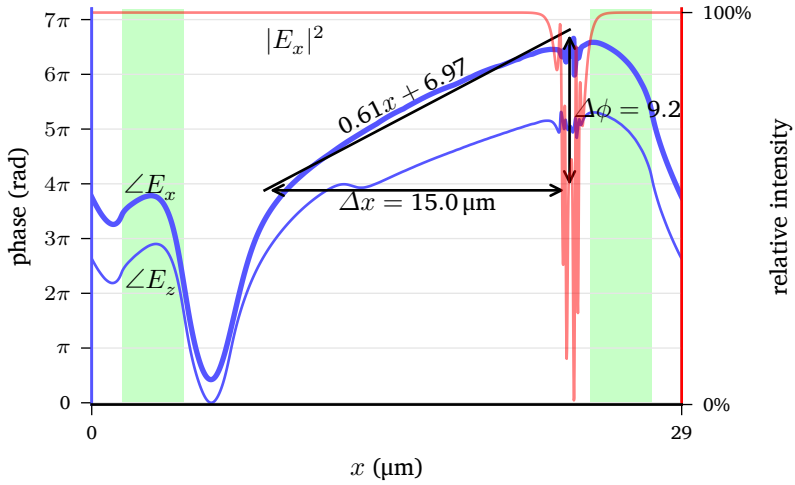

Fig. 2.5: Phase and intensity of light emerging from the device when x-polarized light is perpendicularly incident from the lower glass–LC interface of figure 2.2a. The green areas denote the position of the addressing electrodes.

relies on the slowly varying envelope approximation that is justified when the refractive index varies slowly along the propagation direction [14]. Since its introduction at the end of the 70s, it has seen numerous variations on the numerical techniques that are employed, such as the finite-difference BPM (FD-BPM) [15], finite-difference vector BPM (FD-VBPM) [16] and finite-element BPM (FE-BPM) [17]. Within our research group a full-vector and wide angle beam propagation method software has also been developed [18]. One of its attractive features for this research is that it allows beam propagation through inhomogeneous anisotropic linear media such as liquid crystals. Furthermore, it is a finite-element method, so it can easily interface with the Q-tensor program described in section 2.2.1.B. Attempts have been made to use it on the blazed grating structure described in chapter 3, but the simulation was unstable due to the rapid index change at the interface between the grating and the liquid crystal.

C. *Finite-difference time-domain method*

Another alternative to simulate beam propagation is given by the finite-difference time-domain (FDTD) method. The electromagnetic fields are solved for in a leapfrog manner that uses interweaved grids for the electric

and magnetic fields. The FDTD method is often used when diffraction and refraction cause the propagation of light in transverse directions to be significant, such as in the presence of discontinuities [19] or singularities and dislocations [20, 21] in liquid crystal cells.

Lumerical FDTD, a commercial-grade simulator based on the FDTD method is used in this thesis. It receives the spatially varying anisotropy information from the Q-tensor FEM program that was explained earlier. While the FDTD method is inherently a broadband technique, computing the fields in the entire structure for all wavelengths at the same time, in this chapter we only extract the computed phase profile of an x-polarized monochromatic wave ($\lambda = 633\,\text{nm}$) that is transmitted through the resistive electrode beam-steerer and compare it to the phase profile computed using Jones matrices.

Figure 2.6 shows the phase of the x-component of the electric field of the beam at the upper glass–LC interface after propagation through the LC layer, as computed by Lumerical FDTD. As with figure 2.5, the location of the addressing electrodes has been indicated by green patches. While the values are different, the graph shows a high degree of resemblance to its counterpart in figure 2.5, which was calculated with the simpler Jones matrix method. The actual phase values are not important, only the differences in phase are of importance. The reason for that is simply that the phase profile of the continuous wave could have been captured at a slightly different time, which would add an offset to all phase values. The most pronounced feature is that in the Lumerical result, there is also a region over the resistive electrode where the phase can be considered to be linearly increasing. The slope of this region, which has been chosen to be the same region as in figure 2.5, has been calculated by fitting a linear polynomial to it in a least-squares sense, just like in figure 2.5. The slope is nearly the same and would predict the optical plane wave to be travelling at an angle of about 3.4° relative to the device normal, which is a bit smaller than the 3.6° predicted by calculating the emergence angle using the Jones formalism.

Figure 2.6 also shows the intensity of the x-component of the electric field, relative to the incident power. There is a region near the left electrode where light seems to have been amplified. The phase at that point also varies rapidly, which indicates this is a region where constructive and destructive interference occur. The intensity over the resistive electrode is approximately 75 %, a value for which Lumerical FDTD has also taken into account the losses

from reflections at the various interfaces, unlike the Jones formalism.

D. *Far-field diffraction patterns*

The far-field diffraction pattern indicates to what angles monochromatic light is being redirected and with which intensities. It is an essential concept in the design of beam-steering devices.

Fourier optics shows that the far-field diffraction pattern, also known as Fraunhofer diffraction, can be obtained by taking the Fourier transform of the aperture distribution [22, chapter 4.3], which is the electric field, amplitude and phase, at an aperture.

Using this information, it can be calculated using the output from any of the three previously discussed light propagation simulation techniques. Because of mixed results with the BPM and the limitations of the Jones matrices, the far-field diffraction pattern is in this work extracted using Lumerical FDTD.

The computed far-field diffraction pattern of the resisistive electrode beam-steering device illustrated in figure 2.2 is shown in figure 2.7. The power of the incident beam of coherent light ($\lambda = 633\,\text{nm}$) is directed to specific angles, the so-called diffraction orders, which are given by the Bragg grating equation,

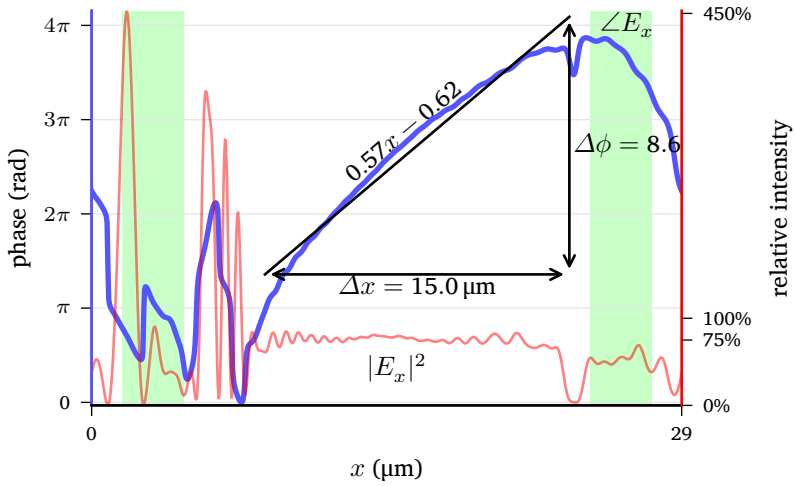

Fig. 2.6: Phase of the x-component of the electric field of the beam after emerging from the device.

$$m\lambda = \Lambda(\sin\theta_i + \sin\theta_o), \tag{2.5}$$

in which Λ is the period of the spatially repeating pattern, θ_i and θ_o are the angle of incidence and emergence respectively, relative to the grating normal, while λ, as usual, is the wavelength of light and m is an integer number called the "diffraction order". The relative strengths of these orders (how much power is radiated in each direction) is still governed by the actual shape and composition of the periodic structure, and this is what is shown in figure 2.7. Note that Lumerical FDTD simulates the *relative* strengths, being the power in an order divided by the power of the incident wave. As reflections from the glass–LC interfaces play a role, the sum of the power in the transmitted orders is not 100 %. The graph that zooms in on the region of interest (ROI) shows that most of the light is redirected to angles between 5° and 2.5° to the left of the grating normal. The emergence angle that was derived from the phase profile, using either the Jones matrix method or the output from Lumerical FDTD, falls nicely in this region. A small amount of power is radiated to angles around 15.2° to the right of the device normal, which could be attributed to the region *between* two resistive electrodes where the optical path length changes rapidly and in a sense that is opposite to the OPL change *over* the resistive electrode.

Note that in figure 2.7, there is almost no power in the TE mode (the maximum is less than 0.16 %). The reason for this is that the indicent light is polarized along the x-axis of figure 2.4, which is p-polarization, and very little conversion from p-polarized light to s-polarized light is occuring due to the birefringent liquid crystal.

E. *Summary of the simulation workflow*

The large variety of software and simulation techniques presented in the previous paragraphs might leave the reader confused. While in reality many of these programs have been used to obtain meaningful results, in essence there are only three problems that need to be solved:

1. the director field distribution,
2. light propagation through the device and
3. far-field calculations.

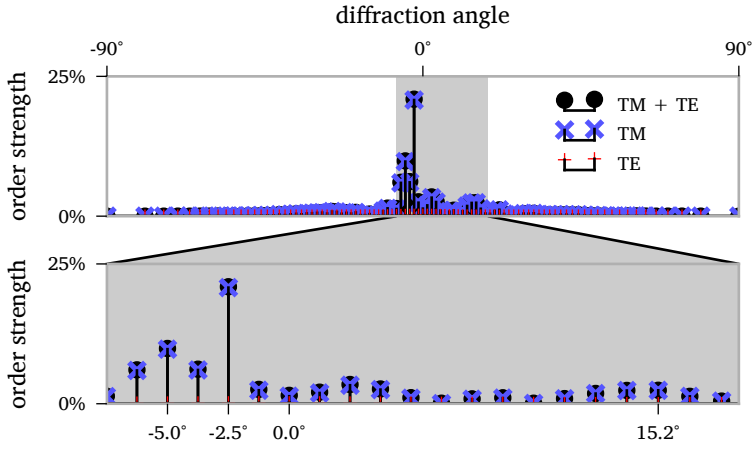

Fig. 2.7: The diffraction pattern of x-polarized light under normal incidence can be split in two components after emerging from the LC layer. The upper graph illustrates that there is only one region of interest, which has been enlarged in the lower graph.

Each of these problems can be tackled in several ways, but in this thesis the workflow is as follows. The director field distribution is simulated using the Q-tensor program described earlier. As this is a FEA program, it requires a pregenerated mesh, which is delivered by Gmsh. Using the simulated LC director field, light propagation through the device can be simulated, a problem that will be tackled using Lumerical FDTD. It uses the FDTD technique internally. The output from this step is the optical field close to the device. For applications, the optical field at a distance far away from the device is more useful. This last step, the conversion from the optical field close to the device to the far-field, is a problem that is typically handled by transforming the input using the Fourier transform. This transformation can be performed by many software packages, but Lumerical FDTD provides a useful module to handle this transformation as well, which allows us to solve the last two problems in the earlier list using the same software package.

2.3 Fabrication technology

In the first part of this chapter the simulation tools that are frequently used in this thesis were explained using the example of a beam-steering device

that uses an electrode with high resistivity. In this second part, general liquid crystal cell fabrication technologies are discussed. These have been used to create the devices that are the subject of the next chapters.

2.3.1 Overview of a cell assembly

An overview of a fabricated liquid crystal cell is shown in figure 2.8. It shows two glass substrates, the bottom of which features a series of patterned electrodes. The two substrates are bound together with an adhesive, such as ultraviolet (UV) curable glue, which is present at the outskirts of the cell (not visible in the figure). The adhesive typically contains small solid particles, so-called “spacers”, that ensure a small gap between the two substrates. The created cavity is filled with a liquid crystal by placing a small droplet of the material at the interface between the two substrates, which then seeps into the cavity by means of capillary forces. The substrates are offset, so that electric signals could be applied to the outer contacts.

The arrows indicate the preferential alignment direction at the interface for the director of a liquid crystal. The alignment direction is imposed by an alignment layer, which will be explained in section 2.3.4. When the arrows face each other, like in the figure, the alignment is said to be anti-parallel. When the same alignment technologies have been used on both substrates, this ensures an alignment of the director of a nematic liquid crystal that is free of elastic distortions, in the absence of electric field. This is illustrated in figure 2.9, together with the “parallel” alignment, where splay deformation is present.

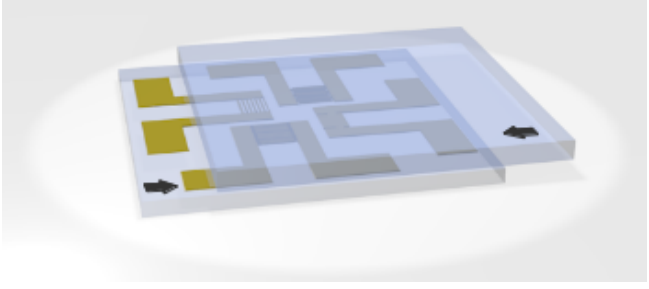

Fig. 2.8: An assembled liquid crystal cell with anti-parallel alignment of the director.

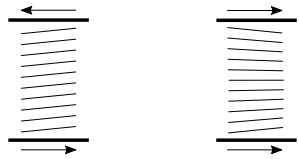

Fig. 2.9: Distribution of the director of a nematic liquid crystal in a cell with parallel substrates. All substrates have been treated with an alignment layer. In (a), one substrate is rotated so that the alignment reaches the energetically favourable anti-parallel state. In (b), "parallel alignment" is obtained, which introduces splay in the liquid crystal director.

2.3.2 Mask design

In chapter 3 a beam-steering device will be studied where the liquid crystal is sandwiched between two substrates and switched by only two electrodes that cover the entire surface area of the substrates. In chapters 4 and 5, devices will be discussed that require a more complex form of addressing the liquid crystal: more than two electrodes are used to switch the liquid crystal. The resistive electrode beam-steering device from the first part of this chapter is an example of this class of devices: it uses two addressing electrodes and a ground. Such devices, known as multi-electrode LC devices [23–26], require a specific layout of the electrodes on the substrates. These layouts can be made in several ways, but the most common method of fabricating is using UV lithography, which will be explained briefly in section 2.3.3. Prior to performing lithography, a layout of the electrode pattern must be designed and transferred to a holder that is suitable for the lithography process, such as a quartz or soda lime glass.

A great variety of software exists that allows designing these masks. Over the course of this PhD, all mask design was carried out using IPKISS version 2.4-alpha, which was developed at the INTEC Photonics Research Group of Ghent University [27]. One of its attractive features is the possibility to parameterize designs, such that once a geometry is properly designed, it can be easily altered to include minor variations such as changing the electrode widths.

To reduce the amount of patterned substrates that need to be made for electro-optic experiments using UV lithography, it is advisable to increase the number of electrode patterns on a single mask. My experience with

lithography allowed me to design masks that featured improvements over previous iterations. As an example, figure 2.10a shows a mask that was designed using AutoCAD by one of the researchers of the LCP group prior to the start of this PhD. It holds four electrode patterns, in which electrodes are interdigitated, as the magnification shows. The patterns differ in the spacing between the electrodes and the dimensions of the electrodes. The narrow interdigitated electrodes are attached to larger electrodes that lead to the edges of the design. Conductive wires can be soldered with greater ease to the large area these electrodes occupy at the sides. An ultrasonic soldering iron is used to solder to glass and my experience with it has shown that it is just manageable to solder wires manually to electrode pads of 2 mm by 2 mm that are spaced 1 mm apart.

The designs of the masks used for the work presented in chapters 4 and 5 of this thesis attempt to reduce the lithography load by making more optimal use of the space and taking into account the typical assembly process of a liquid crystal cell. Because the soldering pads in the older mask (figure 2.10a) are distributed over all sides, one pair per pattern per side, the placement of the upper substrate will render three pairs of soldering pads inaccessible and their associated electrode patterns cannot be used for electro-optical studies of LCs, as figure 2.8 shows. If the upper substrate were not as wide as the lower substrate, three regions could be used at best. With that in mind the asymmetric interdigitated electrode mask, shown in figure 2.10b, was designed. It allows testing three electrode patterns with varying dimensions even if the upper substrate is not cut and six if it is. The concentric arc design of figure 2.10c also features an improved use of the space: each series of concentric arcs requires eight electrodes to be tapered to the closely spaced arcs (arc spacing is on the order of 50 µm). The higher density of addressing electrodes requires some finesse during the soldering, but has proved to be manageable. These improvements to the masks reduce the amount of substrates that need lithography processing and thereby increases the yield.

2.3.3 Lithography

Lithography is a method by which a pattern can be imprinted or transferred to another substrate. With UV lithography, ultraviolet light is incident on a photosensitive material, known as a resist, that is masked in certain areas

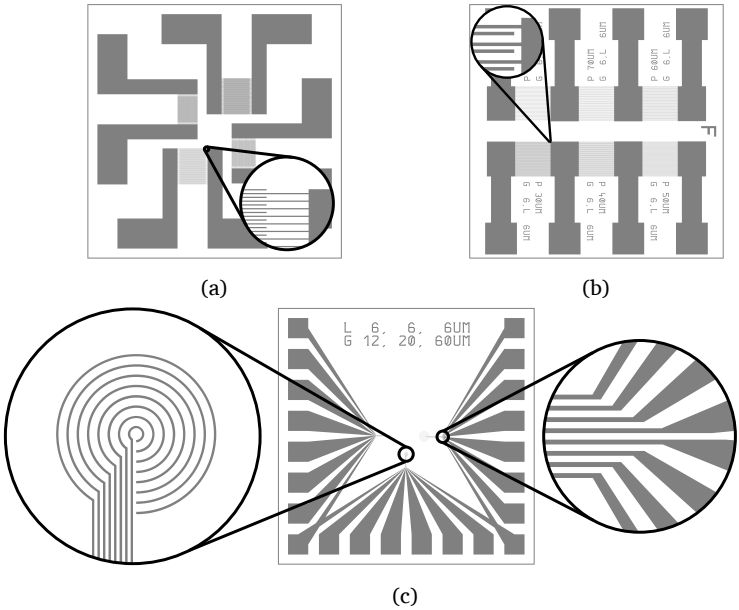

Fig. 2.10: Examples of mask designs, suitable for 2.54 cm by 2.54 cm substrates. (a) A four-sided mask featuring four interdigitated electrode patterns. (b) A two-sided mask featuring six interdigitated electrode patterns, where each ROI is 3 by 3 mm^2. (c) A design featuring concentric circular arcs. Three such designs are present on the mask, each featuring 8 arcs. The soldering pads at the edge of the design are tapered to the finely spaced inner arcs. The diameter of the largest arc set in this mask is 1 mm.

by placing the electronic masks that were explained earlier between the UV source and the photosensitive material.

Figure 2.11 shows schematically the process of UV lithography in both positive and negative photoresists. The lithography process is finished after the 3rd step and shows that negative and positive photoresists lead to complementary resist profiles. After patterning of the resist, post-processing steps such as etching or metallization could take place. Metallization is typically only done with negative photoresists, because the liftoff process works better when there is a small underetch. The LCP group usually buys float glass substrates that are already coated on one side with indium tin oxide (ITO), an optically-transparent and conductive oxide that is used in nearly all liquid crystal displays (LCDs). If this transparent conductor is required, the lithography steps using positive photoresist are executed. For situations where a different electrode material is desired, such as gold or silver which

have a higher conductivity, photolithography using negative photoresists is recommended.

An alternative to photolithography using negative photoresists is given by image reversal. The resist is positive and can be used as such, but by adding two extra processing steps the resist can be used as if it were a negative photoresist. The two extra steps that are added to the lithography process shown in figure 2.11, are the reversal bake in which the exposed photoresist crosslinks and the flood exposure step where the entire photoresist is exposed to UV light, thereby making the non-crosslinked positive resist soluble to the developer solution. This is shown schematically in figure 2.12.

Image reversal requires some fine-tuning, just like normal lithography. Parameters that have not been optimized could lead to severe undercuts of the resist, that would even allow fine resist tracks to be washed away. An example of this is shown in figure 2.13, which is a micrograph of the tapering section shown in figure 2.10c.

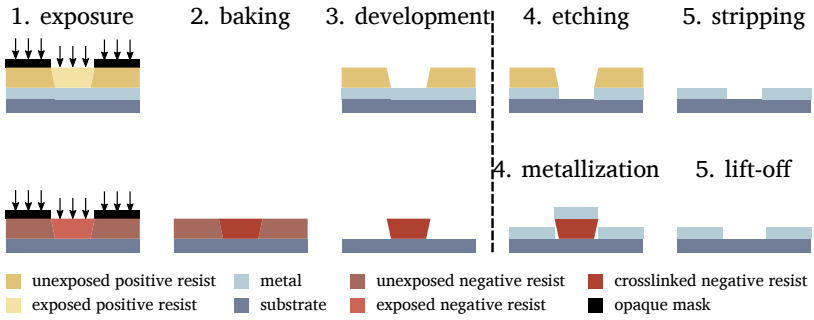

Fig. 2.11: The patterning of a metal using lithography and post-processing. The lithographic process is shown for positive (top) and negative (bottom) photoresists. Lithography is complete after step 3.

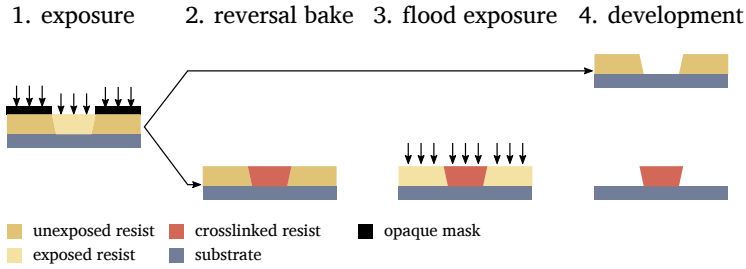

Fig. 2.12: A photoresist for image reversal can be used both as a positive tone resist and as a negative tone.

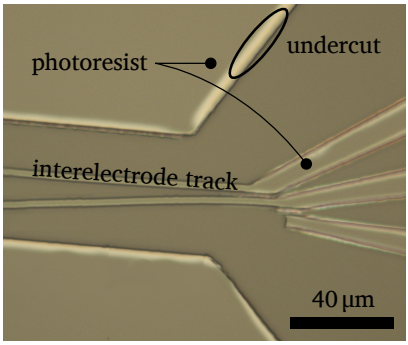

Fig. 2.13: This micrograph shows the tapering region that is enlarged in figure 2.10c after the resist has been developed. Underexposure during the first exposure step of image reversal could lead to a severe degree of undercut: in this example, interelectrode tracks can move freely over the substrate and are easily broken.

Prior to the deposition of the image reversal resist (AZ5214E from Micro-Chemicals), the adhesion promotor Ti-prime is applied to the glass substrates: it is spincoated at 3000 rpm during 40 s, after which the solvent from it is evaporated by having the spincoated substrate rest on a hotplate set at 120° for 3 min. The reversal resist is spincoated subsequently, using the same spinning parameters, but is dried at a temperate of 95°. The image reversal parameters that were used for the devices made as part of this PhD, are listed below.

- initial exposure: 22 s, at 1.4 W (measured behind the mask, on the resist)
- reversal bake: 3 min at 120°, on a hotplate
- flood exposure: 50 s, at 5 W
- develop: 18 s in a 1:3 volume ratio of AZ400k developer to deionized water

The exposure doses differ between the first and third step, because during the initial exposure, the mask is inserted, which reduces the power of the UV light (320 nm) that is incident on the substrate considerably: from 5 W to 1.4 W. The electronic mask is made on a soda lime glass that is 2.3 mm thick (JD Photo Data).

As an example, figure 2.14 shows a micrograph of a patterned substrate featuring interdigitated metallic electrodes. It is not uncommon that some

electrodes get shorted during the lithography, as the figure shows. Electrical shorts and other types of lithography errors render a region around these electrodes useless, although in the case of a sufficiently small short, such as the one shown, an attempt can be made to salvage the substrate by running a sufficiently high current through the short which may rupture the short due to Joule heating.

2.3.4 Liquid crystal alignment technologies

Once a mask is designed and transferred to a substrate, the substrate usually requires pre-treatment to ensure a uniform alignment of the liquid crystal director. This is done by coating the substrate with an alignment layer. Rubbing (section 2.3.4.A) is one of the most well-known and oldest ways to obtain an alignment layer. The use of photosensitive materials lies at the basis of the photoalignment technology (section 2.3.4.B), which is a non-contact method, unlike rubbing. There exist other ways to ensure homogeneous alignment, such as inscribing microgrooves or micropatterns in the substrate [28] and oblique evaporation of silicon oxide [29, 30]. In this thesis, only rubbing and photoalignment have been used so these will be explained briefly.

A. *Rubbing*

The process of rubbing involves coating a substrate with a polymer with long molecular chains, annealing it and subsequently rubbing a piece of cloth with short fibers “gently” over the coated side in a uniform fashion. Depending on the spincoated material, a pretilt and pretwist could be generated that is

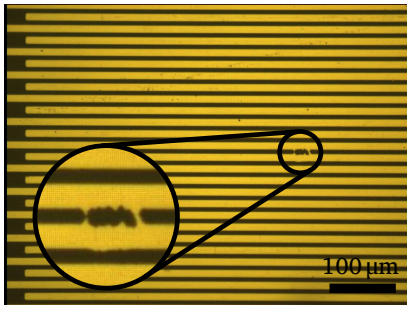

Fig. 2.14: One of the common errors during lithography: the accidental creation of an electric short between otherwise unconnected electrodes.

either perpendicular to or parallel to the direction in which the cloth was pulled [31]. A hardening or crosslinking step is usually required to ensure the tilt and twist of the chains is preserved when a liquid crystal flows over it.

Samples in this thesis that are aligned by means of rubbing had nylon applied to them, dissolved in trichloroethanol in a 1 % ratio by weight. Spincoating this material on an ITO-coated float glass at 3500 rpm, results in a layer thickness of approximately 52 nm, a value interpolated from the measurements shown in table 2.3. When a fibrous cloth is dragged over it, it results in an alignment direction that is parallel to the rubbing direction.

B. *Photoalignment*

An alternative alignment technique is that of photoalignment, which unlike rubbing does not create electrostatic charges, that could damage sensitive electronics such as thin film transistors in active matrix LCDs. One of the problems photoalignment also solves is the ambiguity of the statement that a coated surface is "gently" rubbed, a catch-phrase that occurs in many liquid crystal articles and patents. The compressibility of the cloth could play a role, and as the cloth could become contaminated over time, results from using the same rubbing cloth might not be reproducible. With photoalignment, the illumination dose and angle play a direct role in the anchoring properties, while remaining easily quantifiable, verifiable and repeatable.

The first photopatterned optical elements appeared already in 1977, but only gained attention from the liquid crystal display industry in the 1990s [32, chapter 1]. Since then, many improvements have been made. The LCP group from Ghent University has had its first experiences with the technology in 2012 [33], but several processing iterations were required to get consistent results on areas of approximately 1 square inch: to ensure homogeneous alignment, our cleanroom processing steps require the activation of the surface of the substrate using a plasma-treatment before spincoating the photosensitive material. Figure 2.15 shows a series of images of planar glass substrates that were all photoaligned and illustrates the need for plasma treatment in our

Table 2.3: Nylon layer thickness after spincoating, measured using ellipsometry. The error on the thickness is ± 0.1 nm.

spin speed (rpm)	900	1200	1800	2400	3600
layer thickness (nm)	133.8	100.7	72.5	60.7	49.3

processing: the plasma treatment activates the surface of the cleaned substrates and allows the photosensitive material to spread more uniformly over the substrate. To activate the substrates, they are placed in the plasma chamber of a Pico plasma system (Diener electronic GmbH) in which a plasma is generated for 24 s using 190 W to generate the plasma*. The plasma chamber is filled with air and held at a pressure of 0.8 mbar. Shortly after this treatment, the photosensitive material PAAD-22 (purchased from BEAM Co.), which has an absorption peak at 366 nm, is deposited on the substrates by spincoating the solution at 3000 rpm for 60 s. To evaporate the remaining solvent quickly, the substrates are placed on a hotplate for about 3 minutes at 100 °C, which is below the boiling point of the dimethylformamide (DMF) solvent in which the photosensitive substance is dissolved. The coated substrates are then irradiated with polarized UV light, using the unfiltered spectrum of the (broadband) bulb of an Omnicure series 1000, using an irradiation dose of $5\,\mathrm{W\,cm^{-2}}$. The resulting preferential orientation of the director is perpendicular to the polarization axis.

Remark that the photosensitive alignment material used for the cells shown in figure 2.15 is SD-1 [34]. The need for a plasma treatment has been found for both SD-1, as well as BEAM Co.'s commercially available PAAD-22. No references in literature have been found for the need of a plasma treatment for either material, so it seems related to our processing.

Finally, the colors in figure 2.15 originate from the birefringence of the liquid crystal which is made visible by placing the substrates between crossed polarizers (hence, the darkness of the surroundings), ensuring the director is not aligned with either transmission axis of the polarizers. When the director is aligned with either polarizer, the cell appears dark, as in figure 2.15f. If the director was not uniformly aligned, some light would be transmitted in this configuration, due to the birefringence of the LC layer.

2.3.5 Polarized light microscopy

To study liquid crystals, polarized light microscopy is often used. The technique is not just limited to LCs: other birefringent materials can be studied with it as well.

*The Pico plasma system used in our cleanroom generates 200 W maximum at 40 kHz, even though the inner chamber has 300 W engraved. This has been confirmed via e-mail, using the device's serial number (SN70138).

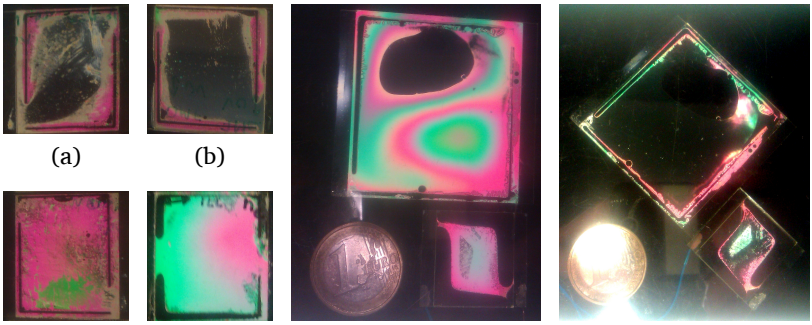

Fig. 2.15: Photoaligned cells between two crossed polarizers. Cells (a) to (c) have not been treated with a plasma prior to spincoating, the cells shown in (d), (e) and (f) have. The solvent for the photosensitive material SD-1 used in (a) and (c) is N-Methyl-2-pyrrolidone (NMP), in (b) dimethylformamide (DMF). The cells shown in (d)-(f) have been treated with the same mixture as cell (a), after plasma treatment.

When a uniformly aligned nematic liquid crystal sample is placed under the objective of an ordinary light microscope, no special features are observed: the sample is optically transparent. When two polarizers are introduced in the optical path, one before the sample, one after, with the transmission axis of the second polarizer perpendicular to that of the first, a series of colors is visible, which change when the sample is rotated.

These colors have the same origin as the bright colors shown in figure 2.15: the birefringent nature of the LC changes the polarization of the incident linearly polarized light. The resulting polarization depends on the wavelength, which means that after passing through the liquid crystal a continuum of "polarization ellipses" exists for each wavelength of the lamp used in the microscope to illuminate the sample. A polarization ellipse is the most general form of polarization and can be interpreted as the path outlined by the electric field vector of the electromagnetic wave at a plane fixed in space when observed for some time. Linear polarization is a special case where the polarization ellipse has collapsed to a line. The continuum of polarization ellipses is forced through the second linear polarizer, also sometimes referred to as the "analyzer", which collapses the polarization ellipses to linear polarization and thereby decreases the intensity of some wavelengths of which the polarization ellipse is poorly matched to the transmission axis of the second polarizer. This

is schematically illustrated in figure 2.16.

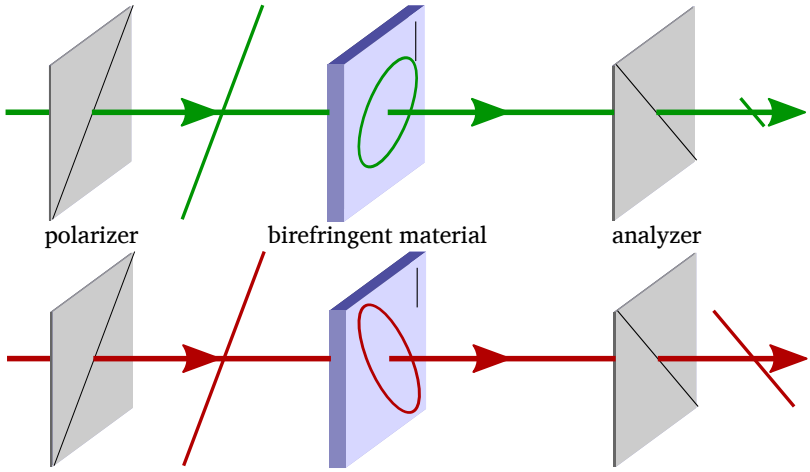

Fig. 2.16: Schematic illustrating the appearance of colors in birefringent samples when observed between crossed polarizers. In the top row, linearly polarized green light is transmitted through a birefringent sample, which changes its polarization state. After passing through the analyzer, a small fraction of this light is transmitted. A linearly polarized red beam of light passing through the same sample will experience a different reduction in power, because its polarization state will be different after passing through the sample. The transmission axis of the polarizers is indicated with a black line. The optical axis of the birefringent sample is shown with a small black line.

Placing a birefringent sample between crossed polarizers under the microscope can teach us many things, such as the direction of the optical axis and the location of defects, places where the director cannot be defined uniquely.

2.4 References

1. Saleh, B. E. and M. C. Teich, *Fundamentals of photonics*. John Wiley & Sons, 2007 (cited on p. 21).
2. Jin, J., *The finite element method in electromagnetics*. Wiley-Interscience, John Wiley & Sons, New York, 2002 (cited on p. 23).
3. Melendo, A., A. Coll, M. Pasenau, E. Escolano, and A. Monros, *Www.gidhome.com*, [Online; accessed Jun-2016], 2016. [Online] (cited on p. 24).
4. Geuzaine, C. and J.-F. Remacle, "Gmsh: A 3-d finite element mesh generator with built-in pre-and post-processing facilities", *International Journal for Numerical Methods in Engineering*, vol. 79, no. 11, pp. 1309–1331, 2009 (cited on p. 24).
5. Jiao, M., Z. Ge, Q. Song, and S.-T. Wu, "Alignment layer effects on thin liquid crystal cells", *Applied Physics Letters*, vol. 92, no. 6, p. 061 102, 2008 (cited on p. 25).
6. James, R. W. L., "Modelling of high resolution liquid crystal devices", PhD thesis, University College London (University of London), 2006 (cited on p. 26).
7. Mottram, N. J. and C. J. Newton, "Introduction to Q-tensor theory", *ArXiv preprint arXiv:1409.3542*, pp. 1–24, 2014 (cited on p. 27).
8. James, R., E. Willman, F. A. Fernández, and S. E. Day, "Finite-element modeling of liquid-crystal hydrodynamics with a variable degree of order", *Electron Devices, IEEE Transactions on*, vol. 53, no. 7, pp. 1575–1582, 2006 (cited on p. 28).
9. Yeh, P. and C. Gu, "Optics of liquid crystal displays", in *Optics of liquid crystal displays*. John Wiley & Sons, 2010, vol. 67, pp. 3–10 (cited on p. 28).
10. Li, J., C.-H. Wen, S. Gauza, R. Lu, and S.-T. Wu, "Refractive indices of liquid crystals for display applications", *Journal of Display Technology*, vol. 1, no. 1, pp. 51–61, 2005. [Online] (cited on p. 29).
11. Mierzwa, M., M. Paluch, S. J. Rzoska, J. Zioło, and U. Maschke, "Ordering effect on dynamics in glass-forming mixture of liquid crystals", in *Soft Matter under Exogenic Impacts*, Rzoska, S. J. and V. A. Mazur, Eds. Dordrecht: Springer Netherlands, 2007, pp. 201–214. [Online] (cited on p. 29).
12. Thévenaz, L., *Advanced fiber optics: Concepts and technology*. EPFL press, 2011 (cited on p. 31).
13. Collett, E., "Field guide to polarization", SPIE Washington, 2005 (cited on p. 31).
14. Xu, C. and W. Huang, "Finite-difference beam propagation method for guide-wave optics", *Progress In Electromagnetics Research*, vol. 11, pp. 1–49, 1995 (cited on p. 33).
15. Chung, Y. and N. Dagli, "An assessment of finite difference beam propagation method", *IEEE Journal of Quantum Electronics*, vol. 26, no. 8, pp. 1335–1339, 1990. [Online] (cited on p. 33).
16. Huang, W., C. Xu, S. T. Chu, and S. K. Chaudhuri, "The finite-difference vector beam propagation method: Analysis and assessment", *Journal of Lightwave Technology*, vol. 10, no. 3, pp. 295–305, 1992. [Online] (cited on p. 33).

17. Ziogos, G. D. and E. E. Kriezis, "Modeling light propagation in liquid crystal devices with a 3-d full-vector finite-element beam propagation method", *Optical and Quantum Electronics*, vol. 40, no. 10, p. 733, 2008. [Online] (cited on p. 33).

18. Vanbrabant, P. J., J. Beeckman, K. Neyts, R. James, and F. A. Fernandez, "A finite element beam propagation method for simulation of liquid crystal devices", *Optics express*, vol. 17, no. 13, pp. 10 895–10 909, 2009 (cited on p. 33).

19. Wang, B., X. Wang, and P. J. Bos, "Finite-difference time-domain calculations of a liquid-crystal-based switchable bragg grating", *JOSA A*, vol. 21, no. 6, pp. 1066–1072, 2004 (cited on p. 34).

20. Hwang, D. K. and A. D. Rey, "Computational modeling of the propagation of light through liquid crystals containing twist disclinations based on the finite-difference time-domain method", *Appl. Opt.*, vol. 44, no. 21, pp. 4513–4522, 2005. [Online] (cited on p. 34).

21. Ilyina, V. and S. Subota, "Numerical study of liquid crystal-induced optical singularities", *Molecular Crystals and Liquid Crystals*, vol. 453, no. 1, pp. 275–291, 2006. [Online] (cited on p. 34).

22. Goodman, J. W., *Introduction to fourier optics*. Roberts and Company Publishers, 2005 (cited on p. 35).

23. Li, L., D. Bryant, T. V. Heugten, and P. J. Bos, "Near-diffraction-limited and low-haze electro-optical tunable liquid crystal lens with floating electrodes", *Opt. Express*, vol. 21, no. 7, pp. 8371–8381, 2013. [Online] (cited on p. 39).

24. Lee, C.-T., Y. Li, H.-Y. Lin, and S.-T. Wu, "Design of polarization-insensitive multi-electrode grin lens with a blue-phase liquid crystal", *Opt. Express*, vol. 19, no. 18, pp. 17 402–17 407, 2011. [Online] (cited on p. 39).

25. Li, Y. and S.-T. Wu, "Polarization independent adaptive microlens with a blue-phase liquid crystal", *Opt. Express*, vol. 19, no. 9, pp. 8045–8050, 2011. [Online] (cited on p. 39).

26. Apter, B., U. Efron, and E. Bahat-Treidel, "On the fringing-field effect in liquid-crystal beam-steering devices", *Applied optics*, vol. 43, no. 1, pp. 11–19, 2004 (cited on p. 39).

27. Bogaerts, W., P. Dumon, E. Lambert, M. Fiers, S. Pathak, *et al.*, "Ipkiss: A parametric design and simulation framework for silicon photonics", in *9th International Conference on Group IV Photonics (GFP-2012)*, IEEE, 2012, pp. 30–32 (cited on p. 39).

28. Lee, E. S., P. Vetter, T. Miyashita, T. Uchida, M. Kano, *et al.*, "Control of liquid crystal alignment using stamped-morphology method", *Japanese journal of applied physics*, vol. 32, no. 10A, p. L1436, 1993 (cited on p. 44).

29. Goodman, L. A., J. McGinn, C. H. Anderson, and F. Digeronimo, "Topography of obliquely evaporated silicon oxide films and its effect on liquid-crystal orientation", *IEEE Transactions on Electron Devices*, vol. 24, no. 7, pp. 795–804, 1977 (cited on p. 44).

30. Uchida, T., M. Ohgawara, and M. Wada, "Liquid crystal orientation on the surface of obliquely-evaporated silicon monoxide with homeotropic surface treatment", *Japanese Journal of Applied Physics*, vol. 19, no. 11, p. 2127, 1980 (cited on p. 44).

31. Stohr, J. and M. Samant, "Liquid crystal alignment by rubbed polymer surfaces: A microscopic bond orientation model", *Journal of electron spectroscopy and related phenomena*, vol. 98, pp. 189–207, 1999 (cited on p. 45).

32. Chigrinov, V. G., V. M. Kozenkov, and H.-S. Kwok, *Photoalignment of liquid crystalline materials: Physics and applications*. John Wiley & Sons, 2008, vol. 17 (cited on p. 45).

33. Xie, Y., W. Woestenborghs, J. Beeckman, K. Neyts, and K. Panajotov, "Vertical cavity surface emitting laser with photo-aligned liquid crystal overlay", in *24th International Liquid Crystal Conference, Abstracts*, Mainz, Germany, 2012 (cited on p. 45).

34. Chigrinov, V., A. Muravski, H. S. Kwok, H. Takada, H. Akiyama, *et al.*, "Anchoring properties of photoaligned azo-dye materials", *Phys. Rev. E*, vol. 68, p. 061 702, 6 2003. [Online] (cited on p. 46).

3

Hybrid liquid crystal beam-steering

In chapter 2, an example of a liquid crystal beam-steering device was given. By applying a voltage over a liquid crystal, the director reorients, which causes a change in the effective refractive index experienced by light travelling through that medium. This electrically induced change in the refractive index allows us to alter the angle at which that light wave exits the medium. The example in the previous chapter used a gradient in the electric potential over the planar liquid crystal to induce a gradient in the OPL.

In this chapter, a different liquid crystal beam-steering device is studied. It uses a hybrid configuration, in which a liquid crystal is sandwiched between a microstructured grating and a planar substrate. The microstructured grating is shown schematically in figure 3.1. It has a sawtooth profile and is also known as a blazed grating.

In this device, there is no need for a gradient in the electric potential along the electrodes, assuming they are perfect conductors, but a gradient in the OPL is achieved due to the shape of the grating and the difference

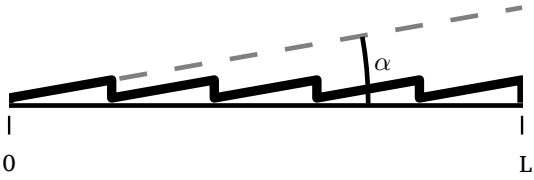

Fig. 3.1: A blazed grating is a periodic arrangement of prisms. Some of its properties can be understood using geometric optics applied to the subunits, but when the size of the subunits approaches that of the wavelength of light, the theory of wave optics is required to describe the functioning of the grating properly.

in refractive indices of the liquid crystal and the grating substrate. Two configurations of this device will be considered: in the first, it will be used in transmissive mode (section 3.1), in the second in reflective mode (section 3.2), which has a beneficial impact on the angular steering range. In each of the related sections some theoretical aspects are considered, which allow us to make fairly accurate predictions on their steering range. Simulation results are also provided for both configurations. In the last section of this chapter, experimental results on a reflective configuration are provided and compared to the theoretical and numerical analyses. A hybrid steering mode, where the device can be used to steer light to specific angles, or to have its reflections cancelled by means of total internal reflection (TIR) is also demonstrated.

3.1 Theory of the transmissive liquid crystal blazed grating

The study of the blazed grating beam-steerer is simplified when we first consider the structure of one periodically repeating unit of that grating, which is a prism.

3.1.1 Theoretical analysis

Consider the cross-section of the structure shown in figure 3.2. It shows a prism of which one interface is parallel to a planar substrate. When light is incident on this transmissive structure as shown in the diagram, it will exit, in general, at a different angle than the one at which it entered. The emergence angle, being the angle a light ray makes with the surface normal of a medium when it emerges from that medium, can be derived by applying Snell's law to the various interfaces and using the following two formulas, derived using simple trigonometry:

$$\text{In } \triangle ADB: \qquad (\pi/2 - \delta_1) + \alpha + \beta = \pi/2 \quad \Leftrightarrow \quad \delta_1 = \alpha + \beta \tag{3.1}$$

$$\text{In } \triangle BCE: \quad (\pi/2 - \gamma) + \delta_2 + (\pi/2 - \alpha) = \pi \quad \Leftrightarrow \quad \gamma = \delta_2 - \alpha \tag{3.2}$$

Application of Snell's law to the various interfaces now teaches us that the angle at which light exits, θ_o is given by:

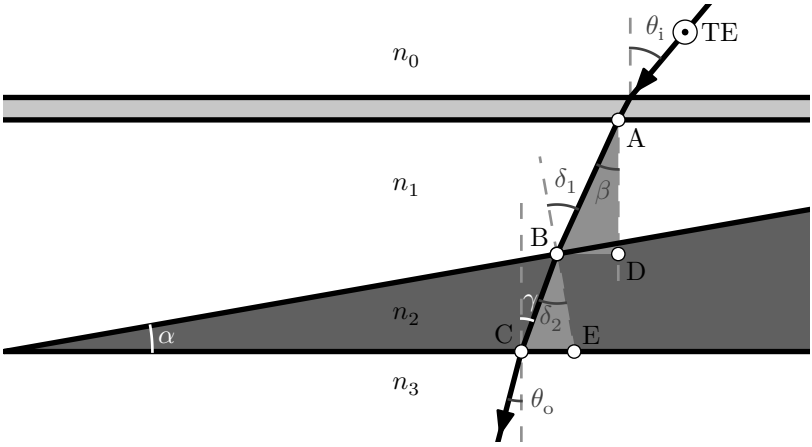

Fig. 3.2: Ray diagram showing the transmission of a beam of light through a structure with an inner wedge.

$$
\begin{aligned}
\theta_o &\overset{\text{Snell}}{=} \arcsin\left[\frac{n_2}{n_3}\sin\gamma\right] \\
&\overset{\text{BCE}}{=} \arcsin\left[\frac{n_2}{n_3}\sin\left(\delta_2-\alpha\right)\right] \\
&\overset{\text{Snell}}{=} \arcsin\left[\frac{n_2}{n_3}\sin\left(\arcsin\left\{\frac{n_1}{n_2}\sin\delta_1\right\}-\alpha\right)\right] \\
&\overset{\text{ADB}}{=} \arcsin\left[\frac{n_2}{n_3}\sin\left(\arcsin\left\{\frac{n_1}{n_2}\sin\left[\alpha+\beta\right]\right\}-\alpha\right)\right] \\
&\overset{\text{Snell}}{=} \arcsin\left[\frac{n_2}{n_3}\sin\left(\arcsin\left\{\frac{n_1}{n_2}\sin\left[\alpha+\arcsin\left(\frac{n_0}{n_1}\sin\theta_i\right)\right]\right\}-\alpha\right)\right]
\end{aligned}
\tag{3.3}
$$

Equation (3.3) indicates that a change of the emergence angle can be effected by varying any of the 6 parameters: θ_o is a function of the incidence angle θ_i, the slope or blaze angle α, the refractive indices of the outer media, n_0 and n_3 or the refractive indices of the inner media n_1 and n_2. If medium 1 or medium 2 would be a liquid crystal, the refractive index can be changed electrically, which would lead to a deviation in the emergence angle. If, for example, medium 1 is a liquid crystal, we may write:

$$
\Delta\theta_o^{\text{LC}\to\text{s}} = \theta_o(\theta_i,\alpha,n_0,n_e,n_s,n_3) - \theta_o(\theta_i,\alpha,n_0,n_o,n_s,n_3), \tag{3.4}
$$

where n_e and n_o are the extraordinary and ordinary refractive indices of the liquid crystal respectively and n_s the refractive index of the substrate, which in this example would then be medium 2. The superscript, LC $\rightarrow$ s, denotes that this is the deviation angle when light passes through the liquid crystal before it travels through the grating substrate.

Equation (3.3) can be simplified under the following assumptions: the angle of incidence is small, such that $\sin\theta_i \approx \theta_i \approx \arcsin\theta_i$; the outer media are the same and have a refractive index of equal to that of air, $n_0 = n_3 = 1$; the refractive indices of the inner media are similar, $n_1 \approx n_2$; the blaze angle α is small. Under those assumptions, equation (3.3) reduces to:

$$\theta_o \approx (n_1 - n_2)\alpha + \theta_i \tag{3.5}$$

This simplified equation shows that any change to θ_i would translate to the same change in θ_o. More interestingly, any change to the refractive indices of the enclosed media would be multiplied by the angle α:

$$\Delta\theta_o \approx \Delta n_i \times \alpha \tag{3.6}$$

Thus, in a structure where the blaze angle, α, would be 10°, a change of the refractive index by 0.2, a typical value for the birefringence of common liquid crystals, would result in a deviation of the emergence angle over $\Delta\theta_o \approx 2°$.

Equation (3.6) serves as a good first order approximation of the deviation angle one can expect from a beam that is transmitted through the device that is schematically represented in figure 3.2.

Note that in figure 3.2, the ray is assumed to be incident from the right of the upper substrate normal and θ_i is positive. The effect of using negative incidence angles, or –in other words–having the incident beam coming from the left of the upper substrate normal, on equation (3.3) is limited to sign changes in α, as explained in appendix A. After simplification of the deflection angle to a form similar to that of equation (3.6), we see that the absolute value of the beam deflection, $|\Delta\theta_o|$, is the same in both situations (beam incident from the right of the upper substrate normal or from the left) and we will therefor use positive angles of incidence whenever we numerically evaluate equation (3.6) or its predecessors.

We now perform a study using equation (3.3) to derive a set of guidelines to maximize the deviation angle, $\Delta\theta_o$, when one of the two inner media is a

liquid crystal that is switched.

A. *Propagation direction*

An import decision should be made at the start of the design of this device: whether the transmitted light beam should first propagate through the liquid crystal medium and then through the solid material or vice versa. If we assume that medium 1 is a liquid crystal and medium 2 an isotropic dielectric, this design decision means that light propagates either from top to bottom in figure 3.2 or from the bottom to the top.

Equation (3.6) hints that the direction in which light propagates will not influence the overall deviation angle. Numerically evaluating $\Delta\theta_o$ for the two scenarios using equation (3.4) and equation (3.3), and assuming the refractive index of the outer media is 1, leads to figures 3.3 and 3.4. These figures illustrate the achievable deviation angle evaluated on a limited subset of the 5-dimensional domain of that function. Each figure is subdivided in 3 columns: in the first one from the left, equation (3.4) is evaluated, meaning light travels through the liquid crystal before it is refracted at the LC–grating interface. In the second column, the deviation angle is evaluated in the alternative scenario where light travels through the grating first before it passes the LC ($\Delta\theta_o^{s\to LC}$). The third column shows the difference between both deviation angles in absolute values: $|\Delta\theta_o^{LC\to s}| - |\Delta\theta_o^{s\to LC}|$. If the value is positive, the first scenario is more advantageous to achieve larger deviation angles. Positive values are shown in red, negative values in blue.

Each row in figures 3.3 and 3.4 is the evaluation of those three functions using the refractive indices shown at the top of that row. Note that the limited subset of parameter choices shown in figures 3.3 and 3.4 is realistic for solid materials that are transparent, such as optical plastics which usually have refractive indices in the range from 1.4 to 1.6 in the visible wavelength spectrum [1, 2].

Notice that while the color schemes used in the two columns to the left are the same, the values are negated. The sign of the deviation angle refers to the direction in which the light beam will deflect when the effective refractive index of the LC changes from n_e to n_o: a negative value indicates a clockwise change in figure 3.2, a positive value is a counter-clockwise change.

The last columns teach us that the obtainable deviation angles in both

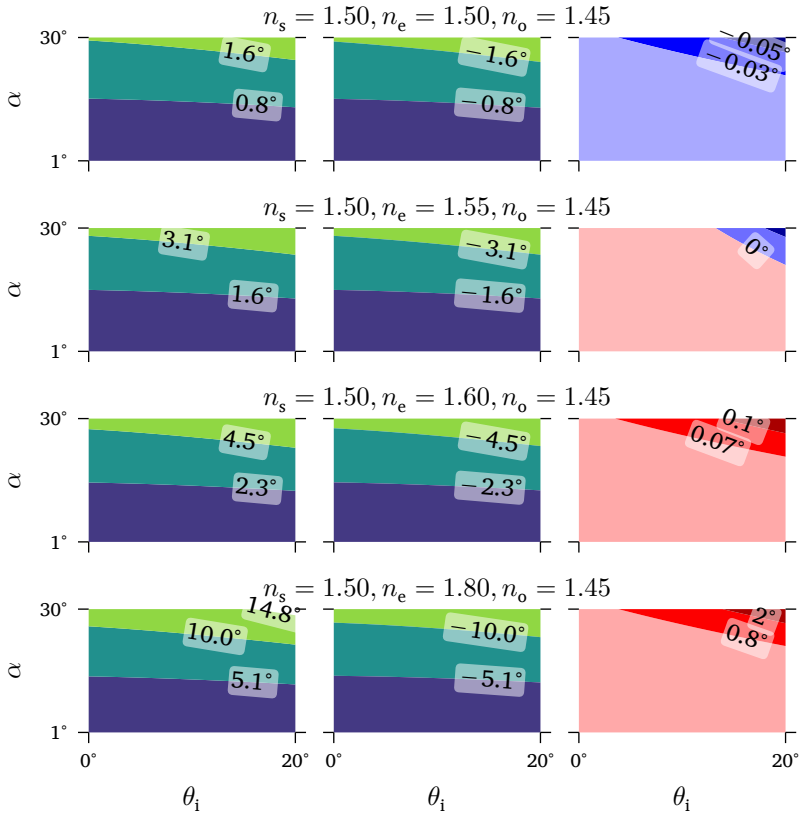

Fig. 3.3: Comparison of the achievable deflection angle between the situation where light travels from the LC to the grating substrate (left column: $\Delta\theta_o^{LC\to s}$) and vice versa (middle column: $\Delta\theta_o^{s\to LC}$). The column to the right shows $|\Delta\theta_o^{LC\to s}| - |\Delta\theta_o^{s\to LC}|$, with negative values indicated in blue, positive values in red.

scenarios are similar, especially at low values for α and θ_i, there is no clear indication to prefer one scenario over the other. This confirms the statement made at the beginning of the second paragraph in this subsection. There are also a few trends that can be seen in these graphs:

- As the birefringence of the liquid crystal increases, larger deviation angles are more often found when light travels from the liquid crystal to the blazed grating.

- The case where light travels from the LC to the grating substrate becomes more preferable for steering over larger angles, when the

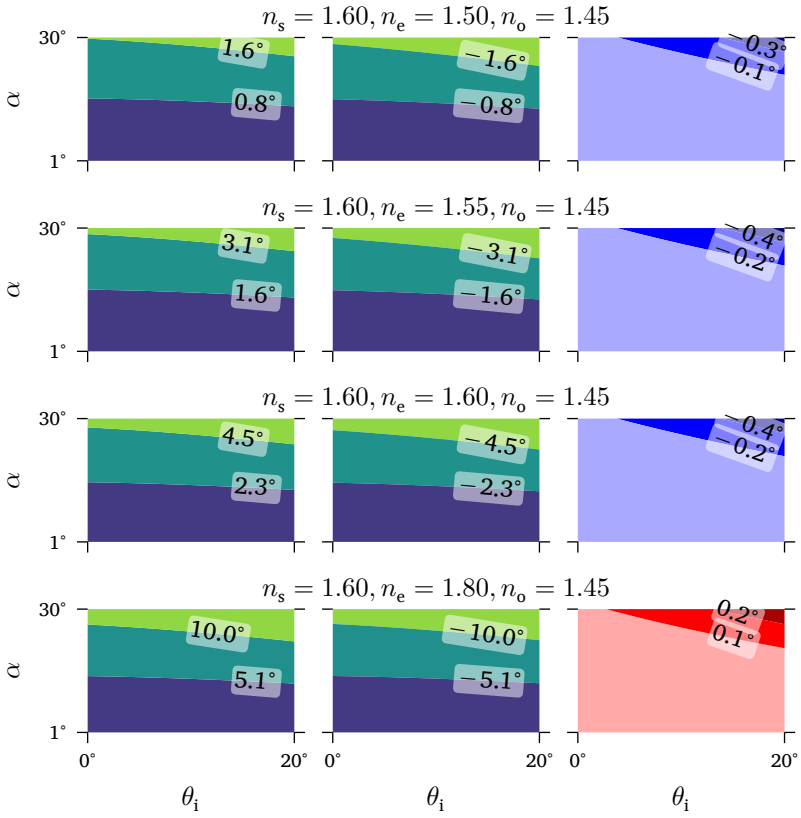

Fig. 3.4: Comparison of the achievable deflection angle between the situation where light travels from the LC to the grating substrate (left column: $\Delta\theta_o^{LC\to s}$) and vice versa (middle column: $\Delta\theta_o^{s\to LC}$). The column to the right shows $|\Delta\theta_o^{LC\to s}| - |\Delta\theta_o^{s\to LC}|$, with negative values indicated in blue, positive values in red. The difference with figure 3.3 is the refractive index of the grating substrate.

grating substrate has a smaller refractive index.

- The influence of the angle of incidence on the deviation angle is negligible, especially at low values for α and θ_i.

From this discussion, we conclude that there is no pronounced difference in the deviation angle between the two scenarios that were described earlier. When the refractive index of the grating substrate is rather small, the deviation angle tends to be slightly larger when light first propagates through the LC and then through the dielectric. Given that most optical plastics used in the LCP research group have a refractive index in the lower range, in the rest

of this chapter it is assumed that light first propagates through the liquid crystal, refracts at the boundary between the LC and the dielectric and then propagates through the dielectric.

B. *Influence of periodicity*

There is another reason to prefer the configuration where light travels through the LC layer before it travels through the grating substrate. As mentioned in section 1.3.1.A, liquid crystal layers are kept thin to reduce the switching speed. This means normal sized prisms are "wrapped" in a blazed grating configuration, which have the same beam-steering effect for monochromatic light where the optical path difference across the discontinuous jumps is a multiple of the wavelength. When we take into account the typical refractive indices of liquid crystals and optical plastics, often $n_\mathrm{e} > n_\mathrm{o} \approx n_\mathrm{s}$. Looking at the simple ray diagrams shown in figure 3.5, it is clear that shadowing may occur when the hybrid LC grating is illuminated from the bottom (the grating substrate) along the grating normal, which will reduce the efficiency. Light that hits the vertical slope will be deflected in a different direction than desired. This can be compensated by having light entering from the grating substrate side under a small angle.

The periodicity of the grating also introduces diffraction, which is unavoidable for coherent light. As mentioned in section 2.2.2.D, because of this, the direction in which light will propagate is quantized: there is a set of angles (orders) to which light can be diffracted and these orders are given by the grating equation equation (2.5). A good match between these angles and the angles predicted by the analysis using Snell's law ensures efficient steering.

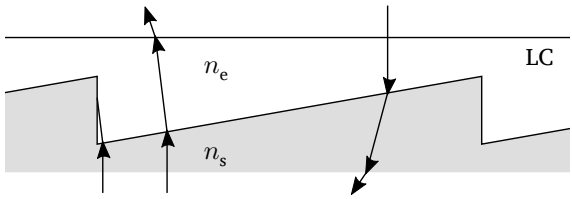

Fig. 3.5: Ray diagram illustrating the loss of efficiency due to shadowing: light travelling from the grating the higher refractive index LC could hit the steep grating reset as indicated in the left. When light travels the other way, this is not the case, as illustrated with the light beam to the right.

C. *Substrate sensitivity considerations*

Equation (3.6) also hints at the negligible sensitivity of the deviation angle due to changes in the refractive index of the substrate. This is not directly clear from figures 3.3 and 3.4, but by taking a different view into the 5-dimensional space, it is shown that this is the case. This is illustrated in figure 3.6, which shows the expected deviation angle as a function of the refractive index of the substrate and the difference in refractive indices of the liquid crystal (the birefringence) for 3 scenarios.

This degree of freedom in the choice of the dielectric is a great feature, as it allows us to design a prism-like substrate in any material we want. The micromachining of polymers, which are inexpensive, can be done with greater ease than the micromachining of glass [3]. Furthermore, polymers lend themselves to easy replication by molding and embossing techniques, such as soft embossing, which decreases the price of devices manufactured in this way.

Figure 3.6 also illustrates that the simpler formula of equation (3.6) gives a good approximation of the achievable deflection angle, when the incidence angle and blaze angle are small.

D. *Polarization considerations*

Finally, before we take a look at the realistic beam deflection behavior of the transmissive device, we consider the effect of the liquid crystal birefringence

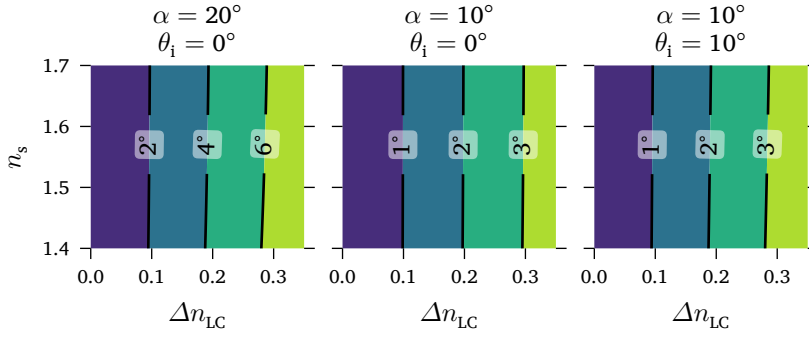

Fig. 3.6: The deviation angle as a function of the refractive index of the substrate and the difference in refractive indices of the liquid crystal, based on equation (3.4) and equation (3.3). n_o is assumed to be 1.5.

on the polarization of light.

In our simplistic model, thus far we have assumed that light passing through the liquid crystal layer experiences either the ordinary or the extraordinary refractive index of the liquid crystal. This assumption is valid for only one polarization direction and only if the LC director is uniform over the entire grating. We will see in the next section that the LC does not switch uniformly however and study the influence of that on the device's beam-steering efficiency in section 3.1.2.

Consider figure 3.7, which shows three possible director configurations for a nematic liquid crystal on a slanted interface. In the first, the director is perpendicular to both substrates, a configuration also known as homeotropic alignment at both substrates. In this configuration s-polarized light experiences the ordinary refractive index, while p-polarized light experiences an effective refractive index that lies between the ordinary and extraordinary refractive index and is given by [4]:

$$n_{\text{eff}}(\theta, n_{\text{e}}, n_{\text{o}}) = \left(\frac{\cos^2 \theta}{n_{\text{o}}^2} + \frac{\sin^2 \theta}{n_{\text{e}}^2} \right)^{-1/2} \tag{3.7}$$

where θ represents the angle between the propagation direction of light and the director. Because the interfaces are not parallel themselves, this director configuration is inhomogeneous and so the effective refractive index will depend on the position within the LC. In figure 3.7b, the director is viewed head-on, with its main axis perpendicular to the xy plane. In this configuration s-polarized light experiences the extraordinary refractive index of the liquid crystal, as the electrical component of light, $\vec{E}$, is parallel to the director. P-polarized light experiences the ordinary refractive index in that case. Finally, in figure 3.7c the director is parallel to the xy plane and is parallel to the upper and lower interfaces in their neighborhoods. This director configuration is also inhomogeneous; there is a non-negligible amount of splay energy in the bulk of this LC configuration. Here, s-polarized light experiences the ordinary refractive index of light, regardless of its position in the liquid crystal, while p-polarized light experiences an effective refractive index that is dependent on the position. Table 3.1 summarizes the refractive indices experienced by light of the two mutually orthogonal polarization modes.

We already know from the previous section that in order to maximize the deviation angle, $\Delta\theta_{\text{o}}$, the difference between the two refractive indices

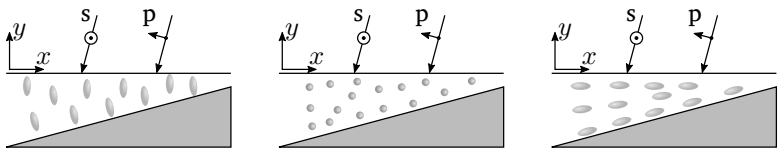

Fig. 3.7: The three possible director configurations under consideration in a simplistic LC switching model of the wedge-shaped device. The orthogonal s- and p-polarizations of an incident wave are indicated.

Table 3.1: The experienced refractive index for s- and p-polarized light in the three situations depicted in figure 3.7.

	Fig.3.7a	Fig.3.7b	Fig.3.7c
s	n_{o}	n_{e}	n_{o}
p	$n_{\mathrm{eff}}(y)$	n_{o}	$n_{\mathrm{eff}}(y)$

experienced by light in the liquid crystal should also be maximized. In practice the LC is switched between the situations shown in figure 3.7a and figure 3.7b or between figure 3.7a and figure 3.7c. Table 3.1 shows that the largest index difference between these scenarios is obtained when switching between figure 3.7a and figure 3.7b, using s-polarized light.

Note that in this discussion, there has been no mention of the sign of the dielectric anisotropy, $\Delta\varepsilon$, of the liquid crystal: it could be positive or negative. The only effect this property would have is that it would define which of the figures represents the state of the LC when no voltages are applied (the "off-state").

3.1.2 Numerical analysis of the transmissive grating

In the previous paragraphs the working principle of a one-dimensional hybrid liquid crystal beam-steering device was explained. To derive the simple expression of equation (3.6) the assumption that the liquid crystal is uniform in the presence of an applied voltage and without it, was silently made. This is not the case in reality and it was already hinted at near the end of the previous section: figures 3.7a and 3.7c show a director field that is not uniform. The quasi-static electric field originating from applied voltage signals plays an important role in the director configuration. Intuitively we feel that in a sawtooth-like cavity, the electric field is in general not uniform. As the director

tends to align with the electric field*, the director field will also be nonuniform. The liquid crystal director configuration in the beam-steering device we have studied thus far can be simulated numerically. The director field will depend on the geometry of the device, the placement of the electrodes, the applied potential and the materials used.

In this section, the director field is numerically simulated for a few scenarios, using the FEM software discussed in section 2.2.1.B.

A. *Used geometry and materials*

The simulated device geometry is shown in figure 3.8. To be able to compare the experimental results discussed in section 3.4 to the simulations, the parameters of the simulated geometry, shown in the figure, are chosen in such a way that they resemble best the devices that were fabricated and tested. This will not limit all the conclusions of this chapter to just this specific geometry though, as some findings are applicable to similar geometries with a set of different parameters.

In the software, the alignment layers are configured to impose a preferential direction to the LC director along the z-axis, with a 2° pretilt on both the LC–superstrate interface, as well as the LC–grating interface, to achieve anti-parallel alignment. The anchoring is assumed to be strong: the polar and azimuthal anchoring energy are set at $1 \times 10^{-3}\,\mathrm{J\,m^{-2}}$.

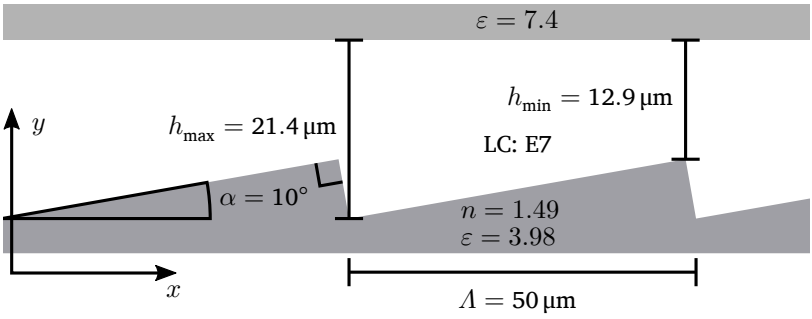

Fig. 3.8: Schematic of the simulated geometry and the material constants of interest. Material parameters of the used LC are given in tables 2.1 and 2.2. Note that due to the periodicity of the grating, only one period needs to be simulated.

*For liquid crystals with positive dielectric anisotropy. With negative dielectric anisotropy the director tends to be perpendicular to the electric field.

B. *Electrical simulation results*

The position of the electrodes has not been mentioned thus far. They are typically placed in close proximity to the LC to reduce the voltages needed to switch the material. That leaves two options. For the upper substrate (the "superstrate"), the electrode is simply placed directly on the interface between the liquid crystal layer and the superstrate. For the electrode on the side of the grating there are two choices: either the electrode is deposited on top of the grating, following the grating interface or it is deposited underneath the grating. The former has the advantage that any applied electric potential difference is entirely over the liquid crystal, while in the latter the dielectric grating substrate acts as a capacitor in series with the liquid crystal and will thus screen a part of the applied electric potential. Because the permittivity of the grating is smaller than that of the liquid crystal and the thickness of the grating substrate could potentially be much thicker than the liquid crystal layer, the electric potential drop over the grating could be quite high. The shielding effect of the grating is simulated in this work with the FEM software that caculates the director orientation (ref. section 2.2.1.B), which also solves the Poisson equation for the electric field.

The configuration where the electrode is underneath the grating has a distinct fabrication advantage: substrates with a transparent conductive coating can simply be bought. Depositing a transparent conductive coating on top of a structured surface is not straightforward and care has to be given to the deposition parameters such as deposition angle and possible heating of the substrate. The influence of the electrode position on the director profile and thus the deviation angle will be discussed in this section and section 3.1.2.C.

The results of four simulations at different potentials for the two different configurations are visualized in figures 3.9 and 3.10. These figures show the director profile within the liquid crystal cavity, together with the equipotential lines over the entire unit cell. Only one period of the grating is simulated, as periodic boundary conditions on the left and right sides are applied. Dirichlet boundary conditions apply to the electrodes. Note that the grating substrate extends 2.5 µm below the lowest point of the grating. For the electrical simulation, the thickness of the grating is irrelevant in case the electrode is on top of the grating as both electrodes extend over the entire substrate. For that reason the thickness of the grating is not indicated in figures 3.9a and 3.9b.

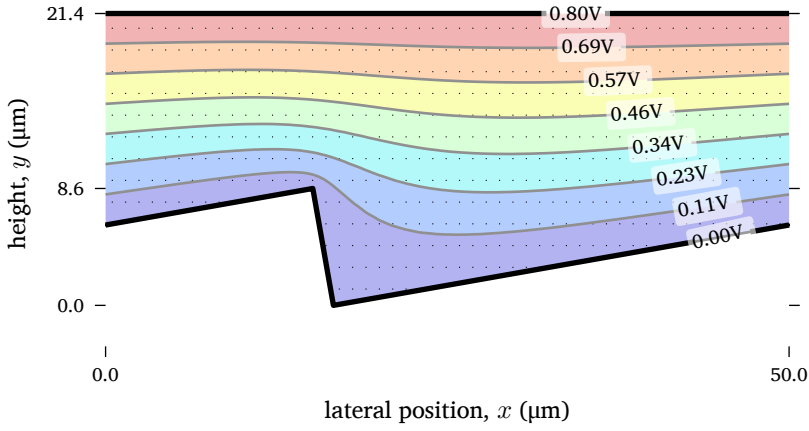

(a)

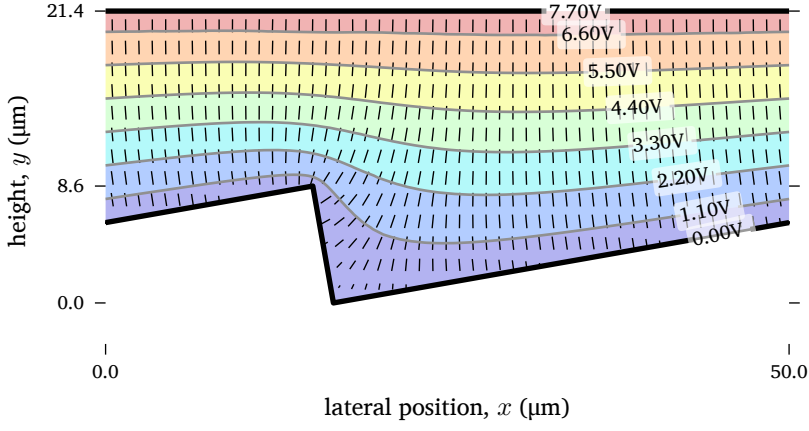

(b)

Fig. 3.9: Simulated director profile and equipotential lines in a hybrid geometry where one electrode covers the upper, planar substrate and another electrode is coated over the grooves of the grating. In (a), the voltage between the electrodes is $V = 0.8\,\mathrm{V}$, while in (b) $V = 7.7\,\mathrm{V}$. The structure is periodic along the x-direction. The black dots and rods represent the projection of the liquid crystal director on the xy-plane. The thick, black lines represent the electrode covered interfaces.

It is clear from figures 3.9a and 3.9b that the non-planar profile of the

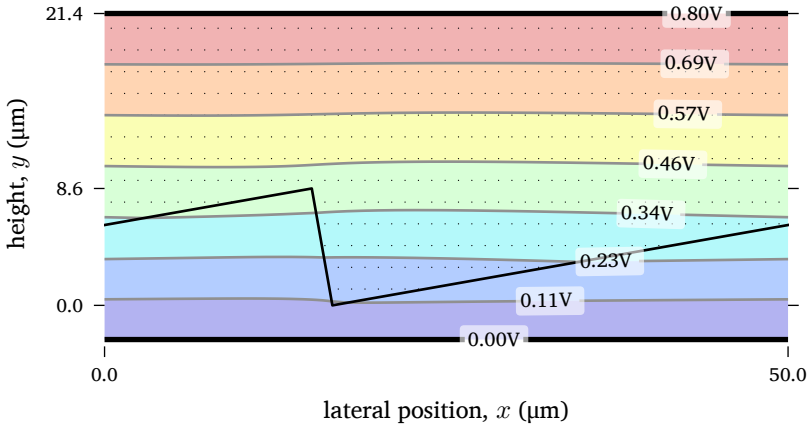

(a)

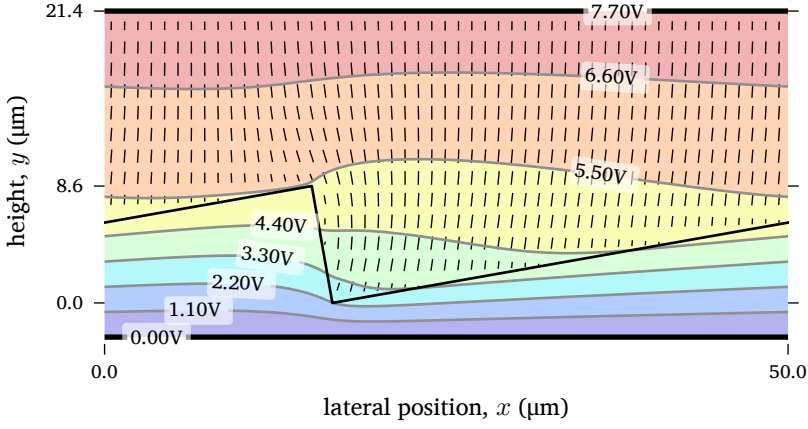

(b)

Fig. 3.10: Simulated director profile and equipotential lines in a hybrid geometry where one electrode covers the upper, planar substrate and another electrode is *below* the grooves of the grating. The same notations as in figure 3.9 apply. The thinner black line shows the outline of the grating that is not covered by an electrode.

grating causes a laterally varying electric field that is strongest at the peak of the grating. The x-component of the electric field is non-negligible in the neighborhood of the steep sidewall and this gives the director a strong

x-component there, rather than merely tilting the director, which is the case for the majority of the cell. When the electrode is below the grating (figures 3.10a and 3.10b) and a voltage is applied that is insufficient for reorienting the liquid crystal, the equipotential lines are nearly parallel and the influence of the grating structure on the electric field distribution is negligible. The reason for this is simple: in this configuration, the permittivities of both the grating and the liquid crystal are similar, $\varepsilon_s \approx \varepsilon_\perp$. To the electric field, it is as if the entire cell, grating plus liquid crystal, is filled with a nearly homogeneous material, similar to a parallel-plate capacitor. Once the electric potential difference is sufficiently high and the director starts to reorient, the isopotential lines change rapidly and the potential drop over the liquid crystal becomes smaller relative to the drop over the dielectric. The reason for this is that $\varepsilon_\parallel$ is approximately five times that of the substrate.

At low voltages, the initial alignment of the director is along the grating grooves, i.e. perpendicular to the xy plane of these figures. By comparing the two configurations at higher voltages, we notice that in both scenarios the director is nearly perfectly tilted, except in the neighborhood of the steep grating edge. There, the director exhibits noticeable twist, which is more pronounced when the electrode is on top of the grating (figure 3.9b). From this observation, it may be expected that light passing through this region will undergo some degree of polarization rotation.

C. *Optical simulation results*

To verify the device's beam-steering functionality, the power in the transmitted diffraction orders at 633 nm is recorded, relative to the power of the incoming source. The orders are determined by the periodicity of the grating and the wavelength, according to the grating equation, which is given in equation (2.5). In the simulation, s-polarized light is perpendicularly incident on the structure ($\theta_i = 0$), so the electric field component is along the grooves and hence along the director when no potential is applied. The boundary conditions in the optical simulations are Bloch-periodic at the sides and a perfectly matched layer at the top and bottom.

Figures 3.11 and 3.12 show the results of the optical simulations for the two scenarios, with the electrode above and below the grating respectively. Figures 3.11a and 3.12a nicely illustrate the beam shifting behaviour: as the

voltage over the liquid crystal increases, the majority of the beam power moves from one order to the next. This is also shown in figures 3.11b and 3.12b which are alternative presentations of the same data that allow for easier reading of the actual power levels. At low voltages the power is distributed nearly equally in the 4th and 3rd order for both electrode configurations. The analytical equation derived in section 3.1 predicts that when the experienced refractive index is n_e, a perpendicularly incident lightbeam would emerge at an angle of 2.4°, which is between both the angles computed in the simulation that correspond to the 4th and 3rd order.

When the electrode is above the grating, the total beam deflection, $\Delta\theta_o$, is about 2.2° and the power in the 1st order reaches its maximum at 4.0 V. While the power in the zeroth order keeps increasing as the voltage increases, it never reaches a value comparable to the maximum of the other orders. The power increase for the zeroth order also occurs much slower than the power changes that occur for the other orders in the range of 0.0 V–4.0 V. This indicates that the bulk of the liquid crystal is fully switched after about 4 V–5 V. The small changes that occur for larger voltages are likely due to reorientation of the liquid crystal near the substrate, which is governed by the interplay of anchoring effects and applied electric field.

The sequence of diffraction orders that carry the majority of power is more complex when the electrode is below the grating. Figure 3.12a shows that the beam initially moves from the 4th order to the 0th order and goes further until it reaches the 1st order on the other side of the grating normal (order -1). This corresponds to a change of about 3.6° over 4 V. The beam then gets directed back to the 0th order, which becomes dominant around 6 V and reaches a maximum of 71 % at 9.1 V.

Figures 3.11 and 3.12 show the combined intensity of both s- and p-polarized light in the different diffraction orders. It is instructive to separate both polarizations to see how much of the incident light, which is s-polarized, is converted to p-polarized light. Figure 3.13 shows the normalized intensity of that part of figure 3.11a which is p-polarized. As the colorbar indicates, only about 6 % of the light present in the results of figure 3.11a is p-polarized. Conversion to p-polarized light (polarization leakage) becomes pronounced around 5 V. Figure 3.14 shows the p-polarized transmitted diffraction orders when the electrode is below the grating. Like the previous scenario, where the electrode is above the grating, very little light is converted. The conversion

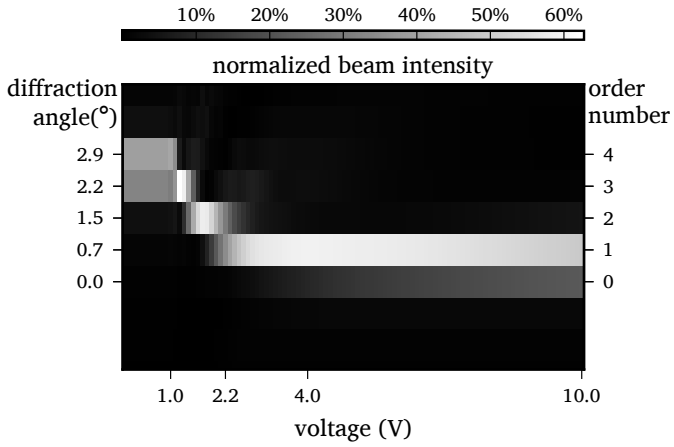

(a)

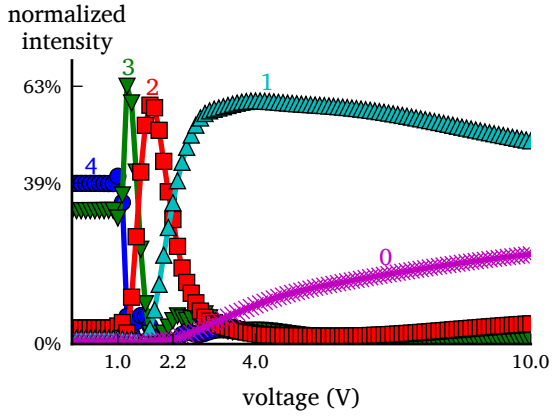

(b)

Fig. 3.11: Simulated power in several transmitted diffraction orders for the hybrid grating where the bottom electrode is *on top* of the grating and $\lambda = 633\,\text{nm}$. In (a) the beam jumping behaviour is illustrated, whereas (b) shows power details more clearly.

starts at higher voltages, compared to figure 3.13, which is logical, because the voltage over the liquid crystal is reduced by the grating in this case, so that higher voltages are needed to induce a similar change in the LC director.

Note that in figures 3.11 to 3.14, the power is normalized with respect to the power of the incoming light. A part of the incident light will be reflected as light travels from air (the surrounding medium) to the device. Figure 3.15

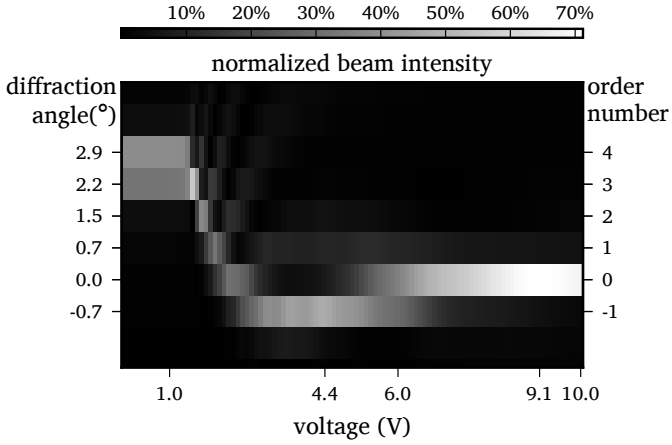

(a)

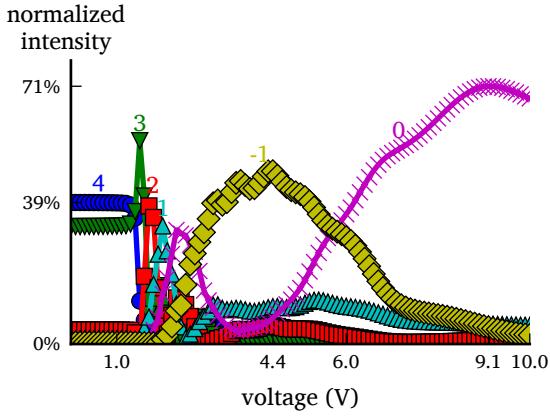

(b)

Fig. 3.12: Simulated power in several transmitted diffraction orders of the hybrid grating where the bottom electrode is *below* the grating and $\lambda = 633\,\text{nm}$. In (a) the beam jumping behaviour is illustrated, whereas (b) shows power details more clearly.

shows that about 88 % is transmitted and that about 78 % ends up in the orders -1 to 4.

D. *Partial summary*

In this section, two configurations of the hybrid grating have been compared. They differed in the location of the electrodes. Simulations show that by

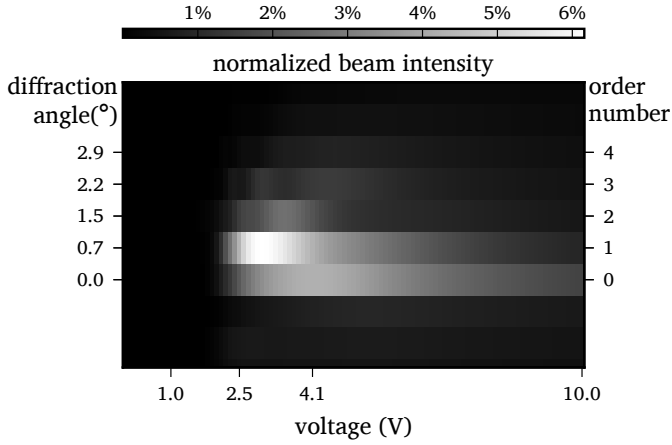

Fig. 3.13: The part of figure 3.11a that is p-polarized. Note the different colorscale between both figures.

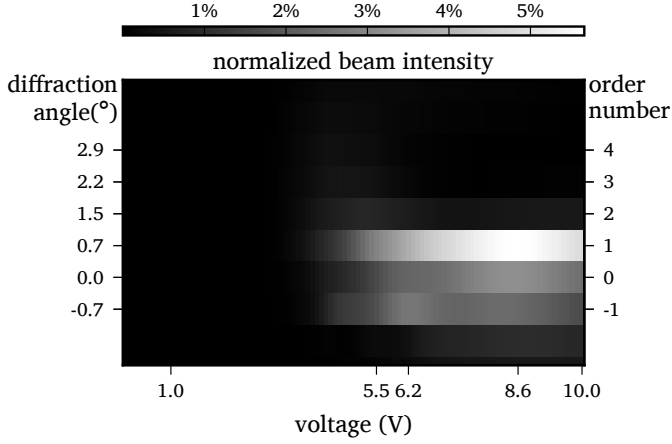

Fig. 3.14: The part of figure 3.12a that is p-polarized. Note the different colorscale between both figures.

placing the electrode 2.5 µm below the grating the tunable deflection range can be increased from 2.2° to 3.6°, compared to the situation where the bottom electrode is on top of the grating. In both cases, the required voltage over the *entire* cell is only 4 V. The normalized maximal power in each order is about 40 % when the electrode is below the grating, compared to about 60 % when the electrode is on top of the grating. Little polarization conversion occurs in both configurations. Both configurations have their advantages and the

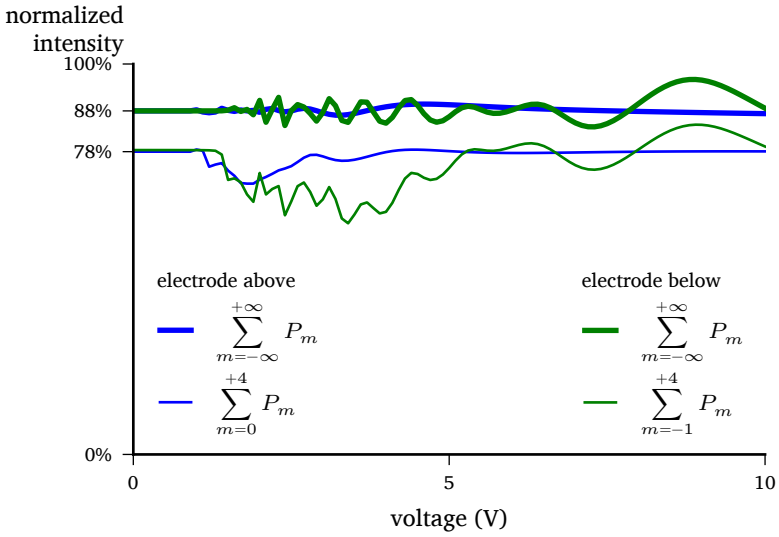

Fig. 3.15: The power, P, in the diffraction orders $m = -1$ to $m = 4$ compared to the total power transmitted through the structure for 633 nm light.

application requirements should dictate which of these is to be used.

3.2 Theory of the reflective liquid crystal blazed grating

One way to increase the deflection range from the hybrid grating is to use the device in reflective mode. In the following sections, the reflective hybrid grating is analyzed in a similar way as was done for the transmissive hybrid grating.

3.2.1 Theoretical analysis

Similar to section 3.1, the equation that determines the emergence angle can be derived based on geometric optics. Figure 3.16 shows the ray diagram for a ray that reflects on the slanted interface of the hybrid grating. The emergence angle is given as:

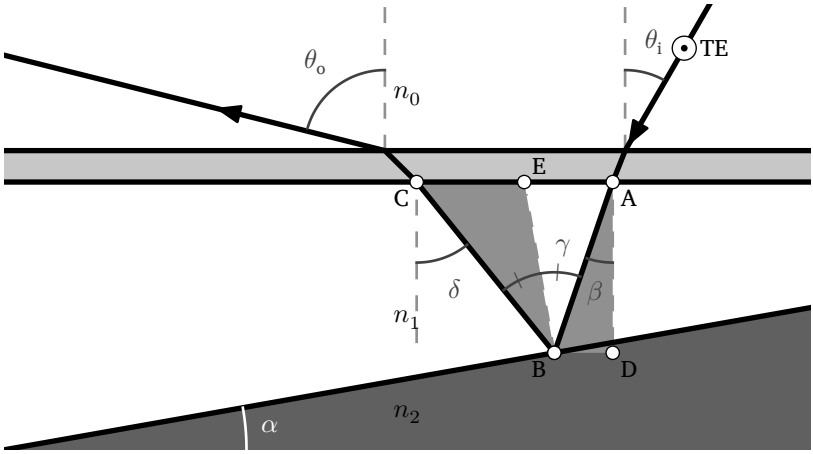

Fig. 3.16: Ray diagram showing the reflection of a lightwave through a structure with an inner wedge. The angles drawn are representative for realistic combinations of n_0 and n_1, with $n_1 > n_0$.

$$\begin{aligned}
\theta_o &\overset{\text{Snell}}{=} \arcsin\left\{\frac{n_1}{n_0}\sin\delta\right\} \\
&\overset{\text{BCE}}{=} \arcsin\left\{\frac{n_1}{n_0}\sin\left[\alpha+\gamma\right]\right\} \\
&\overset{\text{ADB}}{=} \arcsin\left\{\frac{n_1}{n_0}\sin\left[2\alpha+\beta\right]\right\} \\
&\overset{\text{Snell}}{=} \arcsin\left\{\frac{n_1}{n_0}\sin\left[2\alpha+\arcsin\left(\frac{n_0}{n_1}\sin\theta_i\right)\right]\right\}
\end{aligned} \tag{3.8}$$

In a similar way as before, equation (3.8) can be simplified by assuming that the angle of incidence, θ_i, and the blaze angle, α, are small and that the refractive index of the outer environment, n_0, is equal to that of air. We may write then for the deviation angle, $\Delta\theta_o = \theta_o(\alpha, \theta_i, n_e) - \theta_o(\alpha, \theta_i, n_o)$, that

$$\Delta\theta_o \approx 2 \times \Delta n_{LC} \times \alpha \tag{3.9}$$

in which Δn_{LC} is the birefringence of the liquid crystal, the difference between the refractive index for the extraordinary and the ordinary ray, $\Delta n_{LC} = n_e - n_o$.

Similar to equation (3.6), this equation shows that the blaze angle acts as a multiplicative factor to the birefringence of the liquid crystal. Because of the reflection, there is now also a doubling of the deviation angle. In the

transmissive grating, the refractive index of the substrate was negligible. It had to be optically transparent though. In the reflective configuration, there is no influence of the substrate at all. It does not even have to be transparent. This allows even more freedom for the designer.

Naively, one might want to increase the angle α to obtain a larger deviation angle. Unlike the transmissive grating, there is a limit to this: as figure 3.16 shows, the angle at which the beam exits is larger than the incidence angle. By increasing α, the upwards travelling beam will eventually hit the top substrate interface at the critical angle, δ_c, at which TIR occurs. For the refractive indices of the liquid crystal E7 at 633 nm, this already happens at $\alpha_c = 17.7°$ (n_e experienced) and $\alpha_c = 20.6°$ (n_o experienced). By using a blaze angle of 17.6°, the deflection angle could become as large as 24.6°, based merely on equation (3.8) and the refractive indices of E7 mentioned earlier. However, the magnitude of the partial reflections from the inner medium to the environment would be close to 100 % as predicted by the Fresnel coefficients [5], so while this scenario would be more ideal for obtaining a larger deflection angle, it will reduce the amount of power reflected from the device. A blaze angle of 10° ensures that we remain below the critical angle for total internal reflection, while preserving a moderate amount of power in the reflected orders. It would lead theoretically to a deviation angle of 5.0°, assuming the refractive index of the liquid crystal is uniform and equal to either E7's n_e or n_o. The TIR condition can still be reached by increasing the angle of incidence, which will be discussed in section 3.4.3.

3.2.2 Numerical analysis of the reflective grating

For the electrical simulations in which the director profile is computed, the simulation results for the transmissive grating apply to the reflective grating as well. Figure 3.9 would still describe the director profile when light would be reflected from the grating.

For the optical simulations a few changes need to be made: the material that the grating is made of should be replaced by a proper reflector or covered with a thin reflective layer. Such a material can be found in Lumerical's material database: "Ag (Silver) - CRC". The choice for silver is inspired by the physical realisation of a reflective grating that happened concurrently and which required a few processing iterations to find a deposition method

that would work on the grating. Furthermore, the position of the far-field calculating component needs to be changed from below the grating to above the device to measure the reflected waves. In these optical simulations, as well as with those for the transmissive grating, light is assumed to enter the liquid crystal directly from air, there is no upper substrate present. This is not a physically realistic simulation, because an alignment layer is still present at the LC–air interface. A planar substrate there would not change the phase of the monochromatic wave as it emerges from the cell, so it is allowed to ignore it for simulating the angles to which light diffracts, as those depend on the phase. An upper substrate would affect the power radiated in the various orders though, so some caution is advised when discussing powers.

Figures 3.17a and 3.17b show how a plane wave propagates through the structure, at two different times, when the two electrodes are at the same electric potential. In figure 3.17a, the plane wave has just reached the reflective interface and the reflected wave is interfering with the incident wave. Three regions can be distinguished and are labelled in the figure: in the region labelled A, the wave fronts of the specularly reflected wave interfere with the wavefronts that are propagating towards the grating. In the region labelled B, the plane wave that is transmitted propagates through the liquid crystal medium towards the slanted interface, whereas in the C-region that downwards propagating wave interferes with the wave that is specularly reflected from the upper interface.

Figure 3.17b shows the situation at a later time, after continuous wave (CW) regime has set in and the source of the plane wave is subsequently abruptly stopped[*]. Four regions can be distinguished: in D, the reflected wave is propagating through the surrounding air medium. In E, the reflected wave is still within the LC medium. It is clear from the angle the wavefronts make that the direction the wave travels in within the LC medium is different from the direction it travels in when it is in air. That difference corresponds to the difference between the angles δ and θ_o in figure 3.16. In the region marked by the letter F, the incident wave and the reflected wave interfere, similar to region C in figure 3.17a. Finally, in region G another interference effect is visible. Its origin can be found in the different optical path lengths that rays falling to the left and right of the steep slope of the grating experience.

[*]This is not a physical possibility, but allows a clearer view of certain aspects of the wave propagation.

Had the optical path length difference been a multiple of the wavelength, this interference pattern would not have been visible. Note that in both images only the s-polarized waves are being shown.

By recording the diffraction pattern of the reflected wave at different voltages, a good image of the beam deflection behavior is formed, similar as was done for the transmissive grating. The result of these simulations is shown in figure 3.18. Figure 3.18a shows that by changing the voltage from

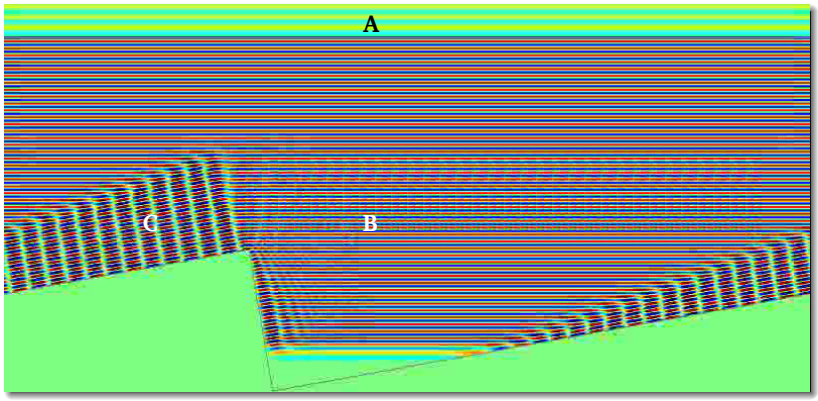

(a) The plane wave has just reached the reflector, but CW regime has not yet set in. A: specular reflection. B: transmitted wave propagating towards the grating. C: interference between the reflected and incident wave.

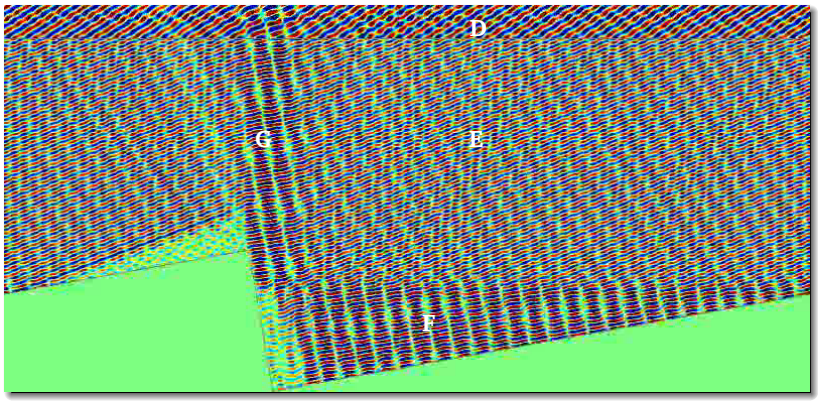

(b) The source is abruptly stopped and the last wavefronts propagate through the structure. D: reflected wave in the device's surrounding medium. E: reflected wave in the LC (no interference effects). F: interference of the reflected wave and the incident wave in the LC. G: interference due to optical path length mismatch.

Fig. 3.17: Snapshot of a steady-state plane wave ($\lambda = 633\,\text{nm}$) reflecting off a slanted interface. Only $\text{Re}(E_z)$ is shown.

0 V to 6.5 V the beam deflects roughly 5.3°, a value that is very close to the result obtained earlier from the analytical formula that was based merely on geometric optics.

As before, the amount of light that is converted from the incident s-polarized wave into p-polarized light is extracted from the simulations. It is shown in figure 3.19. The colorbar reveals that there is considerable

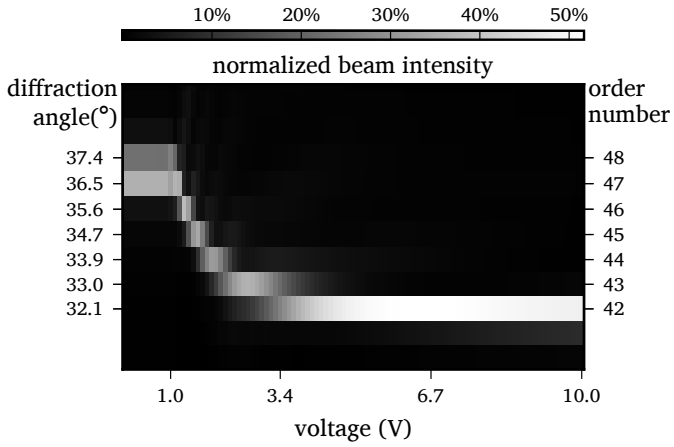

(a)

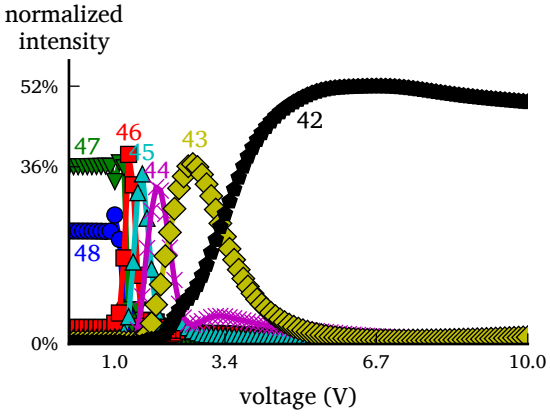

(b)

Fig. 3.18: Simulated power in several reflected diffraction orders of the hybrid grating where the bottom electrode is on top of the grating and $\lambda = 633\,\text{nm}$. In (a) the beam jumping behaviour is illustrated, whereas (b) shows power details more clearly.

polarization conversion this time. Comparison of figure 3.18a and figure 3.19 indicates that the power in the 43rd diffraction order is nearly all p-polarized.

The power in the orders 42 to 48 is about 64 % of the power of the incident wave, as figure 3.20 shows. About 7 % of the incident light is specularly reflected from the air–LC interface, which corresponds to the Fresnel reflection coefficient for normal incidence from air to a medium with refractive index n_e and is given by [5]:

$$R(\theta_i = 0) = \left| \frac{1 - n_e}{1 + n_e} \right|^2 \tag{3.10}$$

Only 88 % is captured in all the reflected orders. That means that about 12 % is lost due to absorption at the metallic interface and due to light that is trapped by total internal reflection. Indeed, a fraction of the reflected light that reaches the upper substrate is reflected back towards the grating. Upon each successive roundtrip, the angle δ from figure 3.16 increases. Eventually that angle will be larger than the critical angle at which point total internal reflection occurs.

3.3 Fabrication of a reflective hybrid grating

The reflective grating described in the previous section has also been fabricated and tested. In the theoretical description, variations of the blaze angle and

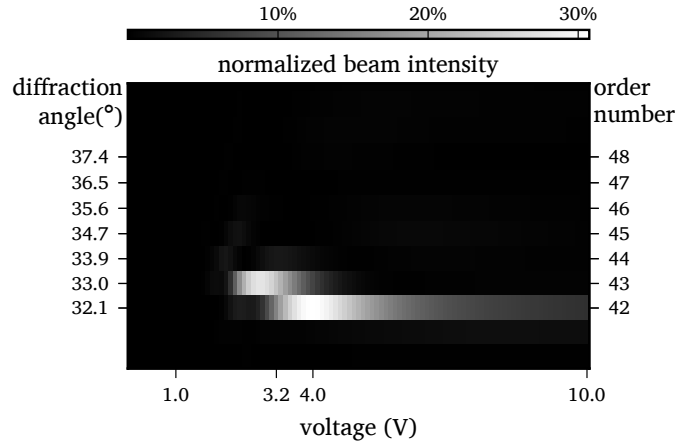

Fig. 3.19: The part of figure 3.18a that is p-polarized. Note the different colorscale between both figures.

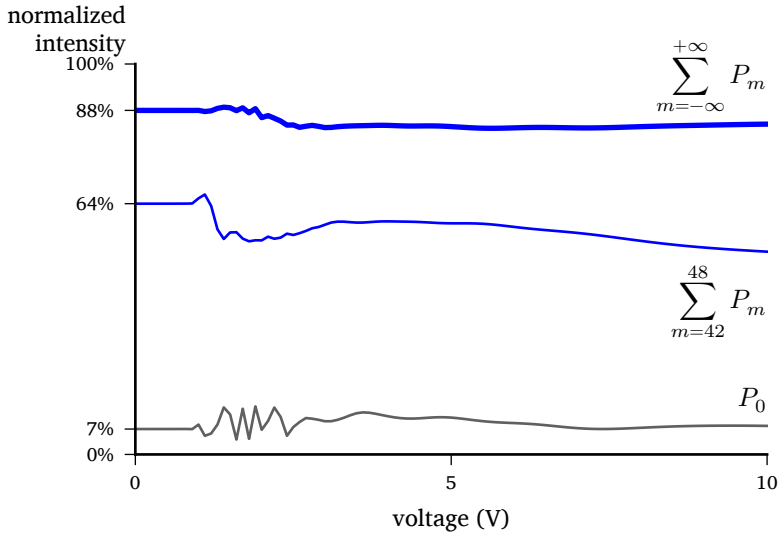

Fig. 3.20: The power, P, in the reflected diffraction orders $m = 42$ to $m = 48$ compared to the total reflected power for 633 nm light. Also shown is the specularly reflected light (light in the zeroth order).

thickness of the LC layer over multiple grating periods are assumed to be non-existent. These devices were manufactured in a non-industrial environment, which means that any variations will likely be larger than what an industrial type of processing could achieve. In this section, the fabrication process is detailed and measurements of the device's geometrical parameters are presented.

3.3.1 Grating description

The gratings were custom made by Michael Vervaeke of the B-Phot team of the Vrije Universiteit Brussel as part of his work for the SECONDOS* project. Several grating designs were initially proposed, while only some of those were fabricated and tested in various LC arrangements by Xiaobing Shang, Pankaj Joshi (both affiliated at the time with the CMST research group of Ghent University) and the author of this dissertation.

*The SECONDOS project is a Strategic Basic Research project, that was funded in large by the Belgian government agency for Innovation by Science and Technology (IWT). The project's full name is "Smart electro-optical components for the direction of solid-state light".

The blazed grating is made of poly(methyl methacrylate) (PMMA), an isotropic medium with a refractive index of $n_{\text{PMMA}} = 1.49$ at a wavelength of $\lambda = 633\,\text{nm}$ [6]. The dielectric constant of PMMA is between 3 and 9 [7, 8], the exact value depends on several parameters, like composition, polymerization path and degree of cross-linking. For the electrical simulations described in section 3.1.2.B, where one electrode is below the grating, $\varepsilon_r = 3.98$ is assumed, as this value corresponds to the permittivity of several optical photopolymers that were used for generating multiple inexpensive substrates from the more expensive PMMA grating by means of soft-embossing [9]. This choice allows re-using the simulation results for the inexpensive substrates.

The grating structure is obtained by hot-embossing, a technique allows for easy replication and upscaling possibilities [10]. A 0.5 mm thick sheet of PMMA, obtained from Notz Plastics AG, is hot-embossed with a brass mold that was manufactured using ultraprecision diamond milling with a cylindrical end-mill [11]. Because of the tool geometry, the two slopes of the grating make a right angle*, as illustrated in figure 3.8. The blaze angle is designed as 10° and the designed period is 50 µm. This is the same design as presented in section 3.1.2.A.

One of the parameters used in the simulations is the height difference between the peaks of the grating and the upper substrate. An accurate measurement of the lateral profile of these gratings is performed using a profilometer, before the liquid crystal cell is assembled. This measurement is shown in figure 3.21 for two different samples of the same grating design. The height profile near the edges is plotted. The graphs shows that there is a small variation in the vertical offset from the grating's side elevation, which is used to join the grating and the cover substrate during cell assembly. The graphs also indicate the periodicity, which is close to the design parameter of 50 µm. It should be noted that due to the finite width of the profilometer's stylus, the distance between the peaks and the valleys of the grating cannot be accurately measured. For that, the Wyko NT3300 non-contact profilometer from Veeco is used, which is a white-light interferometer system that is designed to profile structures by using interferometry instead of a stylus.

Figure 3.22 shows a measurement of this white-light interferometer. To the left is the unprocessed image that the built-in camera sensor images, to its

*These limitations have been reduced at a later stage in the research, so that sharper corners were possible. The study has continued with a right angle at the top of the grating.

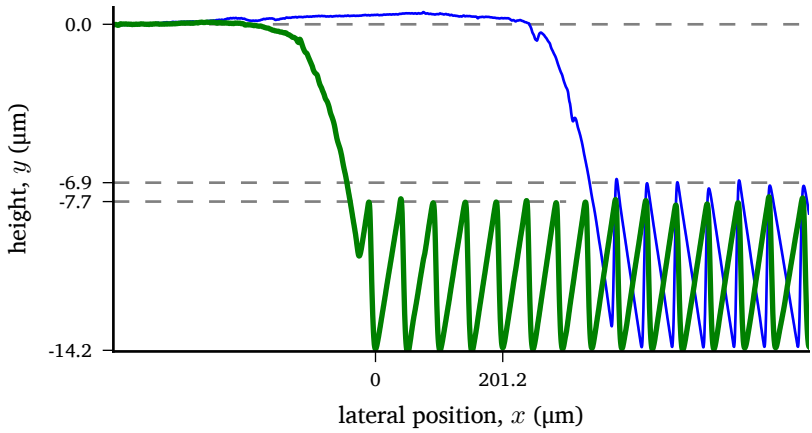

Fig. 3.21: Measurement of the cross-sectional profile of two samples of the same grating design using a Dektak 150 profilometer from Veeco.

right is the measured height profile of the same region. A slice along its y-axis is added to the right, which shows that the distance between the peaks and the valleys is approximately 8.2 µm. Xiaobing Shang has demonstrated that the variation of this distance is small ($\pm$0.1 µm) and that when this PMMA grating is used as the master mold for the soft-embossing process, the structure is well replicated [12]. Figure 3.22 also shows that the grating period is once again close to 50 µm. From these two dimensions a blaze angle of 9.3° is derived, slightly less than designed. The gradient in figure 3.22b indicates an overall smooth slope, although the unprocessed image illustrates that there are some local disturbances.

After the profiling measurements, a 15 nm thin layer of chromium is deposited on top of the grating using a physical vapor deposition (PVD) system. The chromium improves the adhesion of the actual reflective layer, which is a 50 nm layer of silver that is deposited subsequently. Both processes are carried out in the same system, under a vacuum pressure of 7×10^{-7} mbar, using a deposition speed of 0.5 Å s^{-1} for the Cr layer and 1 Å s^{-1} for the Ag layer.

3.3.2 Liquid crystal alignment

The next step in assembling the hybrid grating is to ensure a preferential alignment direction for the liquid crystal. As the grating is structured, the common technique of rubbing a cloth uniformly over the substrate (section 2.3.4.A) is

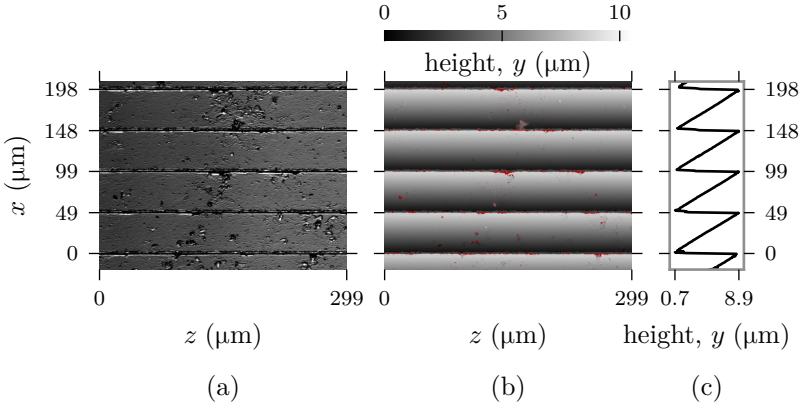

Fig. 3.22: Surface characterization of the blazed grating using a Wyko NT3300 profilometer from Veeco. (a) Unprocessed image. (b) Height profile. (c) Slice through the height profile. Red pixels in (b) indicate faulty data.

not advisable because there is a risk that the fibers of the cloth do not penetrate all the way into the valleys. This does not mean it is impossible, but there are easier methods to achieve alignment on structured substrates. For the grating substrates, photoalignment (section 2.3.4.B) is used. The transmission axis of the polarizer is aligned perpendicular to the grating grooves, to ensure the resulting preferential orientation of the director is parallel to the grooves, which results in a director profile shown in figure 3.7b.

3.3.3 Cell edge thickness

After the photoalignment step, a rectangular pattern, slightly larger than the grating area, is traced on an ITO-coated glass substrate using a syringe filled with glue. The glass substrate received the same photoalignment treatment as the grating. It will be used as the cover glass over the grating, creating a cavity between them. Mixed in the glue are spherical spacers of nominally 5.5 µm (Micropearl SP-2055 from Sekisui Chemical GmbH), which ensure a reproducible distance between the two substrates of the liquid crystal cell. It is at this point that the grating substrate is placed on top of the glass substrate. Pressure is applied uniformly to get good contact between both substrates and the glue as well as to keep the distance between the two substrates at about the size of the spacers. After curing the glue, the cell gets filled with the liquid crystal mixture E7. The glue outline does not form a closed loop, so

that liquid crystal can be injected into the cavity by placing a tiny amount of liquid crystal close to the opening of that outline. The droplet will spread in the cavity due to capillary forces. The cell is now fully assembled. Its cross-section is shown in figure 3.23. It is sometimes useful to add more glue to the edges to reduce the risk of failure if in the initial outline not enough glue was used. The cavity can also be fully sealed if that is desired. For the cell of which the measurement results are discussed in section 3.4, more glue was added to prevent the two substrates from detaching, which happened to a few other cells.

3.3.4 Alignment check

The effectiveness of the photoalignment can be evaluated after filling the cell with liquid crystal. Observation of the cell using polarized light microscopy (see section 2.3.5) gives the images shown in figures 3.24a and 3.24b. For these two images, the sample was tilted by approximately 18°, which is necessary to capture the reflected light with the 0.25 numerical aperture microscope objective. The tilt of the sample is evident from the defocusing

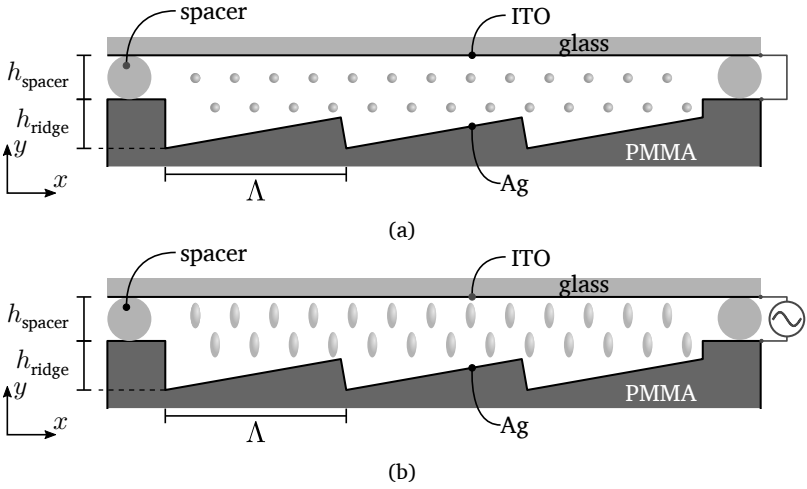

Fig. 3.23: Cross-section of the structure of the studied device. Only three grating periods are shown, but in reality there are about 100. The idealized working principle is illustrated: (a) in absence of an applied voltage, the director is aligned with the grating, along the z-axis—(b) when an electric potential is applied, the liquid crystal switches, thereby causing a change in the effective refractive index. $h_{\text{spacer}} = 5.5\,\mu\text{m}$, $h_{\text{ridge}} \approx 14.2\,\mu\text{m}$, $\Lambda = 50\,\mu\text{m}$.

in figure 3.24b: only the center part of the images is in focus. Most of the liquid crystal is homogeneously aligned, which is apparent from the overall dark appearance when the alignment direction of the liquid crystal is parallel to one of the polarizers (figure 3.24a). When the director is at 45° relative to the polarizer transmission axes, as in figure 3.24b, the image is uniformly bright, except for some smaller patches that vary in intensity compared to their surroundings. This non-uniform intensity can be explained using figure 3.24c, which shows the PMMA grating imaged from the backside (no liquid crystal), at the edge of the grating. Similar roughness is observed as in figure 3.22a, so these defects were present before the assembly. Figure 3.24d shows the same sample, observed using polarized light microscopy, with a larger magnification microscope objective, when light from red light emitting diodes (LEDs) is used and transmitted by the sample. The reflective coating is not thick enough to block all the light from the LEDs. About three sinusoidal variations in the intensity can be distinguished in each grating period. These fringes are the result of linearly increasing retardation [13]. It is believed that the fringes do not show up in figure 3.24b, because the fringes from different wavelengths in the microscope bulb's broadband spectrum overlap at different positions, which reduces the contrast of the fringes. The direction of the fringes, parallel to the grooves, also indicates good uniaxial alignment.

3.4 Experimental results of the reflective grating

In this last part, the beam-steering functionality of the device fabricated in section 3.3 is tested and compared to the theory. It is also shown how the device can be used not just to steer light, but also to guide light by means of total internal reflection.

3.4.1 Experimental setup

Figure 3.25 shows schematically how the experiment is conducted. The beam of a helium-neon (HeNe)-laser ($\lambda = 633\,\text{nm}$) is directed along the device's grating normal, which is parallel to the normal of the cover glass. Before incidence, the laser output is passed through a spatial filter to filter out its rapid spatial intensity fluctuations. The beam width is enlarged to cover more grating periods. It passes through a polarizer of which the transmission axis is

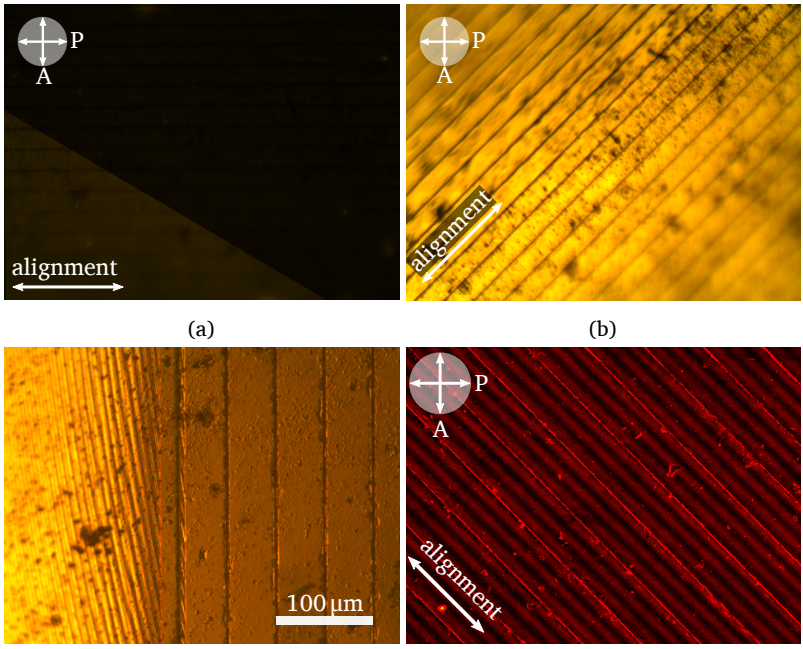

Fig. 3.24: Microscope images of the liquid crystal blazed grating hybrid cell, in absence of a voltage. The sample is imaged between two crossed polarizers in (a), (b) and (d). In (a), the sample is rotated such that the director is parallel to the analyzer. As this causes an overly dark image, the lower left region has been digitally enhanced to show the groove direction. In (b) and (d), the director is at 45° with respect to both polarizer transmission axes. In (c) the cell is imaged from the backside, with a magnification twice as large as in (a) and (b). The same magnification is used in (d), where the cell is observed in transmission, illuminated using red LEDs ($\lambda = 641\,\text{nm}$, $\Delta\lambda_{\text{FWHM}} = 18.7\,\text{nm}$).

parallel to the grooves of the grating, so that the electric field experiences the change from n_e to n_o as the voltage over the LC is increased. The diffracted beams hit a detection screen that is being imaged by a digital camera.

3.4.2 Diffraction patterns

Figure 3.26 shows two diffraction patterns recorded by the digital camera. The voltages applied over the LC at which these patterns are recorded are given in the figure. It is clear from these two images that the diffraction order that carries the majority of power has shifted from the 48th to the 43rd order. The images can be further annotated by including the emergence

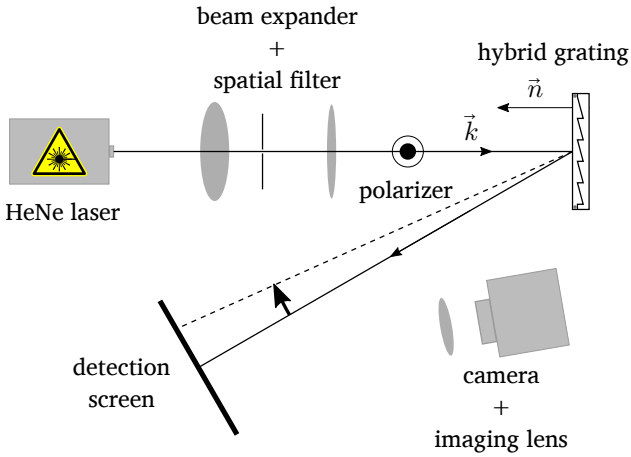

Fig. 3.25: Schematic illustration of the measurement setup in which the beam-deflection behaviour of a reflective grating is measured.

angles, which can be derived from the knowledge of the distance between the detection screen and the grating reflector and the conversion factor between pixels of the image and physical distances on the detection screen. The latter is obtained by using a calibration paper.

The diffraction pattern is recorded for a range of voltages between 0.1 V and 10.0 V using 0.1 V steps. This sequence of 2D images is subsequently processed by integrating the power in the different orders. In this way, the two-dimensional images are reduced to a one-dimensional dataset, which is shown in figure 3.27.

Comparison of figure 3.27 to the simulations from figure 3.18a shows good agreement in the tunable deflection angle, although the majority of the power at 0 V in figure 3.27 is in the 48th order, not the 47th as predicted by the simulations. Measurement of the power in the 48th order at 0 V shows 15.2 mW. Relative to the incident power of 86.1 mW, that is 17.7 %, not too

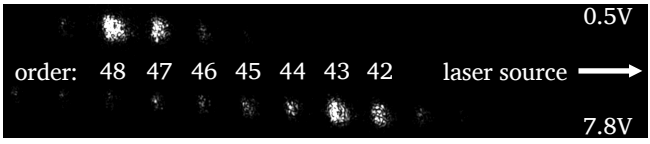

Fig. 3.26: Recorded laser diffraction pattern of the hybrid blazed grating at two different voltages. The location of the beam incident on the reflective grating, relative to the reflected beam, is indicated in the figure, as well as the order number, m, of each of the diffraction orders.

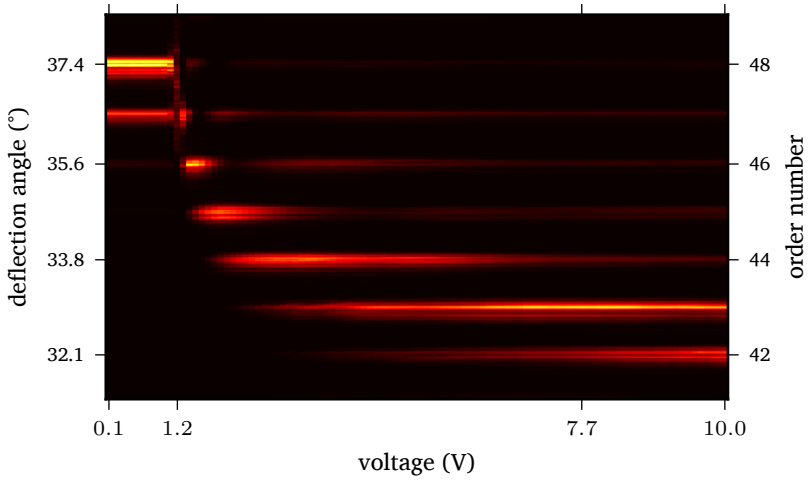

(a)

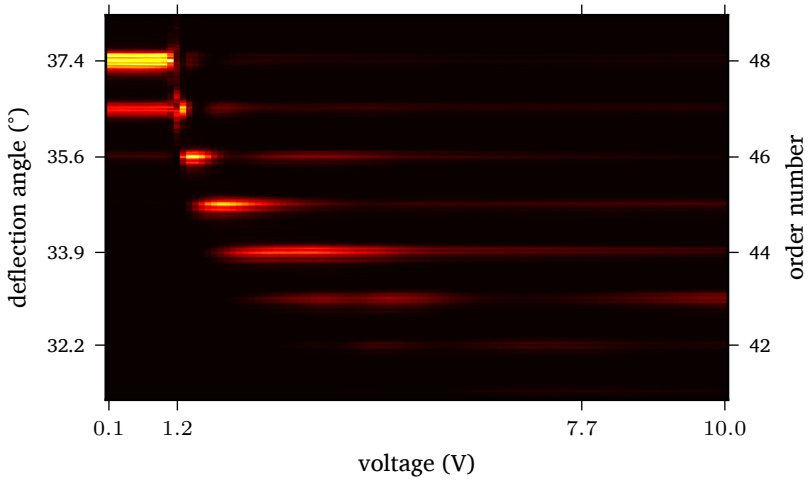

(b)

Fig. 3.27: Evolution of the diffraction pattern of the hybrid blazed grating as a function of the voltage applied between the two electrodes. Each vertical slice shows the diffraction pattern at a specific amplitude of an applied 1 kHz square wave electric signal. The deflection angles are relative to the grating normal, which is parallel to the incident laser beam. In (a) the evolution for unpolarized reflected light is shown, whereas (b) is the result from having another polarizer between the reflective grating and the detection screen.

far below the 22.6 % predicted by the simulation for that order and shown in

figure 3.18b. The fabricated device is slightly transparent, because the silver electrode on the grating is not thick enough: 3 % of the incident laser light is transmitted. Further comparison between the experiment and the simulations shows that there is a small difference in voltage at which steering starts. The biggest discrepancy between the two figures is found in the diffraction order that is most strongly excited at larger voltages: for the experiment, this is the 43rd order, whereas in the simulation it is the 42nd. It is believed this is due to small variations in the manufacturing process that lead to an error in the estimated height of the liquid crystal region, which would influence the electric field over the LC.

Remark that figure 3.27b shows the experimental results when another polarizer, whose transmission axis is parallel to the first polarizer, is inserted in the path of the reflected beams. Comparison of this figure to figure 3.27a shows that at low voltages most of the light undergoes no polarization rotation, but at intermediate to high voltages a larger amount of polarized light is converted to light of the perpendicular polarization. The reason for this can be explained with figure 3.9b: starting from intermediate voltages, the director tilts upwards, but because of the lateral component of the director, polarization rotation occurs. The simulation result of figure 3.18a shows the evolution of the diffraction pattern for unpolarized light, similar to figure 3.27a. A close inspection of figure 3.27b shows that there is a small angular difference of 0.1° in the lower diffraction orders compared to the angles of the same orders in figure 3.27a. This is merely due to beam displacement as it passes through the 2 mm thick polarizer.

3.4.3 Application: on–off steering using total internal reflection

Thus far, the hybrid grating has been studied when light is perpendiculary incident on it. In this way total internal reflection is avoided. By tilting the sample such that the angle of incidence is no longer 0°, the reflected diffraction orders could disappear completely due to total internal reflection. Indeed, for some angles of incidence, θ_i in figure 3.16, light will be totally internally reflected after passing through the liquid cystal layer. This TIR condition is given by

$$\theta_\mathrm{i}^\mathrm{TIR} = \arcsin\left(n_\mathrm{LC} \sin\left(\arcsin\left(n_\mathrm{LC}^{-1}\right) - 2\alpha\right)\right) \tag{3.11}$$

with n_{LC} the effective refractive index experienced by light as it propagates through the liquid crystal medium. Using the ordinary and extraordinary refractive indices of E7 at a wavelength of 633 nm, we find that when no voltage is applied, light would be totally internally reflected when $\theta_{\mathrm{i}} \geq \theta_{\mathrm{i}}^{\mathrm{TIR}_0} = 26.2°$, whereas if the liquid crystal would be fully switched, $\theta_{\mathrm{i}} \geq \theta_{\mathrm{i}}^{\mathrm{TIR}_\infty} = 31.4°$. This means that when $26.2° \leq \theta_{\mathrm{i}} < 31.4°$ light is totally internally reflected when no voltage is applied and is reflected in a similar way as discussed in the previous section, because the effective refractive index is decreased by applying an electric potential over the liquid crystal layer. This provides a way in which light can experience larger angular shifts.

To test this application the cell in figure 3.25 is tilted with respect to the incoming beam, so that the grating normal makes an angle of $(26.6 \pm 0.1)^\circ$ relative to the incoming beam. At this point, the diffraction orders with most intensity have just disappeared from the 180° field-of-view in front of the reflective grating. The detection screen and imaging setup of figure 3.25 are repositioned to image the diffraction orders that propagate nearly parallel to the grating.

In a similar way as before, we obtain a dataset from the diffraction patterns at different voltages, which is shown in figure 3.28a. Below 1.2 V, there is no light visible on the detection screen. In this TIR state, light eventually reaches the side edge of the grating and is there scattered at the glue boundary that holds the two substrates together, as shown in figure 3.28b. As the voltage increases, the effective refractive index of the LC decreases and the beam that propagates through the liquid crystal layer is no longer totally internally reflected: the diffraction pattern becomes pronounced again. The power in the diffraction order that makes the second smallest angle to the device surface is measured at 8.1 % of the incident power when the device voltage is at 3.5 V. When the voltage is switched off, less than 0.1 % is measured at that same position.

This experiment shows that by illuminating the grating at the edge under an oblique angle, light can be more than just directed to different angles: it can also be *guided* along the grating interface, as illustrated in the upper image of figure 3.28. Wave guiding is an important aspect of photonic integrated circuits. In the configuration shown here, the light guided by total internal reflection is eventually scattered due to the device's edge termination.

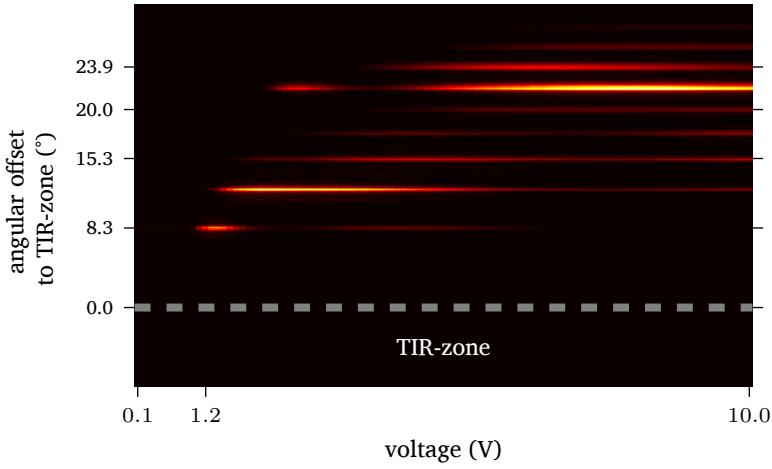

(a)

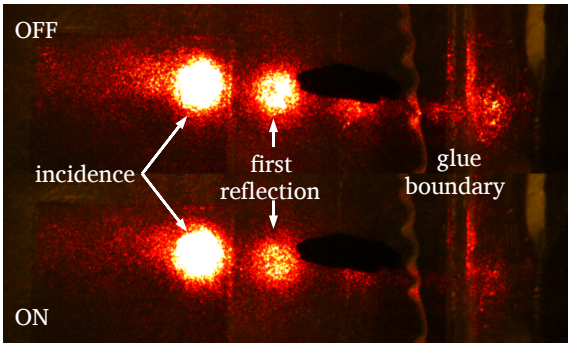

(b)

Fig. 3.28: Experimental results of 633 nm light obliquely incident on the reflective grating. The grating is tilted with respect to the incident beam at an angle of $(26.6 \pm 0.1)^\circ$. (a) By increasing the voltage, light is pushed out of the TIR-zone and steering to diffraction orders resumes. (b) Photos of the cell taken with a camera nearly perpendicular to the device. The voltage applied to the cell is 0 V in the upper photo, 10 V in the lower. The incidence spot is where the laser hits the upper glass substrate under an oblique angle. The first reflection is where the laser has traversed through the glass and LC layer, is reflected off the grating, propagates through the LC layer and glass layer again and hits the glass–air interface.

3.5 Summary

In this chapter, the combination of a blazed grating with a liquid crystal layer has been analyzed. Formulas from geometric optics were used to

come to elegant equations that predict the deflection angle of light as it propagates through or reflects from this structure. Numerical simulations have shown that these equations are good at predicting the overall deflection. The simulations could also predict the relative power in each of the diffraction orders. Several hybrid gratings have been fabricated, including gratings with a larger blaze angle and gratings with rotational symmetry. In this chapter, the results for one hybrid grating were presented and discussed. The gratings with different geometrical parameters were not characterized as fully as this one, as the assembly of LC cells using these gratings often introduced new manufacturing mistakes. These could be solved given more time. Nevertheless, the measurements on the presented grating show good agreement with the simulations in terms of deflection angle, number of excited orders and to a lesser degree the power distribution. Some of the deviations between the simulations and the experiments can be attributed to manufacturing details, which have been added to provide evidence to support the conclusions.

The fabricated device has also been used in a configuration in which one can electronically switch between total internal reflection and partial reflection. In this way, it could be useful for applications such as emergency lighting where escape routes could be illuminated by means of scattering, but in normal operation light could be directed elsewhere, for example to illuminate an image or an object.

3.6 References

1. Nikolova Kasarova, S., N. Georgieva Sultanova, C. Dimitrov Ivanov, and I. Dechev Nikolov, "Analysis of the dispersion of optical plastic materials", *Optical Materials*, vol. 29, no. 11, pp. 1481–1490, 2007. [Online] (cited on p. 57).
2. Inc., N. P. (2016). Adhesive index, [Online] (visited on 06/28/2016) (cited on p. 57).
3. Henry, C., *Microchip capillary electrophoresis: Methods and protocols*, ser. Methods in molecular biology. Humana Press, 2006. [Online] (cited on p. 61).
4. Si, G., Y. Zhao, E. S. P. Leong, and Y. J. Liu, "Liquid-crystal-enabled active plasmonics: A review", *Materials*, vol. 7, no. 2, p. 1296, 2014. [Online] (cited on p. 62).
5. Saleh, B. E. and M. C. Teich, *Fundamentals of photonics*. John Wiley & Sons, 2007 (cited on pp. 75, 79).
6. Beadie, G., M. Brindza, R. A. Flynn, A. Rosenberg, and J. S. Shirk, "Refractive index measurements of poly(methyl methacrylate) (pmma) from 0.4-1.6μm", *Appl. Opt.*, vol. 54, no. 31, F139–F143, 2015. [Online] (cited on p. 81).
7. Gross, S., D. Camozzo, V. Di Noto, L. Armelao, and E. Tondello, "Pmma: A key macromolecular component for dielectric low- hybrid inorganic–organic polymer films", *European Polymer Journal*, vol. 43, no. 3, pp. 673–696, 2007. [Online] (cited on p. 81).
8. Thomas, P., B. S. Dakshayini, H. S. Kushwaha, and R. Vaish, "Effect of sr2timno6 fillers on mechanical, dielectric and thermal behaviour of pmma polymer", *Journal of Advanced Dielectrics*, vol. 05, no. 03, p. 1 550 018, 2015. [Online] (cited on p. 81).
9. Shang, X., J.-Y. Tan, J. De Smet, P. Joshi, E. Islamaj, *et al.*, "Replicating micro-optical structures using soft embossing technique", vol. 9231, 2014, 92310H–92310H. [Online] (cited on p. 81).
10. Worgull, M., *Hot embossing: Theory and technology of microreplication*. William Andrew, 2009 (cited on p. 81).
11. De Coster, D., H. Ottevaere, M. Vervaeke, J. Van Erps, M. Callewaert, *et al.*, "Mass-manufacturable polymer microfluidic device for dual fiber optical trapping", *Opt. Express*, vol. 23, no. 24, pp. 30 991–31 009, 2015. [Online] (cited on p. 81).
12. Shang, X., J.-Y. Tan, **Willekens, O.**, J. De Smet, P. Joshi, *et al.*, "Electrically controllable liquid crystal component for efficient light steering", *IEEE Photonics Journal*, vol. 7, no. 2, pp. 1–13, 2015 (cited on p. 82).
13. Haller, I., H. Huggins, and M. Freiser, "On the measurement of indices of refraction of nematic liquids", *Molecular Crystals and Liquid Crystals*, vol. 16, no. 1-2, pp. 53–59, 1972 (cited on p. 85).

4

Beam-steering with high-κ materials

In the previous chapter a beam-steering device that uses two electrodes was studied. The propagation direction a of light beam is altered as it reflects or refracts at the LC–grating interface. Key to its functioning is the change in the refractive index in the LC layer when a voltage is applied and the *oblique* incidence on the slanted interface of the grating. The director in that device is fairly uniform over the entire LC domain. In contrast, a light beam will never change direction if it propagates through a homogeneously aligned liquid crystal that is sandwiched between two planar, *parallel* electrodes if the starting medium and ending medium are the same, regardless of the electric voltage between those two electrodes*. The beam could be offset though, but the propagation direction will not change. The reason for this is that the optical path length across the cell does not change. In the previous chapter, the OPL varied across the cell due to the slanted interface. A beam can also be diverted by devices that create a gradient in the refractive index, so-called gradient index (GRIN) devices. For example, in liquid crystal optical phased arrays (LCOPAs) the refractive index of the LC is changed gradually by using a series of closely spaced electrodes that are at different voltages relative to a common electrode [1–3]. A gradient in the index can also be generated using only 2 addressing electrodes by connecting these with a material that is much less conductive than the ground electrode, a technique that has already been discussed when introducing simulations in chapter 2. GRIN lenses using titanium oxide as the resistive layer and numerous one-dimensional beam-steerers employing either poly(3,4-ethylenedioxythiophene) polystyrene

*There exist situations where due to total internal reflection, the transmission through this planar device can be prevented, which is binary beam-steering: it can only send light in one of two fixed directions.

sulfonate (PEDOT:PSS) or metal oxides have been demonstrated [4–7]. In this chapter another way to induce a gradient in the refractive index will be studied. The outcome is similar to that of the beam-steering device using a highly resistive layer, but uses a dielectric material. It has the advantages that no current will flow, thereby reducing the generated heat which could be disadvantageous to the liquid crystal, as well as being able to be deposited over the electrodes, without the need for precise lithography mask alignment. In this chapter, the effect of this material on the optical path length will be studied and compared to the situation where that layer is missing. This technique opens up new possibilities for multi-electrode designs and one such possibility will be discussed in detail in the next chapter.

4.1 Revision of the three-electrode beam-steerer

The example that was used in chapter 2 to introduce the common analysis methods used in this thesis is a device where the electric potentials are defined at three positions using highly conductive materials. Between two of these three electrodes there is a bridging electrode with much lower coductivity which acts as a potential divider. While it does allow light beams to be steered to different angles depending on the applied voltages, it suffers from the drawback that a non-negligible current flows through the device, so it consumes a certain amount of power, which is released as heat and disturb the desired mesophase if the LC is heated beyond its transition temperature.

Liquid crystal devices are capacitive by nature: LCs do not conduct and because they are sandwiched between two closely spaced substrates, they act as a capacitor. It is instructive to study the change in equipotential lines of the 3-electrode device shown in figure 4.1. The electrodes (colored green) are not connected via a resistor and are surrounded only by dielectric layers. Each graph shows the contourlines of the electrostatic potential, $V(\vec{r})$, in a stack of isotropic dielectric layers with varying thickness and permittivity of each layer, simulated using FEM software that solves the Poisson equation for the electric field. One addressing electrode is held at a potential of 8 V, the other electrodes are grounded. From each graph to the next, only one change is made, which allows drawing the following conclusions:

a $\rightarrow$ b: As the thickness of the upper dielectric decreases, the lateral

spread in the electrostatic potential decreases;

b $\rightarrow$ c: A decrease in the permittivity of the upper dielectric, leads to a horizontal broadening of the contours;

c $\rightarrow$ d: The addition of a thin dielectric layer with a permittivity higher than those of the surrounding layers leads to a further increase in the lateral spread of the electrostatic potential;

d $\rightarrow$ e: As the dielectric permittivity of that additional layer increases, so does the lateral spread of the electrostatic potential;

e $\rightarrow$ f: The electrostatic potential is further broadened by an increase in that layer's thickness.

In figure 4.1f, the electric field lines in the upper dielectric layer, which are perpendicular to the equipotential surfaces, are more stretched along the x-axis. It is as if the electric field lines are more drawn to the region with higher dielectric permittivity. This is the low-frequency analogon of the well-known tendency of light to be attracted to regions with higher refractive index, which forms the basis of optical waveguides.

The potential along the dashed line connecting the two addressing electrodes has been made more linear by the addition of the dielectric layer. This situation is reminiscent of the resistive electrode studied in chapter 2, where the electrostatic potential between the two electrodes was linearly increasing. By replacing the upper dielectric in figure 4.1 with a liquid crystal we may reach an alternative type of beam-steering device that does not require a current to flow between the two addressing electrodes and still has an improved electrostatic field distribution. Unlike figure 4.1a, thick LC layers are usually not desirable, because it reduces the switching speed of the LC. The addition of a dielectric thus seems an interesting option to explore. The influence of the various parameters shown in figure 4.1 on an LC layer that is on top of it form the main subject of this chapter.

4.2 Lead zirconate titanate

Before studying the influence of the various parameters shown in figure 4.1, a quick side step is made to describe the properties of lead zirconate titanate (PZT), a material that is of special interest in this chapter and the next.

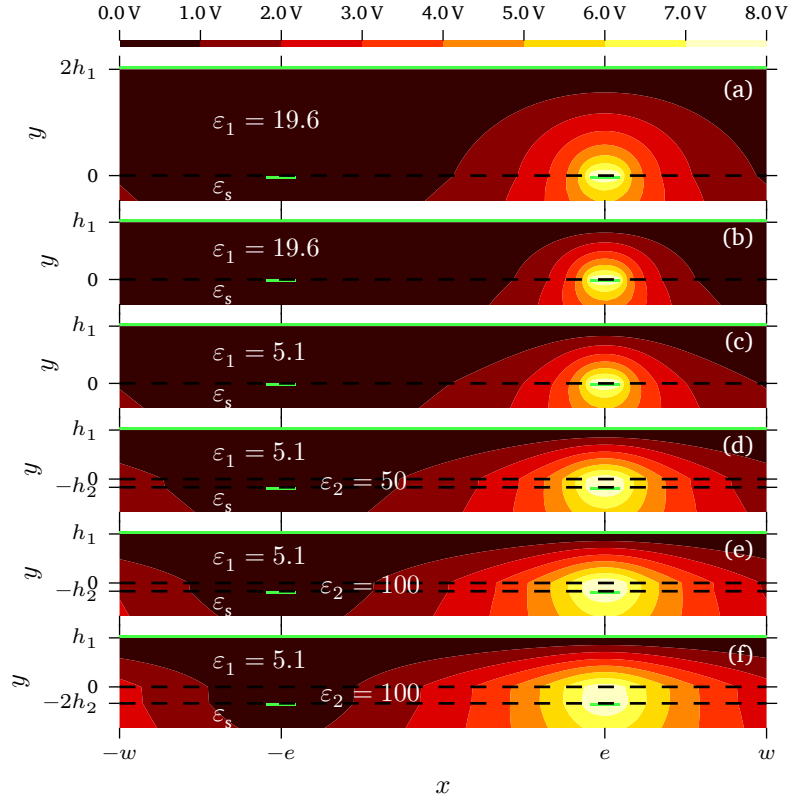

Fig. 4.1: Simulated potential distribution in stacks of isotropic dielectrics. The position and size of the electrodes is given by the green patches and the dashed lines represent the interfaces between the dielectrics. Periodic boundary conditions are applied to the sides. In each of the graphs, only a part of the bottom substrate (with ε_s) is shown, the potential distribution in it is not of interest. The simulation assumes *all* layers are isotropic dielectrics with $h_1 = 5\,\mu\text{m}$, $h_2 = 0.84\,\mu\text{m}$ (only present in (d), (e) and (f)), $h_s = 40\,\mu\text{m}$, $w = 33\,\mu\text{m}$ and $e = 16.5\,\mu\text{m}$. The permittivity of the bottom substrate is $\varepsilon_s = 7.4$, a typical value for glass. The two values used for ε_1 are the same as $\varepsilon_\perp$ and $\varepsilon_\parallel$ of the liquid crystal E7 (table 2.1).

4.2.1 Properties and uses

PZT is a ceramic material that exhibits a large piezo-electric coefficient, electro-optic coefficient and, of special interest for the LC-based beam-steering devices studied here, a large dielectric constant [8, section 10.3]. Materials with a large dielectric coefficient are more commonly known in the field of microelectronics as high-κ materials and appear there frequently as the

dielectrics in thin-film capacitors and piezo-electric actuators[9–13]. The reason its properties are explained here is that the LCP group has recently acquired the know-how to deposit the material on various substrates [14] and due to its high dielectric permittivity and optical transparency of thin micron-sized PZT layers, it is an excellent candidate for beam-steering devices based on this technology.

The origin of the high dielectric permittivity of PZT is found with its large permanent dipole moment, which is the result of its perovskite crystal structure. The LCP group has developed a cost-efficient method based on chemical solution deposition (CSD) that allows the growth of high-quality poly-crystalline layers of PZT on different types of surfaces [14]. Figure 4.2 shows a scanning electron microscope (SEM) micrograph of a PZT layer deposited on a silicon substrate. Each single grain has a diameter of about 80 nm and the layer has a thickness of approximately 100 nm*.

A. *Dielectric constant*

To measure its permittivity, a cylindrical capacitor is made by growing a PZT film of 1 µm on top of a metallic disc, measuring 3.14 mm^2 in area. It is capped at the same location by another metallic patch of the same dimensions. The small-signal capacitance, $C(f)$, is measured from which the relative dielectric permittivity, ε_r is calculated, assuming the parallel plate capacitor model,

$$C(f) = \varepsilon_0 \varepsilon_r(f) \frac{A}{d}, \tag{4.1}$$

accurately describes the capacitor. In this model A and d are the area of the electrodes and the spacing between them respectively, and ε_0 is the

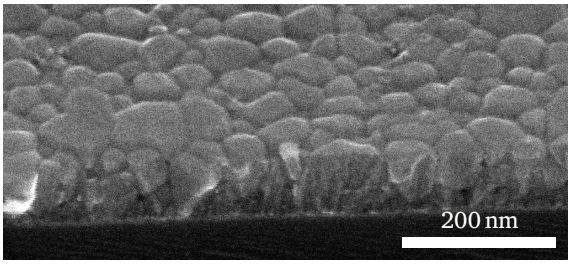

Fig. 4.2: SEM micrograph of polycrystalline PZT deposited on a silicon wafer.

*The layer is imaged at an angle of 52°, which has to be taken into account when estimating the thickness based on the scalebar.

permittivity of vacuum. The relative permittivity of PZT is shown in figure 4.3 for a range of frequencies and for two different plate materials: indium tin oxide (ITO) and platinum (Pt). The measured permittivity for the ITO-plated capacitor decreases around 10 kHz, because resistance–capacitance (RC) effects start to play a role, due to the finite conductivity of ITO. The Pt-plated capacitor shows a constant permittivity, as expected, for all measured frequencies up to 2 MHz, because Pt has an electrical conductivity that is several orders of magnitude larger than that of ITO. For frequencies around 1 kHz, which are the frequencies of interest for typical nematic LCs, the relative permittivity reaches a value of 561. This value is comparable to that found in other studies where PZT was deposited on metal foils using sol-gel processing and rf-sputtering [15–18]. Values above 1000 have been reported [19, 20].

B. *Transmission spectrum*

For applications where light is transmitted through thin layers of PZT, the transmission spectrum of the material is of interest. Figure 4.4 shows the measured transmission spectrum of two PZT-coated glass substrates. The substrates are 1.1 mm thick Corning® glasses (Delta Technologies, Ltd, product code CB-90IN-0111). Corning® glass is a type of boro-aluminosilicate glass that is commonly used in displays. The glasses are coated on one surface with ITO, having a thickness in the range 15 nm–30 nm.

Comparison of the spectra of the PZT-coated substrates to the spectrum

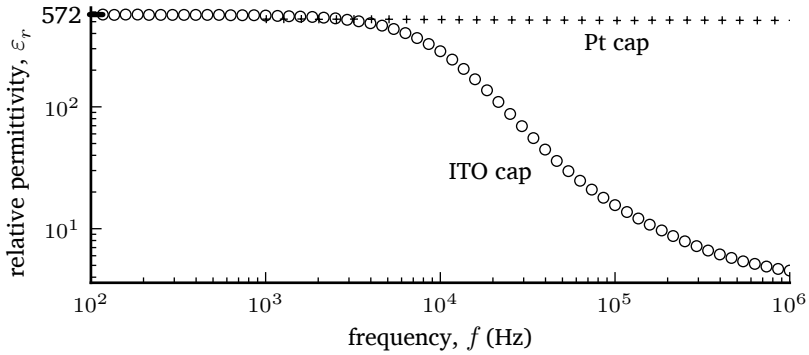

Fig. 4.3: The permittivity of PZT, measured by using it as the dielectric material in a parallel plate capacitor. Results are shown for measurements where the capacitor plates are constructed from either platinum or ITO.

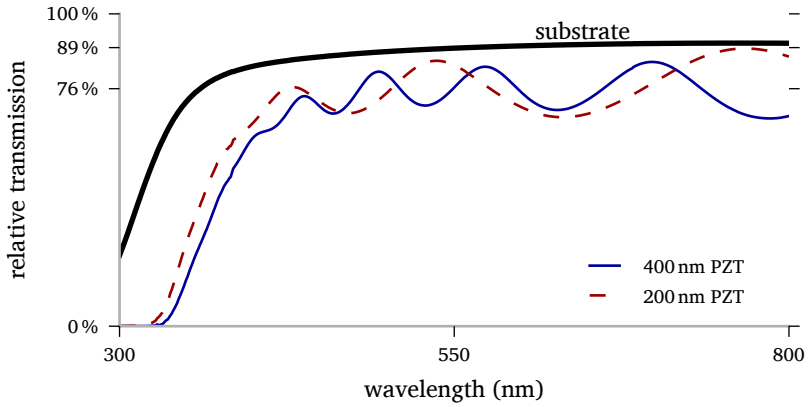

Fig. 4.4: Measured transmission spectra of two PZT-coated substrates. The transmission spectrum of the substrate, which also has an ITO coating, is given as well: its transmission is low for small wavelengths, because of the absorption of ITO in the UV. The illuminated stack of layers is thus PZT, ITO and glass, in that order. The ringing of the spectra arises from the interference of multiple partial reflections [21].

of the reference substrate, gives an idea of the amount of light that is being reflected and absorbed. By taking the average over the wavelength range 460 nm–700 nm, a relative transmission of 76 % is obtained for the substrate coated with a 400 nm thick PZT layer. Relative to the 89 % average relative transmission of the substrate, that is an increase in loss of 15 % (or 13 percentage points).

4.2.2 Integration with liquid crystal cells

The process of applying a layer of PZT on top of a glass substrate to be used in an LC application is outlined in figure 4.5. The chemical processes with which the buffer layers and PZT are manufactured, are explained in detail in [14]. Due to the high temperatures involved during the annealing phase (600 °C and more), a type of glass should be used that can withstand such temperatures without deformation (low thermal expansion coefficient). The glass substrates used here are the Corning® glasses discussed earlier, which can withstand such temperatures.

After 3 to 4 iterations of spincoating a single layer of PZT, the deposited material needs to be annealed. As a single layer of PZT is approximately 60 nm thick, to reach a thickness of about 1 µm, the annealing process will

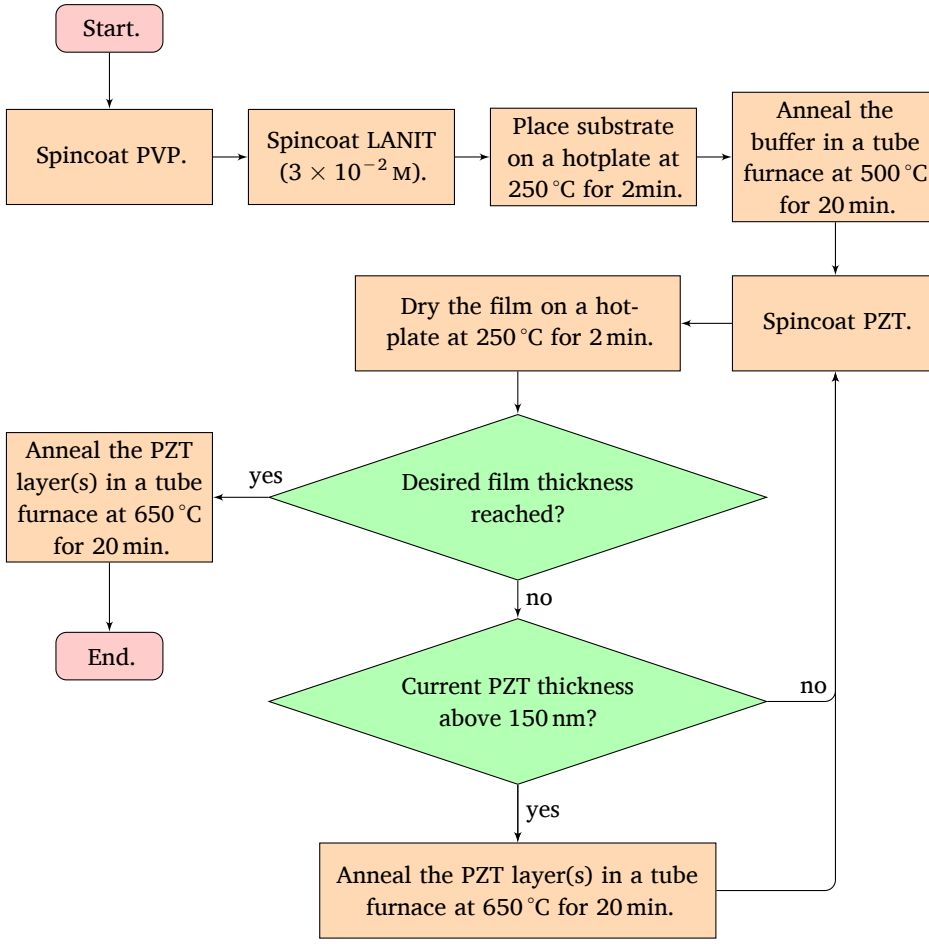

Fig. 4.5: Process flow for applying PZT to a substrate. PVP is polyvinylpyrrolidone and improves the adhesion of LANIT, which is lanthanide nitrate and prevents the diffusion of PZT into the coated substrate.

need to be repeated about 4 times. The deposition of PZT on substrates used for the work presented here is handled by John PuthenParampil George.

4.3 Experimental verification

Figure 4.6 shows photos of two liquid crystal cells observed using a microscope. Each cell is placed between crossed polarizers and is illuminated in transmission. They both feature a planar electrode that covers one substrate entirely and have the same interdigitated electrode pattern, shown schematically in

figure 4.6a, on the other substrate. The cells have been rubbed in a direction perpendicular to the thin electrodes. The cell in figure 4.6c differs from that in figure 4.6b by the presence of a PZT layer that has been added on top of the electrode pattern, prior to coating with nylon for the alignment layer.

The larger electrode section in the upper right corner and the digitated electrodes connected to it are at 5 V, while the other digitated electrodes in the same plane are at 0 V. The homogeneous transparent electrode that is above this plane is also at 0 V (not shown). The color variations along the rubbing direction in the midsection of the micrographs are an indication for the variation of retardation that light experiences. In figure 4.6b the color variations between the equal-potential electrodes are large, ranging from yellow to green to red, which hints at a large lateral variation in the tilt of the

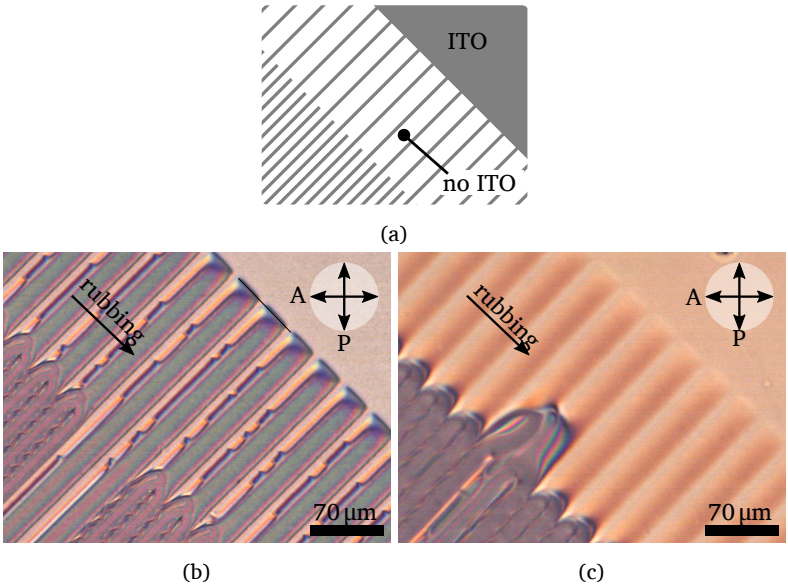

Fig. 4.6: Comparison of electrically switched liquid crystal (E7) over digitated electrodes, observed under the microscope and placed between crossed polarizers (transmission axis indicated). In (a), the bottom electrode pattern is schematically illustrated (the top electrode is homogeneous). The labelled ITO electrode is held at 5 V, all other electrodes are grounded. In (b) and (c), the LC is sandwiched between the ITO-coated top glass substrate and the patterned bottom substrate. In (c), a 0.64 µm thick layer of PZT is present between the LC and the patterned bottom substrate. The arrow indicates the rubbing direction on the bottom substrate, which is anti-parallel to that of the upper substrate (not shown).

director. In figure 4.6c the color variations in the same region are very small, the hue is approximately constant. This indicates that the director tilt barely changes in the lateral direction over these small interelectrode distances. It is as if the liquid crystal over the bottom interelectrode gap behaves as if it were over a planar electrode.

The intensity profile between two thin electrodes that are at the same potential in figure 4.6c is asymmetric. The reason for that is that there is a mismatch between the alignment imposed by the electric field and the alignment imposed by the alignment layer. This will be verified numerically in section 4.4.2.A.

These initial experimental results are promising, because they show that a liquid crystal does not necessarily need to be sandwiched between electrodes everywhere in order to switch. This could lead to a reduction in the amount of transparent conductive materials required for many LC technologies, which simplifies the design of the electronic drivers. If the interelectrode spacing could be made much larger than shown here, the addressing electrodes could even be made from non-transparent materials without a noticeable decrease in transmitted intensity.

4.4 Numerical analysis of PZT-influence

The experimental results from figure 4.6 invite us to study the influence of the PZT layer (or any layer with high dielectric constant) on the director in a quantitative manner. While the Michel-Lévy chart [22, 23] could be used to get (approximate) quantitative data on the retardation, and thus the director tilt, we have FEA tools at our disposal, which will be used in the next sections.

4.4.1 Influence of the substrate thickness

For the FEM simulations that will be discussed in this chapter, modelling the bottom substrate to realistic scales compared to the size of the liquid crystal layer (200:1) would require far too much computation time. It is tempting to reduce the thickness of the bottom substrate to the minimum of 0 µm, in order to reduce the size of the computational domain. This seems reasonable as we are not interested in the electric field distribution within the bottom substrate, which is typically glass. However, in chapter 2 it was mentioned that the

thickness of the bottom substrate of the LC cell influences the simulation results. The reason for this is that some of the electric field lines emanating from the addressing electrodes will extend into the glass region before ending up at the ground electrode. The ground electrode, which covers the entire upper substrate, does not have this problem, because it is assumed to extend infinitely in the horizontal direction.

An upper bound on the required thickness of the bottom glass layer can be determined by studying the absolute error of the electrostatic potential, which is defined as:

$$\mathrm{err}_i := \left| V_{h_i}(\vec{r}) - V_{h_{1000}}(\vec{r}) \right| \qquad \text{with} \quad \vec{r} \in \Omega_{\mathrm{LC}}\,, \tag{4.2}$$

where $V_{h_{1000}}(\vec{r})$ is the electrostatic potential when the thickness of the glass layer is 1000 µm, $V_{h_i}(\vec{r})$ is the scalar potential in the mesh with a different thickness for the glass layer and Ω_{LC} is the liquid crystal domain defined in the FEM simulations (see section 2.2.1). Equation (4.2) should be evaluated for every geometry to ensure the chosen thickness was sufficient to model the physics accurately. But a lot can already be learned from the simple geometry shown in figure 4.7. It is essentially a dual electrode device, with one homogeneous ground on the upper substrate and one periodically repeating addressing electrode on the lower substrate.

This geometry consists of 4 layers: from the top to the bottom these represent the liquid crystal, the high-κ dielectric, a thin buffer layer and

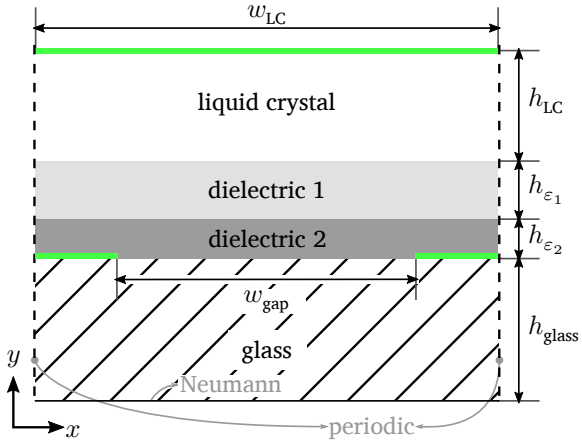

Fig. 4.7: Geometry for deriving of an upper bound on h_{glass}. The green patches represent the electrodes.

a bottom glass substrate. The reason a second dielectric layer is present, is because the bonding process of the high-κ material to the glass often requires a buffer layer, as explained in section 4.2.2. The thickness of this buffer layer is often negligible compared to the high-κ dielectric layer, but its relative dielectric constant is typically much lower ($\epsilon_{2,r} < 20$), so it is not unreasonable to take it into account. Our interest goes out to the influence of the first dielectric layer, so all other references to "the dielectric layer" in the following paragraphs refer to the first dielectric layer with high dielectric constant.

Intuitively one might expect the error of the electrostatic potential to be largest furthest away from the addressing electrode. Figure 4.8 shows that this is indeed the case. It is a visual representation of equation (4.2), in the absence of a dielectric layer ($h_{\varepsilon_1} = 0\,\mu\text{m}$). The electrodes, not technically part of the LC domain, have been added as an overlay, with exaggerated thickness.

Figure 4.9 shows the maximum absolute error in the LC domain as a function of the thickness of the bottom glass substrate for both the reference case and the case where the dielectric layer ($\epsilon_1 = 550$) is present. Note that the x-scale is logarithmic. The graph shows that the error decreases slowly, with increasing thickness of the glass layer. It also indicates that the absolute error is reduced to less than 0.025 V in both cases, once the glass layer is more than about 20 µm thick. This absolute error, compared to the potential difference between the addressing electrode and the ground (5 V), is an error of less than 0.5 %. Very little benefit is to be found in increasing the glass layer thickness beyond about 20 µm.

Care should be taken when generalizing the result of figure 4.9: the

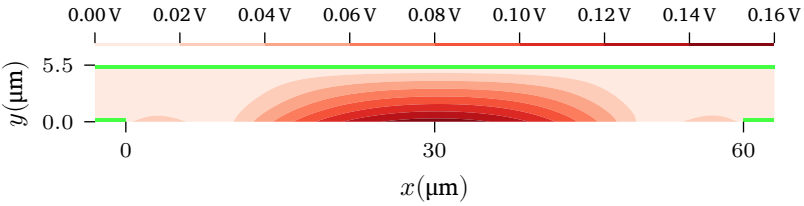

Fig. 4.8: Visualization of the absolute error defined in equation (4.2), when the thickness of the glass layer is 10 µm and the potential difference is 5 V. Dielectric layers are not present.

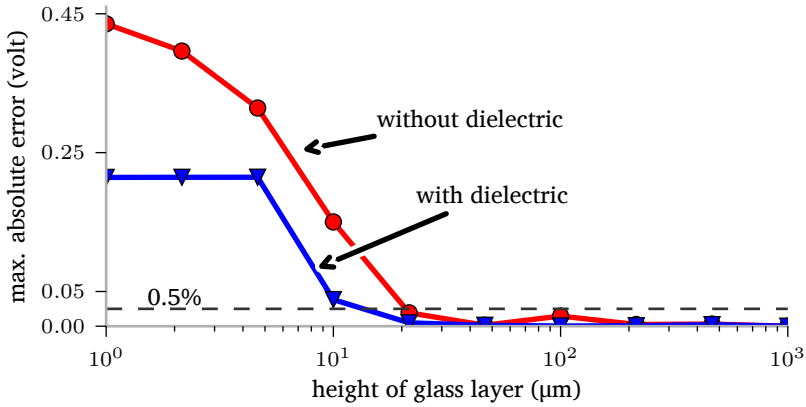

Fig. 4.9: The maximum of the absolute error in the potential distribution in the LC domain as a function of the thickness of the bottom substrate. For these results, the LC layer is 5.5 µm thick, the dielectric 0.84 µm thick and has a permittivity of $\epsilon_1 = 550$, while the interelectrode spacing is 60 µm.

director profile of a 5.5 µm thick layer of liquid crystal is simulated using an electrode spacing of $w_{\text{gap}} = 60\,\mu\text{m}$, the largest gap size that is taken into consideration. When these geometric parameters change, the absolute error will be different. Changes in the physical constants of the problem will have similar effects. For the upcoming simulations, a general guideline derived from the previous observation is followed stating that the glass layer thickness should be about the size of the interelectrode spacing to reduce the error sufficiently.

4.4.2 Influence on the average refractive index

Many electro-optic applications involving liquid crystals only consider two states: a voltage-ON state, where the liquid crystal is fully switched, and a voltage-OFF state, where the liquid crystal is in its initial state, which is largely determined by the boundary conditions imposed by the alignment layers, such as anchoring strength and pretilt. In both cases the physics can usually be simplified by considering the average refractive index experienced by light propagating through the LC layer, which is proportional to the optical path length:

$$\langle n \rangle = \frac{1}{d} \int_0^d n_{\text{eff}}(y) dy \,, \tag{4.3}$$

where d is the thickness of the LC layer and $n_{\text{eff}}(y)$ is the effective refractive index at a height of y within the layer, and is defined by equation (3.7). The tilt of the director, θ in that definition, is here the angle between the director and its projection on the xz-plane, which is perpendicular to the propagation direction of light along the y-axis..

A. *Influence of the Permittivity*

Shown in figure 4.10 are the simulated director profiles of the LC cell geometry shown in figure 4.7, for two cases: in figure 4.10a the dielectric layer has a relative permittivity of $\epsilon_r = 20$, in figure 4.10b $\epsilon_r = 550$. A pretilt of 2° (counterclockwise from the x-axis) was imposed, with strong anchoring (polar and azimuthal anchoring set to $W_\theta = W_\phi = 1 \times 10^{-3}\,\mathrm{J\,m^{-2}}$). In both cases, an electric potential difference of 3 V was applied between the ground and the addressing electrodes. This potential is sufficient to switch the liquid crystal in the region between the ground and the addressing electrodes from its planar alignment to a direction almost perfectly perpendicular to the ground; the director tilt is close to 90°. As the distance to the addressing electrodes increases, the director tilt decreases. This change occurs faster when the permittivity of the dielectric layer over the addressing electrodes is lower (figure 4.10a). One region in figure 4.10a stands out: at the left and right sides of the addressing electrode, the director is tilted in opposite ways due to the inhomogeneity of the electric field near the electrode. At the left edge of the electrode this clockwise reorientation opposes the pretilt imposed by the alignment layer ($\theta|_{z=0,d} = 2°$) and a bend wall is formed, which is a type of elastic deformation where the director bends around a common point and introduces two regions in the LC with opposing director orientations [24]. The bend wall is one of several types of domain walls, that are also known as Brochard–Leger walls, and transform to disclinations at higher voltages [24–26]. A similar profile is observed in absence of the dielectric layer and the transformation of the domain wall into a disclination line is shown in the supplementary video accompanying my article on the combination of PZT and LCs [27]. Figure 4.10b indicates that a value of 550 for the permittivity of the dielectric layer prevents the formation of such a domain wall and the director profile assumes a counterclockwise tilt over the entire domain.

The average refractive index, equation (4.3), can be computed numerically

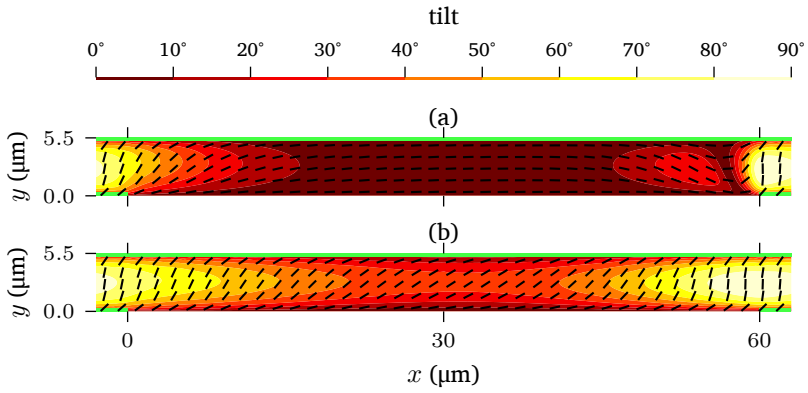

Fig. 4.10: The director profile of the liquid crystal domain when a potential difference of 3 V is applied between the addressing electrode and the ground. The electrodes are shown in green. In (a) the permittivity of the dielectric layer over the addressing electrodes is $\epsilon_r = 20$. In (b) $\epsilon_r = 550$. A domain wall can be seen to the left of the electrode on the right in (a).

from these simulation results in a similar way as the Jones phase profile was calculated in section 2.2.2.A. It is shown in figure 4.11, as a function of the position over the dielectric layer, for different values of the dielectric constant of the dielectric layer ϵ_1, when the applied potential is 3 V.

We begin the discussion of figure 4.11 by noting that the average refractive

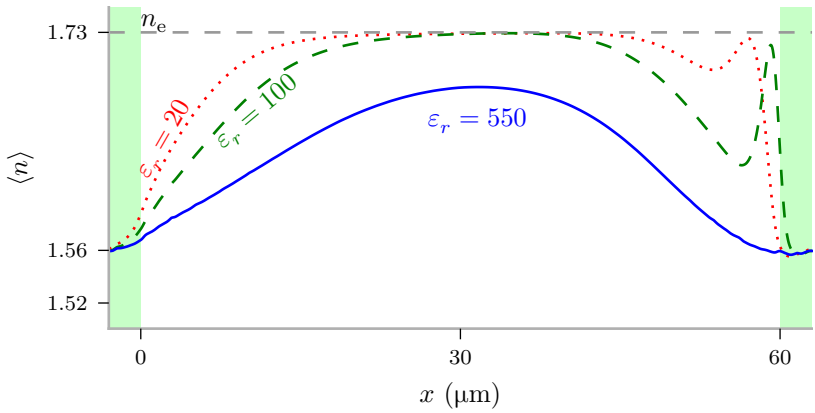

Fig. 4.11: The average refractive index for monochromatic light ($\lambda = 633$ nm) linearly polarized along the rubbing direction and travelling parallel to the interface normal of the cell shown in figure 4.7. The simulations assume the thickness of the dielectric layer is 0.84 µm and the addressing electrodes are held at 3 V.

index sensed over the addressing electrode (i.e. $x < 0\,\mu m$ or $x > 60\,\mu m$) is largely independent of the dielectric constant of the dielectric layer, and always close to a value of 1.56, which is to be expected: as shown in figure 4.10, the director above the addressing electrode will be mostly 90° tilted, such that light experiences mostly n_o. As the distance to the electrode to the left increases, $\langle n \rangle$ increases and levels off at a value of 1.73, which is the extraordinary refractive index of E7 at the simulated wavelength of 633 nm. This indicates that the liquid crystal has not switched at the position where $\langle n \rangle \approx n_e$. The position where $\langle n \rangle$ levels off is moved further away from the electrode as the permittivity of the dielectric layer increases. For $\epsilon_r = 550$ there is no levelling. Close to the left edge of the electrode, an oscillation in $\langle n \rangle$ can be observed. The explanation for this is found in the earlier analysis of the director profiles: in the domain wall of figure 4.10a, the director tilt varies rapidly between two angles with opposite sign and passes 0° in between. Where it is 0°, linearly polarized light will experience the extraordinary refractive index of the liquid crystal.

From these simulations, we can conclude that:

- starting from a certain value for the permittivity of the dielectric layer, the occurence of domain walls can be prevented,
- with a 0.84 µm thick dielectric layer with permittivity $\varepsilon_r = 550$ coated over the electrodes, the director is tilted everywhere in the cell, even in the middle, although the tilt is not homogeneous in a cell with 60 µm interelectrode distance.

B. *Influence of the Electrode Spacing*

The interelectrode spacing will also influence the average refractive index. As the interelectrode spacing decreases, the optical path length becomes more easily controllable. Once a specific spacing is fixed, it could be possible to still get reasonable control over the optical path length, by tuning the permittivity of the dielectric layer (as shown in the previous section) or by tuning the thickness of the dielectric layer.

Figure 4.12 shows the average refractive index experienced by monochromatic light ($\lambda = 633\,nm$) travelling along the interface normal of figure 4.7, when the potential difference between the ground and the addressing electrode is 2 V, for a range of interelectrode spacings. To allow easy comparison, the

distance between the addressing electrodes has been normalized, because the geometry width (w_{LC} in figure 4.7) changes with the interelectrode spacing.

Here too, the refractive index experienced just above the addressing electrodes is nearly independent of the interelectrode spacing and for the same reason explained earlier. Note that $\langle n \rangle$ over the electrodes (located around $x = 0$ and $x = 1$) is a bit larger than in figure 4.11, because only 2 V is applied, so the electric field is weaker, which results in a smaller tilt compared to the situation shown in figure 4.10. A nearly constant index profile is obtained when the interelectrode spacing is 12 µm with $\epsilon_r = 550$. At this point the ratio of the width of the electrodes to the interelectrode gap is reduced to 50 %, so the intensity reduction in transmission would be large if the addressing electrodes were made in a non-transparent conductive material. To solve this, the 6 µm broad electrodes could be made less wide.

4.5 Use as a one-dimensional beam-steerer

Now that the influence of high-κ dielectrics has been studied numerically, a proof of concept beam-steering device is fabricated and tested.

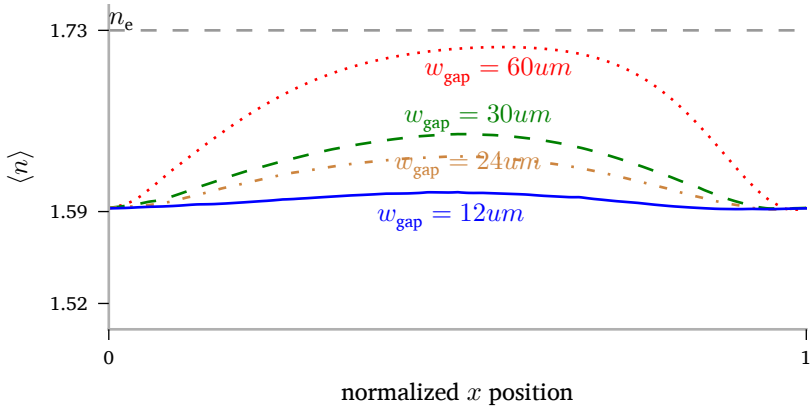

Fig. 4.12: The average refractive index for monochromatic light ($\lambda = 633$ nm) travelling parallel to the interface normal of the cell shown in figure 4.7. The linearizing effect of the dielectric layer ($\epsilon_r = 550$, $h_{\epsilon_1} = 0.84$ µm) is limited by the interelectrode spacing.

4.5.1 Device geometry

The device features an asymmetric interdigitated electrode pattern, like the ones shown in figure 2.10b, using platinum as the conductor. The largest interelectrode spacing is 52 µm and the smallest 6 µm. The width of each addressing electrode is also 6 µm. On top of this electrode pattern a 0.8 µm thick layer of PZT is deposited. Nylon is subsequently spincoated over this surface as well as over an ITO-coated glass substrate and afterwards rubbed. Both substrates are glued together to create the LC cell cavity that is then filled with the nematic LC mixture E7 by means of capillary forces, as described in chapter 2. Figure 4.13 shows micrographs of this cell, observed between crossed polarizers.

A variation on this device is made for comparison: it does not feature the PZT layer. Both devices use 10 µm spacers to separate the substrates, but post-assembly measurement indicates that the gap for the PZT-enhanced device is 23.4 µm and for the reference device it is 13.6 µm. This measurement uses the interference fringes that arise from multiple partial reflections at the cell cavity's interfaces when the cell is illuminated with quasi-monochromatic incoherent light [21]. Because the LC layer is about 4 times as thick as the LC layer used in the simulations of section 4.4, the linearization of the electric

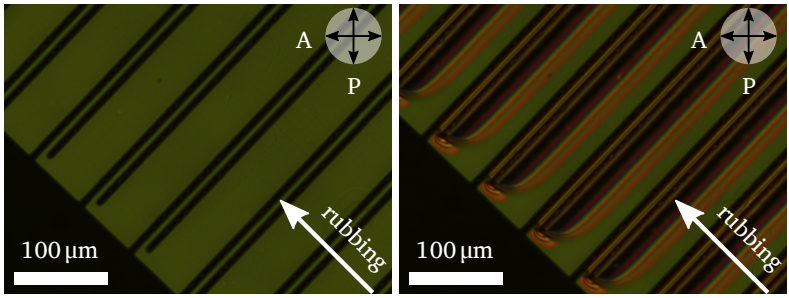

(a) (b)

Fig. 4.13: Micrographs of a liquid crystal cell with an asymmetric opaque interdigitated electrode pattern at the bottom substrate and a homogeneous transparent electrode at the top, imaged between crossed polarizers. The bottom substrate is coated with a PZT layer of 0.8 µm. The arrow indicates the rubbing direction along the bottom substrate, used to achieve anti-parallel alignment in the cell. In (a), all electrodes are grounded. In (b), one set of digitated electrodes is at 5 V relative to the homogeneous ground and the other digitated electrodes.

potential between the addressing electrodes is expected to be better, as was shown in figure 4.1.

4.5.2 Simulation results

The director profile for the PZT-enhanced device is simulated for a range of voltages. The results are shown in figure 4.14. The figure shows that the director tilt increases gradually over the entire LC layer, even at a considerable distance from the lower right addressing electrode.

The phase profile of a monochromatic ($\lambda = 633\,\text{nm}$) plane wave incident on the device along the y-axis and linearly polarized along the x-direction is calculated, as it emerges, using the Jones formalism. This is done for each of the applied voltages shown in figure 4.14. The result from these calculations is shown in figure 4.15.

The figure shows that, in the region between the two addressing electrodes, the slope of the phase of the wave initially increases, but starts to level off again at higher voltages.

4.5.3 Measurement results

A measurement setup almost identical to the one shown in figure 3.25 is used to capture the diffraction profile at different voltages. The setup is changed to work in transmission. Figure 4.16 shows the diffraction profiles of a HeNe-laser when one of the addressing electrodes is grounded and the other electrode is held at a potential that is labelled in the figure. The graphs show that above 3.5 V the diffraction pattern of the reference device hardly changes. Between 0.0 V and 3.5 V, the brightest diffraction order has shifted by one, $m = 0 \rightarrow 1$. In comparison, the beam-steering abilities of the PZT-enhanced cell are better, as shown in figure 4.17: it shows the diffraction patterns of the PZT-enhanced cell in the same measurement setup that was used to generate figure 4.16.

The deflection of the laser beam reaches a turning point at approximately 3.5 V, where the most intense order is number $m = 9$, which propagates at an angle of 4.7°. The reduction in the beam-steering angle at voltages higher than 3.5 V for the PZT-enhanced cell could be explained using figure 4.15. In that figure a decrease in the slope of the phase of the wave is visible after the addressing electrode reaches 3.5 V.

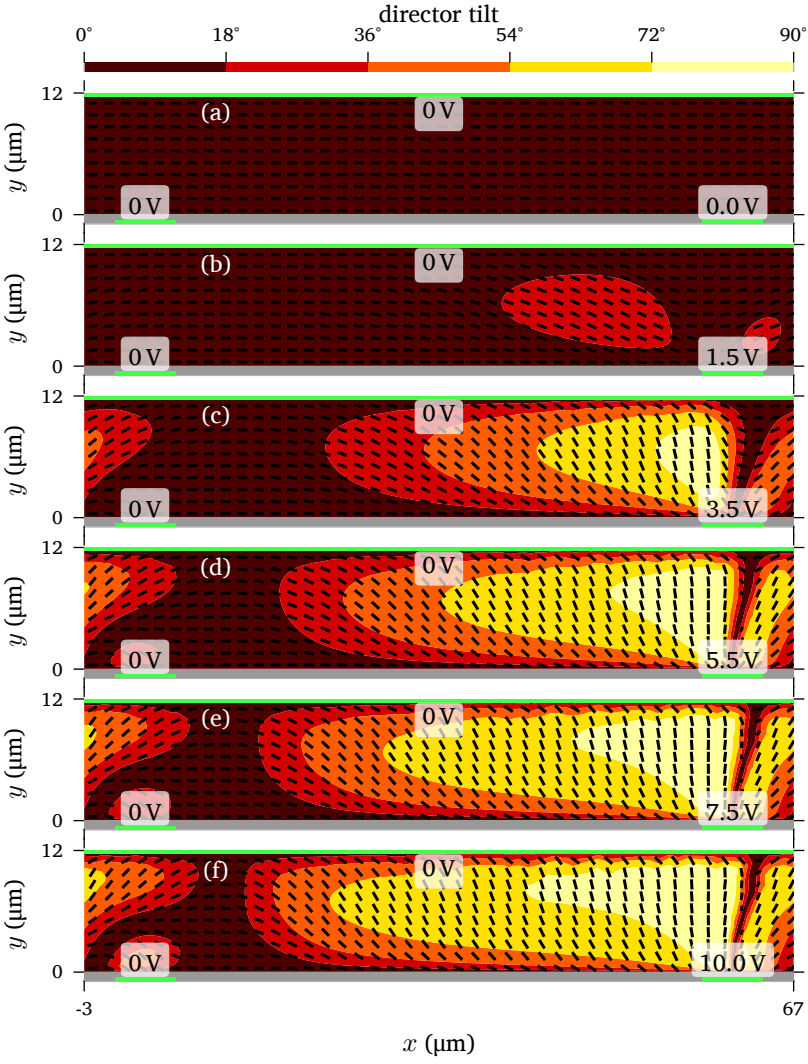

Fig. 4.14: Director profiles for a beam-steering device with a 0.8 µm thick PZT layer (shown in grey) coated over the lower addressing electrodes (shown in green). In each graph the electric potential of the lower right electrode is adjusted. The tilt of the director is indicated as well with the background color.

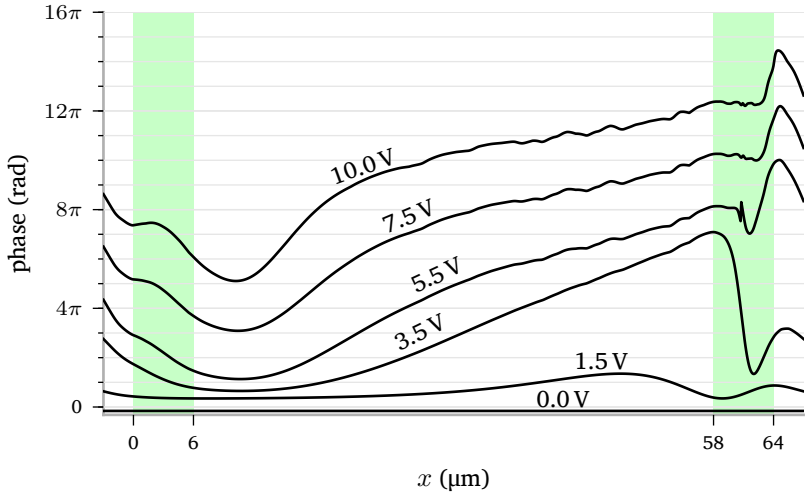

Fig. 4.15: Simulated phase profiles of a wave emerging from the PZT-enhanced beam-steerer. The phase profiles have been offset vertically for clarity. The green patches mark the locations of the addressing electrodes, one of which has the potential indicated near the phase profiles.

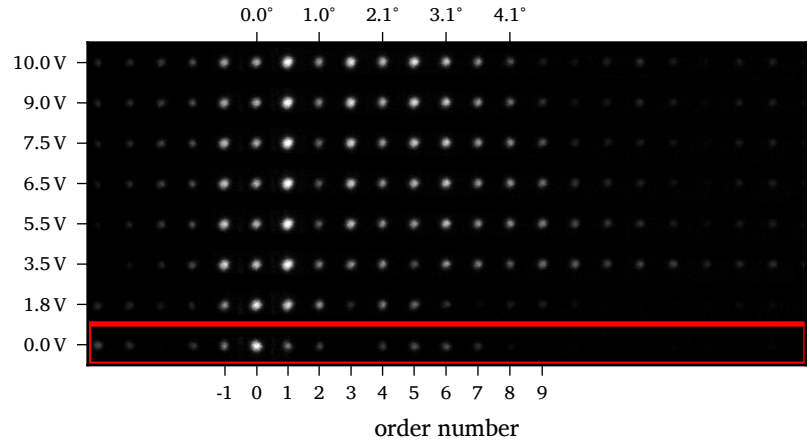

Fig. 4.16: Measured evolution of the diffraction pattern of the reference beam-steerer. The red frame indicates a single diffraction pattern. Adapted from [28], with permission.

4.6 Summary

In this chapter, it was shown that a dielectric layer with high permittivity can be used to create a more linear gradient in the electrostatic potential between

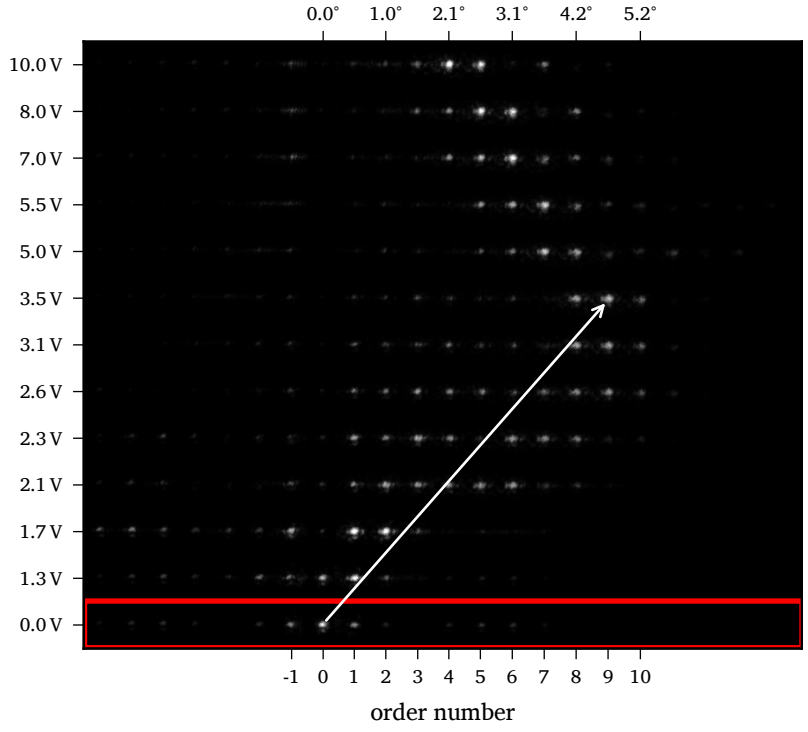

Fig. 4.17: Measured evolution of the diffraction pattern of the PZT-enhanced beam-steerer. The red frame indicates a single diffraction pattern. Adapted from [28], with permission.

two addressing electrodes, similar to the effect of connecting them with an electrically conductive material with high resistivity. The capacitive bridge extends the electric field laterally from the electrodes and can thus be used to switch a liquid crystal farther away from the usual influence field of the electrodes. The dielectric layer thickness is an important design parameter, given the interelectrode spacing. Using FEM simulations it was also shown that a 0.84 µm thick dielectric layer with $\epsilon_r = 550$, a value that can be reached by certain ferroelectric materials such as PZT, can be used to prevent the appearance of domain walls in certain liquid crystal devices. Finally, it was experimentally verified that in a liquid crystal cell featuring asymmetric interdigitated electrodes, the angular beam-steering range and quality of the diffraction patterns is improved considerably when the patterned substrate is coated with a 0.8 µm thick PZT layer.

4.7 References

1. McManamon, P. F., P. J. Bos, M. J. Escuti, J. Heikenfeld, S. Serati, *et al.*, "A review of phased array steering for narrow-band electrooptical systems", *Proceedings of the IEEE*, vol. 97, no. 6, pp. 1078–1096, 2009 (cited on p. 95).
2. Resler, D. P., D. S. Hobbs, R. C. Sharp, L. J. Friedman, and T. A. Dorschner, "High-efficiency liquid-crystal optical phased-array beamsteering", *Opt. Lett.*, vol. 21, no. 9, pp. 689–691, 1996. [Online] (cited on p. 95).
3. Xiao, F. and L.-j. Kong, "Angular magnification method of liquid crystal optical phased array based on telescope system", vol. 8906, 2013, pp. 89062C–89062C–8. [Online] (cited on p. 95).
4. Naumov, A. F., M. Y. Loktev, I. R. Guralnik, and G. Vdovin, "Liquid-crystal adaptive lenses with modal control", *Opt. Lett.*, vol. 23, no. 13, pp. 992–994, 1998. [Online] (cited on p. 96).
5. Shang, X., A. M. Trinidad, P. Joshi, J. De Smet, D. Cuypers, *et al.*, "Tunable optical beam deflection via liquid crystal gradient refractive index generated by highly resistive polymer film", *IEEE Photonics Journal*, vol. 8, no. 3, pp. 1–11, 2016. [Online] (cited on p. 96).
6. Klaus, W., M. Ide, S. Morokawa, M. Tsuchiya, and T. Kamiya, "Angle-independent beam steering using a liquid crystal grating with multi-resistive electrodes", *Optics Communications*, vol. 138, no. 1, pp. 151–157, 1997. [Online] (cited on p. 96).
7. Love, G. D., J. V. Major, and A. Purvis, "Liquid-crystal prisms for tip-tilt adaptive optics", *Opt. Lett.*, vol. 19, no. 15, pp. 1170–1172, 1994. [Online] (cited on p. 96).
8. Erturk, A. and D. J. Inman, *Piezoelectric energy harvesting*. John Wiley & Sons, 2011 (cited on p. 98).
9. Wilk, G. D., R. M. Wallace, and J. M. Anthony, "High- gate dielectrics: Current status and materials properties considerations", *Journal of Applied Physics*, vol. 89, no. 10, pp. 5243–5275, 2001. [Online] (cited on p. 99).
10. Gandhi, S., M. R. Pulugurtha, H. Sharma, P. Chakraborti, and R. R. Tummala, "High-k thin-film capacitors with conducting oxide electrodes on glass substrates for power-supply applications", *IEEE Transactions on Components, Packaging and Manufacturing Technology*, vol. PP, no. 99, pp. 1–6, 2016. [Online] (cited on p. 99).
11. Raj, P. M., D. Balaraman, I. R. Abothu, C. Yoon, N. K. Kang, *et al.*, "Integrating high-k ceramic thin film capacitors into organic substrates via low-cost solution processing", *IEEE Transactions on Components and Packaging Technologies*, vol. 30, no. 4, pp. 585–594, 2007. [Online] (cited on p. 99).

12. Renaud, M., K. Karakaya, T. Sterken, P. Fiorini, C. Van Hoof, *et al.*, "Fabrication, modelling and characterization of {mems} piezoelectric vibration harvesters", *Sensors and Actuators A: Physical*, vol. 145–146, pp. 380–386, 2008, Special Issue: Transducers/07 Eurosensors XXI, The 14th International Conference on Solid State Sensors, Actuators and Microsystems and the 21st European Conference on Solid-State TransducersThe 14th International Conference on Solid State Sensors, Actuators and Microsystems and the 21st European Conference on Solid-State Transducers. [Online] (cited on p. 99).

13. Cui, Q., C. Liu, and X. F. Zha, "Study on a piezoelectric micropump for the controlled drug delivery system", *Microfluidics and Nanofluidics*, vol. 3, no. 4, pp. 377–390, 2007. [Online] (cited on p. 99).

14. George, J. P., P. F. Smet, J. Botterman, V. Bliznuk, W. Woestenborghs, *et al.*, "Lanthanide-assisted deposition of strongly electro-optic pzt thin films on silicon: Toward integrated active nanophotonic devices", *ACS Applied Materials & Interfaces*, vol. 7, no. 24, pp. 13 350–13 359, 2015, PMID: 26043103. [Online] (cited on pp. 99, 101).

15. Zou, Q., H. Ruda, B. Yacobi, K. Saegusa, and M. Farrell, "Dielectric properties of lead zirconate titanate thin films deposited on metal foils", *Applied Physics Letters*, vol. 77, no. 7, pp. 1038–1040, 2000 (cited on p. 100).

16. Zhu, B., D. Li, Q. Zhou, J. Shi, and K. Shung, "Piezoelectric pzt thick films on lanio3 buffered stainless steel foils for flexible device applications", *Journal of physics D: Applied physics*, vol. 42, no. 2, p. 025 504, 2008 (cited on p. 100).

17. Seveno, R. and D. Averty, "Ultra light tunable capacitor based on pzt thin film deposited onto aluminium foil", *Journal of sol-gel science and technology*, vol. 68, no. 2, pp. 175–179, 2013 (cited on p. 100).

18. Walenza-Slabe, J. and B. Gibbons, "Processing of rf-sputtered lead zirconate titanate thin films on copper foil substrates", *Journal of Materials Science*, vol. 50, no. 19, pp. 6420–6426, 2015 (cited on p. 100).

19. Erturk, A. and D. J. Inman, "Appendix e: Numerical data for pzt-5a and pzt-5h piezoceramics", in *Piezoelectric Energy Harvesting*. John Wiley & Sons, 2011, pp. 373–374 (cited on p. 100).

20. Wu, D., Q. Zhou, K. K. Shung, S. N. Bharadwaja, D. Zhang, *et al.*, "Dielectric and piezoelectric properties of pzt composite thick films with variable solution to powder ratios", *Journal of the American Ceramic Society*, vol. 92, no. 6, pp. 1276–1279, 2009 (cited on p. 100).

21. Joo, H.-Y., H. J. Kim, S. J. Kim, and S. Y. Kim, "Spectrophotometric analysis of aluminum nitride thin films", *Journal of Vacuum Science & Technology A*, vol. 17, no. 3, pp. 862–870, 1999 (cited on pp. 101, 112).

22. Stoiber, R. E. and S. A. Morse, *Crystal identification with the polarizing microscope*. Springer Science & Business Media, 2012 (cited on p. 104).

23. Sørensen, B. E., "A revised michel-lévy interference colour chart based on first-principles calculations", *European Journal of Mineralogy*, vol. 25, no. 1, pp. 5–10, 2013 (cited on p. 104).

24. Lózar Muñoz, A. de, *Liquid crystal dynamics: Defects, walls and gels*. Cuvillier Verlag, 2005 (cited on p. 108).

25. Krishnamurthy, K. S., P. Tadapatri, and W. Weissflog, "Twist disclination loops in a bent-core nematic liquid crystal", *Soft Matter*, vol. 7, no. 13, pp. 6273–6284, 2011 (cited on p. 108).

26. Tamba, M.-G., W. Weissflog, A. Eremin, J. Heuer, and R. Stannarius, "Electro-optic characterization of a nematic phase formed by bent core mesogens", *The European Physical Journal E*, vol. 22, no. 1, pp. 85–95, 2007 (cited on p. 108).

27. **Willekens, O.**, J. P. George, K. Neyts, and J. Beeckman, "Ferroelectric thin films with liquid crystal for gradient index applications", *Opt. Express*, vol. 24, no. 8, pp. 8088–8096, 2016. [Online] (cited on p. 108).

28. Xiaoning, J., *Liquid crystal based optical phased-array beam steering*, 2015 (cited on pp. 115, 116).

5

Beam-focusing with high-κ materials

In the previous chapter the effects of adding a dielectric material with high relative permittivity on top of the addressing electrode layer in a beam-steering device were studied and the advantages of this technique highlighted. The beam-steering took place in a single plane, which makes simulating the director profile and visualising it a lot easier. Beam-steering in two dimensions can be easily achieved by placing two one-dimensional beam-steering devices in series, in such a way that the planes in which they steer are not parallel. It can also be achieved with a two-dimensional patterned electrode geometry.

In this chapter a beam-focusing device, similar to a lens, is fabricated and studied. The focal point of this liquid-crystal-based lens can be adjusted electronically, by tuning the voltages applied over a series of conductive and concentric arcs. Its lateral dimensions are comparable to those found in modern day camera modules for smartphones, but it is thinner and allows adjustment of the focal length, similar to real optical zoom lenses, which are far more voluminous. While tunable focal length liquid crystal lenses are nothing new (the first published work dates back to 1979 [1]), this particular design uses the high-κ material discussed in the previous chapter to smoothen the phase profile between the arc electrodes, thereby improving the focusing efficiency. Because the device is based on an optically-transparent, thin and non-conductive layer, it is of interest in the current socio-economic trend towards more energy efficient devices.

5.1 Lensing operation

So how does one go from one-dimensional steering to a two-dimensional lensing action? The way this is realized is by applying one modification to the

previous steering mechanisms: whereas in previous chapters the optical path length (OPL) changed *linearly* within each unit of a periodically repeating pattern, the OPL for a lens needs to change in a *parabolic* fashion. This ensures that the phase of an incident plane wave is parabolically varying across the plane where it emerges from the device, which is the same behaviour as that of a lens made of e.g. glass. An ordinary lens changes an incident planar wavefront to one that is parabolically varying by the curvature of its interfaces and the difference between its constant refractive index and that of the surrounding medium. It is possible to achieve the same effect then with a planar device that has a gradient in its refractive index, a GRIN lens.

Spatial light modulators (SLMs) are a class of devices in which a rectangular grid of closely spaced pixel electrodes allows an incident wave front to be reshaped: each electrode is capable of switching the liquid crystal layer on top of it[*], thereby changing the retardation the wavefront experiences over that electrode or pixel. Modern SLMs feature a grid of 1000×1000 pixels or more. If in such a grid all pixels that are at the same distance from a reference pixel are held at the same electric potential, the square grid is divided into a series of concentric circle-like electrodes. The close spacing between the electrodes allows a very accurate form of phase control, which means that an SLM could be used to realize the lensing functionality. For consumer applications, the high degree of freedom available with an SLM is an inefficient use of resources. Application specific integrated circuits (ASICs) are more cost-effective. For LC-based lensing, a series of concentric electrodes is at the heart of the ASIC, with more electrodes allowing a better control over the phase front. A large amount of electrodes comes at the cost of complexity. When a limited number of circular electrodes is used, the total active area would be quite small though, unless the interelectrode spacing is increased. A too large spacing will degrade the performance rapidly, because the electric field is usually localised to the electrodes, as we have seen in figure 4.1. In that same figure, it was also shown that a layer of a high-κ material covering the electrodes could alleviate this problem and that is where PZT comes in.

Because of the non-linear response of nematic LCs to an applied voltage, the choice of the voltages that need to be applied to the limited number of electrodes is not straightforward: a sampling of a parabolic voltage profile

[*]There are SLMs that do not rely on liquid crystals, instead using deformable mirrors. The principle of operation is similar for both classes of SLMs.

does not automatically lead to a parabolic refractive index profile. The initial choice of voltages can be obtained by using a reverse index lookup: given the desired refractive index over an electrode, determine the voltage that is needed to obtain that index. This process is illustrated in figure 5.1. The desired index profile of two lens designs is shown in the graph to the left. The strong curvature parabola represents the index profile of a lens that has a shorter focal length than the other parabola. The profiles are sampled at eight equidistant points, that correspond to the different radii of the circular electrodes. At these locations, the desired average refractive index, defined in equation (4.3), can then be mapped to the required voltages by using the graph to the right. This graph shows the average refractive index versus the voltage in a parallel-electrode configuration, which is a well-known graph that can be easily calculated upfront given the LC material properties and the alignment layer properties. Noticeable in figure 5.1 to the right, are two well-known features of nematic LCs in a vertical field switching (VFS) configuration: the curve shows the presence of a threshold at low voltages, the Fréedericksz transition threshold below which the index is approximately equal to n_e, and $\langle n \rangle$ approaches n_o as the voltage is increased.

The focal length, f, of a GRIN LC lens is given by [2, chapter 6.4]:

$$f \approx \frac{R^2}{2\Delta n d}, \tag{5.1}$$

where d is the LC layer thickness and Δn is the difference between the average refractive index at the center of the lens and that index at the edge of the lens, a distance R away from the center. Using this equation, we can estimate that the smallest focal length achievable with a 55.7 µm diameter lens made using the liquid crystal E7 and having an LC layer thickness of 5.5 µm is 3.34 cm. That number is an absolute lower bound, because an average refractive index equal to n_o is not achievable in practice, as figure 5.1 hints at.

5.2 The liquid crystal lens: a macroscopic view

The proposed liquid crystal lens design is shown schematically in figure 5.2. The masks used for the fabrication of the addressing electrodes are shown in figure 2.10c: the addressing electrodes are not perfect concentric circles, but concentric arcs, because a wedge-like area is reserved for contacting

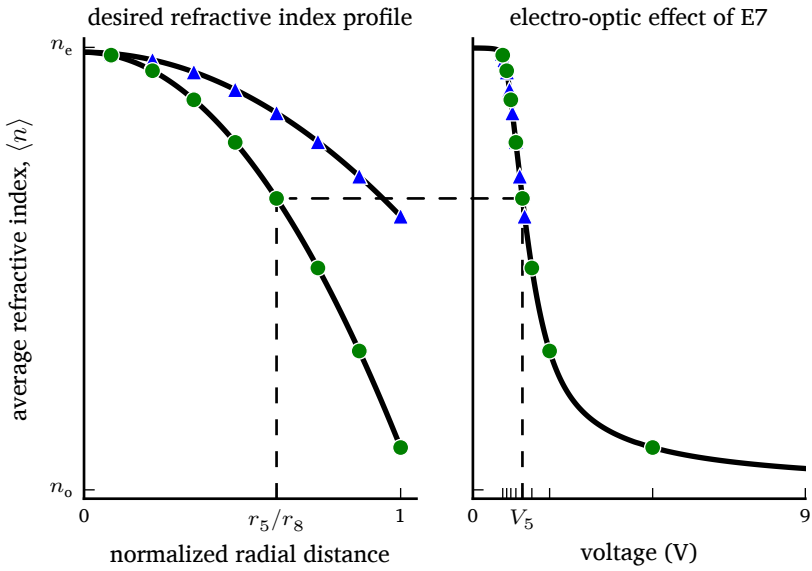

Fig. 5.1: Determining the voltages required for a parabolic index profile in a multi-electrode LC cell happens through a reverse index lookup: at a certain distance from the center of the lens the desired index profile is sampled (left graph). This index value is then mapped onto its corresponding voltage through the curve that displays the electro-optic effect of the liquid crystal in a planar parallel-electrode cell (right graph).

the inner electrodes. This could be avoided by using at least two planes for the addressing electrodes: one plane that holds full concentric circles, and another where the feed lines are in. A conductive path between the electrodes in these two planes can then be made using vias. Such processing is more involved than the simple single-plane electrodes that are proposed here and the presence of the wedge should not have too big of an impact, as long as the interelectrode spacing is large. The figure shows that a polyimide (PI) alignment layer is proposed, which needs to be rubbed. Photoalignment would be a useful alternative. Because the design is quasi-centrosymmetric, the rubbing direction is only of importance to determine the orientation of the polarization axis for light that is incident on the lens. Note that while the ground electrode (upper ITO layer) needs to be made of a transparent conductive material, the addressing electrodes don't necessarily have to: due to the spacing between the addressing electrodes and the optical transparency of the PZT layer, a large amount of light can still be transmitted.

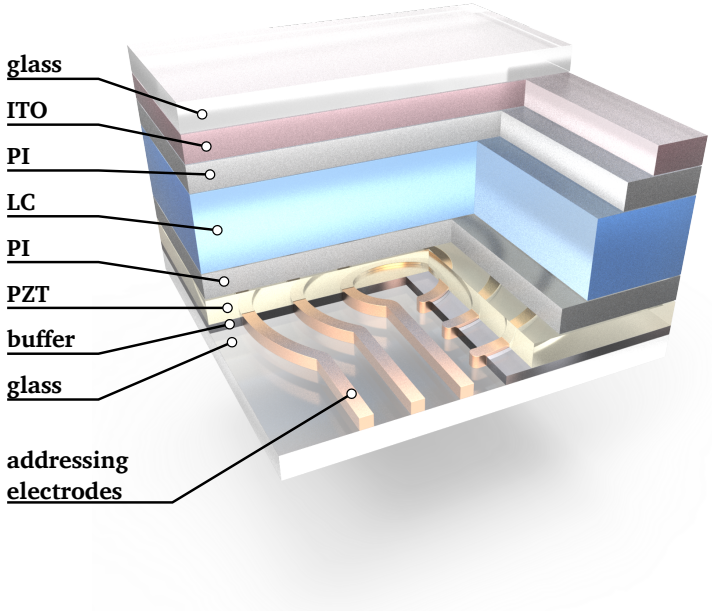

Fig. 5.2: Cutaway diagram of the proposed multi-electrode LC lens. Layer thicknesses are not to scale.

Using the electrode mask of figure 2.10c, several of these LC lenses have been fabricated in a cleanroom environment, including reference devices that lack the PZT layer, which allows comparing the performance between the reference devices and the PZT-enhanced devices. Examples of some of the fabricated electrode patterns are shown in figure 5.3. The electrodes are made of a non-transparent conductive material using the image reversal technique described in section 2.3.3. These photographs also illustrate that the size of the wedge can be made fairly small relative to the overall size of the lens. A photograph of the fully assembled and externally contacted devices is shown in figure 5.4.

Figure 5.4 shows that the device has a slightly reddish color. The transmission spectrum of the fully assembled device, measured at a location free from the opaque conductors, is shown in figure 5.5. It illustrates that there is a slightly higher transmission at a few wavelengths, one of which is associated with red colors (615 nm). The transmission fluctuations can be attributed to the thickness of the PZT layer, as explained in section 4.2.1.B. The relative transmission of the device lies between 63 % and 83 % in the wavelength

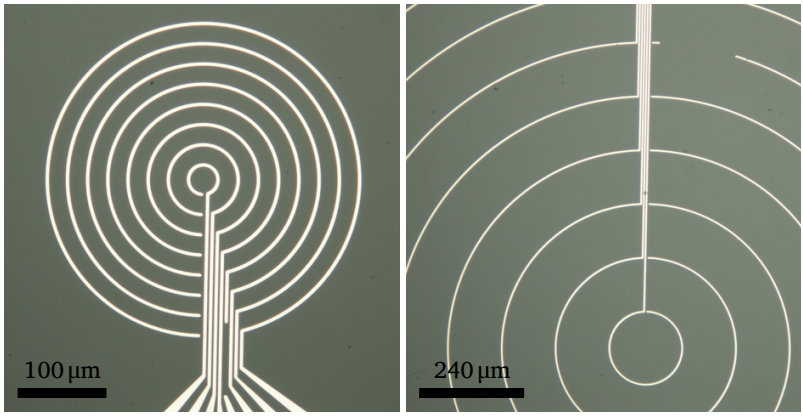

(a) (b)

Fig. 5.3: Electrode patterns after lift-off. Various interelectrode spacings have been used, the ones shown here are $\Delta r = 20\,\mu\text{m}$ (a) and $\Delta r = 120\,\mu\text{m}$ (b). Note the defects in these patterns: some electrode patches are "floating" (not connected to the outer addressing lines), which is a problem that got solved after changing the processing parameters, as described in section 2.3.3.

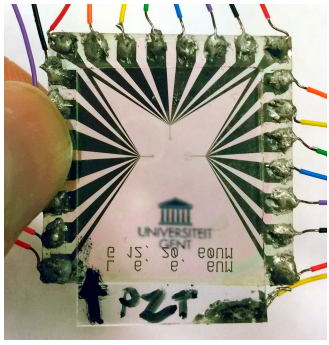

Fig. 5.4: Photo of an assembled LC lens design. The university logo, printed on a piece of paper, is visible through the stack, which illustrates the optical transparency of the PZT layer. The rubbing direction on the upper substrate is indicated with an arrow.

region that is not influenced by the absorption of ITO in the UV region.

5.3 Microscope metrology

Insight into the device's actual performance is given by studying the device using polarized light microscopy. Two studies are presented: a comparison of

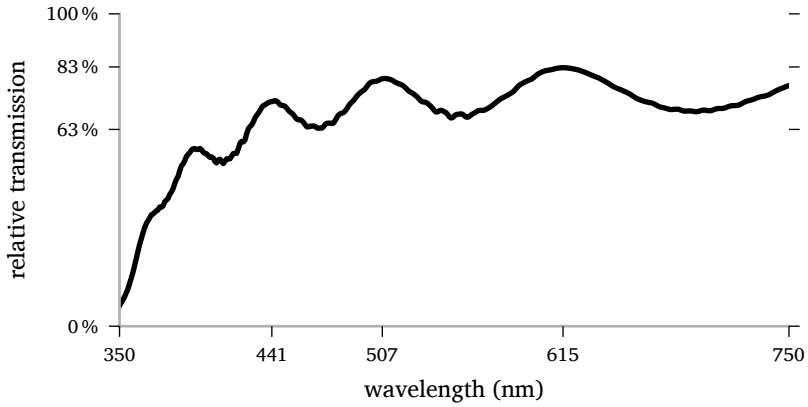

Fig. 5.5: Measured transmission spectrum of the assembled lens device, which uses two Corning® glasses as substrates. The transmission spectrum of an ITO-coated substrate is shown in figure 4.4. The transmission is expressed relative to the spectrum of the used light source.

the retardation profiles of the reference and PZT-enhanced device and a study of the wavefront shape when a specific set of voltages is applied to the lens device.

5.3.1 Comparison of retardation profiles

Figures 5.6a and 5.6b show micrographs of the reference lens and PZT-enhanced lens respectively, where both feature a 60 µm interelectrode distance. Each device is held between crossed polarizers, the transmission axes of which are indicated by the symbol in the top-left corner, and rotated such that the alignment axis (indicated by the rubbing arrow) is at an angle of approximately 45° with respect to either polarizer axis. The LC cells are illuminated by the light from a series of green LEDs ($\lambda_c = 520\,\text{nm}$, $\Delta\lambda_{\text{FWHM}} = 34\,\text{nm}$), which due to their quasi-monochromatic nature simplify the following image analysis. Light is transmitted through the cell, except at the addressing electrodes due to their opacity, which allows us to easily distinguish their locations. All addressing electrodes are held at the same electric potential relative to the ground, which is 2.0 V in both pictures. The bottom right corner of figure 5.6b shows the same area of the PZT-enhanced device using the same imaging conditions, such as exposure time and gain, but with the electrodes at 0.1 V.

In the picture of the reference device, one can clearly see a large intensity variation close to the electrode edges. This is due to the reorientation of

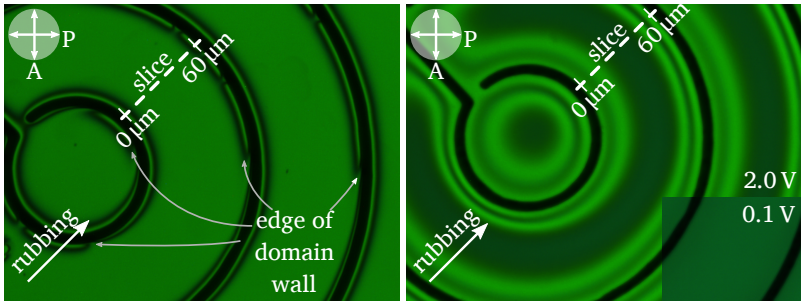

(a) (b)

Fig. 5.6: Micrographs of a reference device (left) and a device with electrodes covered by a 0.84 µm thick PZT layer (right). The devices are illuminated from the backside, placed between crossed polarizers and observed using a 20X microscope objective. The electrodes (black lines) are 6 µm wide and spaced 60 µm apart; a 1 kHz square wave is connected to the electrodes forming a potential difference of 2.0 V between the circular electrodes and the common electrode. The bottom right corner of the PZT-enhanced device shows the situation for the same lens when the amplitude is 0.1 V.

the liquid crystal director that aligns along the electric field lines. This reorientation leads to a change in the polarization of transmitted light, which results in a change in the amount of light that passes through the analyzer. In the PZT-enhanced device the region where the director reorients is much wider, indicating that the PZT layer has spread the electric potential further away from the electrodes, as expected from the previous chapter. How far it spreads the electric field can be estimated from the intensity variations halfway between two neighboring electrodes: for the reference device no intensity variation is discernible there, but the PZT-enhanced lens shows a small decrease in intensity, which is apparent from the small overlay in the lower right corner. The addition of the PZT layer increases the voltage drop over the LC halfway between two neighboring electrodes, making it larger than the threshold voltage of a parallel planar electrode LC cell with the same LC layer thickness, so that the liquid crystal starts to reorient locally.

Interesting to note is that in the reference device domain walls are apparent. The reason for their appearance is the presence of strong in-plane fringe fields which tilt the LC in a direction opposite to the one imposed by the pretilt [3]. The appearance of a domain wall has been simulated as well in the previous chapter, where figure 4.10 shows the simulated director profiles

along the slices indicated in figures 5.6a and 5.6b. The domain walls collapse into disclination lines at higher voltages (∼7.8 V, see Visualization 1 of [4]). No domain walls are visible in the PZT-enhanced device though, as with the simulations, which demonstrates the ability to reduce fringe fields in the liquid crystal layer near electrodes.

The orientation of the director in this three-dimensional device is complex. Insight is provided using figure 5.7, in which the same devices are now imaged with the rubbing direction parallel to one of the polarizers. Where the director is perfectly aligned with the transmission axis of either of the polarizers, the image should be perfectly dark. This is the case for the large black areas between the electrodes. Close to the electrodes a distinction needs to be made between two regions. A conic section labelled with a boldfaced letter "A" is marked in each of the micrographs. Here, the intensity of the transmitted light close to the electrodes is smaller than elsewhere in the figure, which indicates the director is better aligned with the polarizer's transmission axis. The radially directed electric field lines are here to a good degree parallel to the alignment direction imposed by the rubbing. This is less pronounced for the PZT-enhanced lens device and it is believed this is due to the smoothing effect of the PZT layer, which acts more like a blur filter. In the region labelled with a boldfaced letter "B", there is a large mismatch between the radial field lines and the rubbing direction. This leads to a twist of the director that is

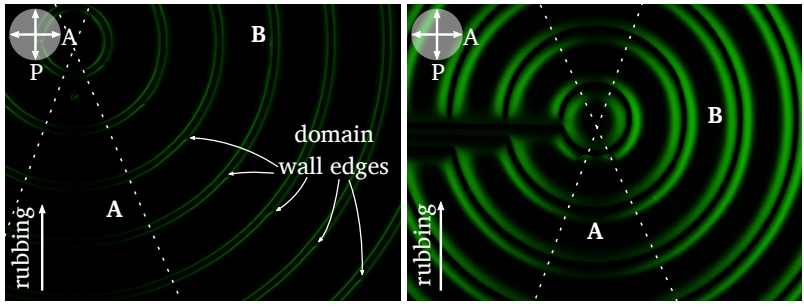

(a) (b)

Fig. 5.7: Micrographs of the same devices from figure 5.6, but with the rubbing axis aligned with one of the polarizers' transmission axis. To the left is again the reference device, to the right the PZT-enhanced device. The potential difference between the concentric addressing electrodes and the homogeneous ground is 4.0 V. Compared to figure 5.6, a larger part of the images is shown, to allow easier observation of the patterns.

more pronounced close to the electrode.

A study of the transmitted light intensity as a function of the applied voltage of the devices is instructive to understand the retardation, which is related to the orientation of the director. To this end, the radial intensity profile for the devices that feature an interelectrode distance of 60 µm is extracted along the slices indicated in figures 5.6a and 5.6b. This procedure is repeated for a range of voltages, going from 0 V to 10 V in steps of 0.1 V, that are applied between the addressing electrodes and the homogeneous ground. These radial intensity slices are shown in figure 5.8. The slices are taken along the rubbing direction between two neighboring addressing electrodes.

This sweep of the electric potential shows that the voltage for which switching starts to occur near the electrodes is hardly affected by the thin layer of PZT, but that the electrode voltage required to tilt the director halfway between the electrodes is much lower compared to the reference device. It also shows that at 4 V, the voltage at which the micrographs in figure 5.7 are taken, the retardation has changed halfway between the addressing electrodes. Combining this piece of information with the darkness between two electrodes shown in figure 5.7b, indicates that the director there is tilted and that there is little to no in-plane twist.

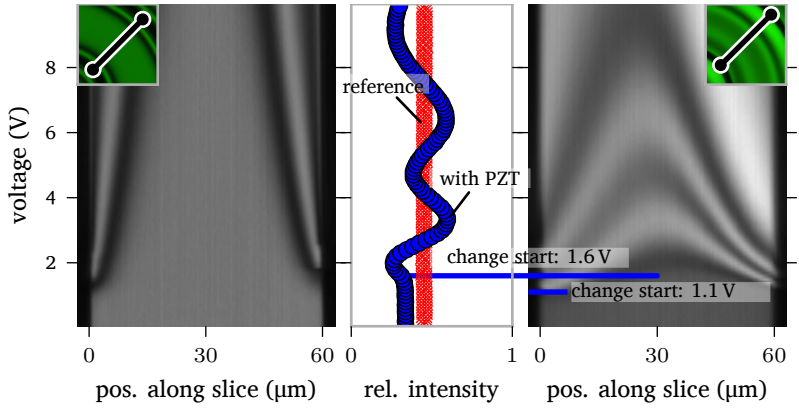

Fig. 5.8: The intensity profile along the slices indicated in figure 5.6, shown when different voltages are applied between the homogeneous ground and the addressing electrodes. The intensity variations are related to the orientation of the director. When PZT is applied over the electrodes, even halfway between two electrodes the director is affected by the potentials applied to the addressing electrodes, which are shown as the black stripes at the sides in the left and right graphs.

The imageset shown in figure 5.8 also indicates that a PZT layer thickness of 0.84 µm over electrodes that are spaced 60 µm apart, is insufficient to induce a quasi-homogeneous director tilt in a 5.5 µm thick LC layer. The ability of the PZT layer to "smear" the electric field laterally between two electrodes to obtain a quasi-homogeneous electric field distribution over the LC layer is therefor limited, a limitation that was already discussed in the previous chapter, together with ways to counter it.

5.3.2 Phase interferometry

To measure the phase of the wavefront as it emerges from the lens, the lens is inserted in the sample arm of the Mach–Zehnder interferometer that is part of a microscope system of the Brussels Photonics Team (B-Phot) of the Vrije Universiteit Brussel. From such a phase measurement, the focal length can be determined. The setup also allows to determine the wave aberrations of lenses.

The set of voltages labelled as "strong" in figure 5.9 is applied to the addressing electrodes. This particular set of voltages was determined in an earlier stage to result in an intensely focussed spot at a distance of approximately 4.4 cm away from the lens. The results from the interferometric phase measurements using this voltage profile are shown in figure 5.10. In figure 5.10a, the wrapped and normalized phase is shown, which is the direct result of applying inverse geonometric functions to the formula that describes the interference of two waves of the same frequency but with a phase difference

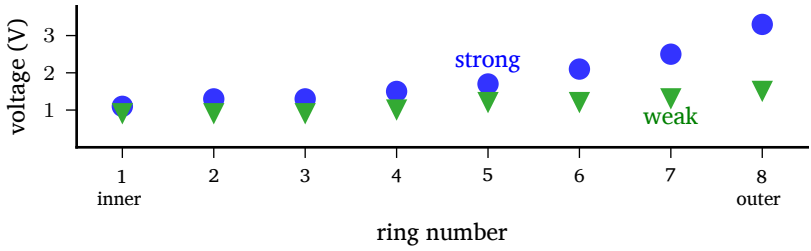

Fig. 5.9: Graphical depiction of a set of voltages that lead to intense spots a distance 4.4 cm away from the lens (the "strong" profile) and a distance 7.4 cm away from the lens (the "weak" profile). The weak profile is quasi-linear, because the linear regime of the electro-optic behaviour of E7 is used (see figure 5.1, to the right), whereas the stronger profile is more non-linear as it covers a larger interval of the obtainable average refractive index.

of ϕ [5, chapter 2]:

$$I = I_1 + I_2 + 2\sqrt{I_1 I_2}\cos\phi, \tag{5.2}$$

in which I_1 and I_2 are the intensities of the waves in the different arms of the Mach–Zehnder interferometer. The software associated with the Mach–Zehnder microscope setup (PSI 5.3 (16)) solves the problem of the limited range of the arccos function (which is between 0 and π), by adding a series of retardation plates with known retardation in the path of one of the Mach–Zehnder arms, which is how it can visualize the phase for an entire 2π modulation. The two-dimensional graph of figure 5.10a shows that between two electrodes the phase varies continuously, because the optical path length varies continuously, but the locations of the electrodes are easily distinguished due to non-continuous jumps in the phase profile. This is likely the result of the opacity of the electrodes. In figure 5.10b, the unwrapped phase is shown. The process of unwrapping the phase continuously in two dimensions apparently leads to some non-sensical data, which is masked red in these graphs. It is clear that the pixels where the phase is not clearly defined are more often located at the positions of the electrodes.

The unwrapped phase profile of figure 5.10b, can be decomposed into a set of Zernike polynomials, which are orthogonal polynomials that are defined on the unit disk and are commonly used in adaptive optics and optical manufacturing where circular pupils are used, as they relate to optical aberrations in such systems [6, 7]. The sum of the Zernike polynomials into which the phase profile has been decomposed then approximates the measured wave front as close as possible, the approximation improving as more terms are added. The lower order Zernike polynomials describe the more common optical aberrations, the “defocus” being the most important to describe a parabolic wave front profile. The coefficient belonging to this polynomial, $Z_2^0(r,\phi)$, can be used to derive the focal length of a parabolically curved phase profile [8]. Figure 5.11 shows the wave front reconstructed from figure 5.10b using the Zernike polynomials. It should be noted that repeated measurements of this phase profile did not result in reproducible results. Over several measurements the masked pixels change, though they are still often found close to the electrodes. The new pixel mask affects the results of the decomposing algorithm, which sometimes reported positive values for the defocus, sometimes negative values. We therefor decided not

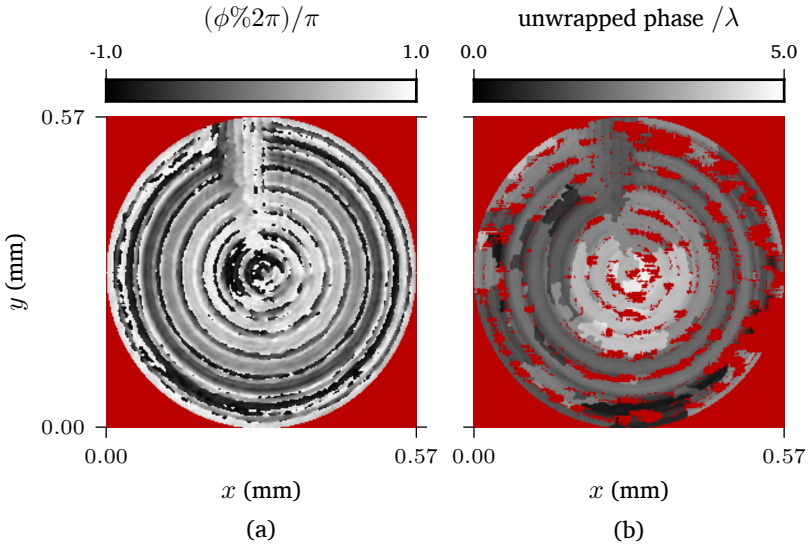

Fig. 5.10: Measured phase of a laser beam ($\lambda = 633\,\text{nm}$) passing through a PZT-enhanced lens with 30 µm interelectrode distance. (a) Reconstruction of the wrapped phase from the observed interference pattern. (b) Two-dimensional unwrapping of the phase. A circular aperture is applied over the micrographs, red pixels denote areas where the phase is either not measured or undefined.

to rely on the calculated values, but have included the measured phase front (figure 5.10) and one linear combination of Zernike polynomials (figure 5.11) for clarity. An alternative technique to quantize the performance of these lens-like devices will be discussed next.

5.4 Direct measurement of the focal length

If the liquid crystal device functions as a lens, the focal length can be derived from measuring the distance between the lens and a focussed spot when the lens is illuminated by a collimated beam. An experimental setup is built to do exactly that. In this experiment a collimated laser beam ($\lambda = 633\,\text{nm}$) is passed through a spatial filter and expanded so that the beam waist is an order of magnitude larger than the lens diameter, thereby ensuring the beam intensity over the lens is approximately constant so that any observed intensity deviations must be due to the device operation. The laser light is

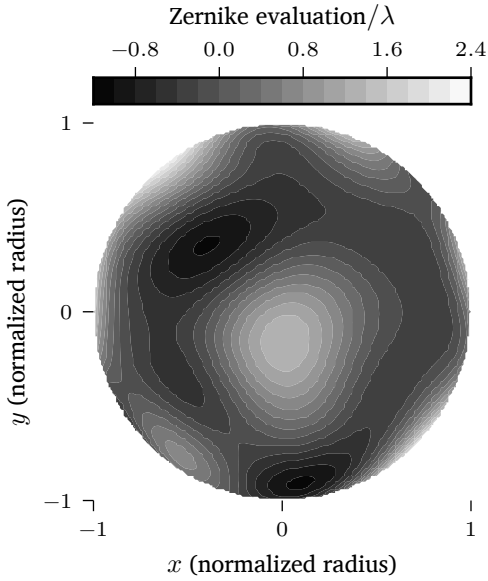

Fig. 5.11: Reconstructed wave front exiting from the PZT-enhanced lens, using the 15 lowest order Zernike polynomials.

also polarized along the rubbing direction prior to incidence on the lens and passes through another polarizer, of which the transmission axis is parallel to the former, prior to impinging on the camera sensor.

Figure 5.12a shows a micrograph of a lens featuring 6 µm wide platinum electrodes and 30 µm interelectrode distance. All electrodes are grounded, so the LC director is aligned in-plane and along the rubbing direction, which is perpendicular to the array of closely spaced addressing electrodes that lead to the lens. In figure 5.12b the focal plane of the camera is 4.4 cm away from the lens, by moving the camera along the optical axis. With still no voltages applied, the camera sensor captures the background illumination from the laser. A small dark spot is observed at the center as well as a darker rectangular area where the feed lines are. These are believed to be caused by the diffraction at the opaque electrodes. The series of voltages labelled as “strong” in figure 5.9 is now applied to the electrodes and the micrograph changes to figure 5.12c. In it, an intense bright spot is observed, which is surrounded by a region that is much darker and about the same size as the lens shown in figure 5.12a. Moving the camera another 3 cm along the optical path and grounding the electrodes again, the image shown in figure 5.12d

is observed. Applying the "weak" set of voltages shown in figure 5.9 to the addressing electrodes now changes the view of this focal plane to figure 5.12e. Once again an intense bright region is shown surrounded by a darker area. The size of the spot is larger than the one in figure 5.12c, which is to be expected when a lens with larger focal length, but same aperture, is used.

These pictures indicate that most of the light is redirected to the focal spot, which means that there is indeed a fairly smooth director variation between the addressing electrodes that are spaced 30 µm apart here. This gradual variation is made possible by the presence of the PZT layer. Some of the aberrations visible in figures 5.12b to 5.12e are due to the use of non-transparent metallic electrodes. This might be overcome by using a transparent conductor such as ITO or reduced by making the electrodes less wide than the current 6 µm.

A quantitative description of the intensity profile of figure 5.12c is obtained by radially integrating the pixel intensity values, using the center of mass as the origin for the radial integration method. This radial intensity profile is visualized in figure 5.13 and shows that the central spot is about 21 times more intense than its surroundings and almost 5 times more intense than the background illumination.

The spot profile shown in figure 5.13 can now be compared to that of a similar-sized and diffraction-limited lens. An ideal lens will focus a laser beam down to a spot known as the Airy disc, which together with the lower-intensity concentric rings around it form the Airy pattern. The full width at half maximum (FWHM) of this diffraction limited spot is given by $D_{\text{FWHM}} = 1.02\lambda f/d$ with f the focal length of the lens and d the diameter of the focusing lens or its aperture stop in case one is present. For an ideal lens with a focal length of $f = 4.4$ cm and a diameter of $d = 557$ µm, this would result in a FWHM of the Airy disc of 51 µm. The diameter in this comparison is chosen to be equal to the largest outer diameter of the set of concentric ring-shaped electrodes of the liquid crystal lens. In reality a small region around the electrodes still contributes towards the lensing operation, so the chosen diameter is slightly underestimated, as well as the FWHM of the diffraction limited spot. The FWHM of the focused spot shown in figure 5.13 is measured to be 72 µm, about 41 % larger than that of the theoretical ideal.

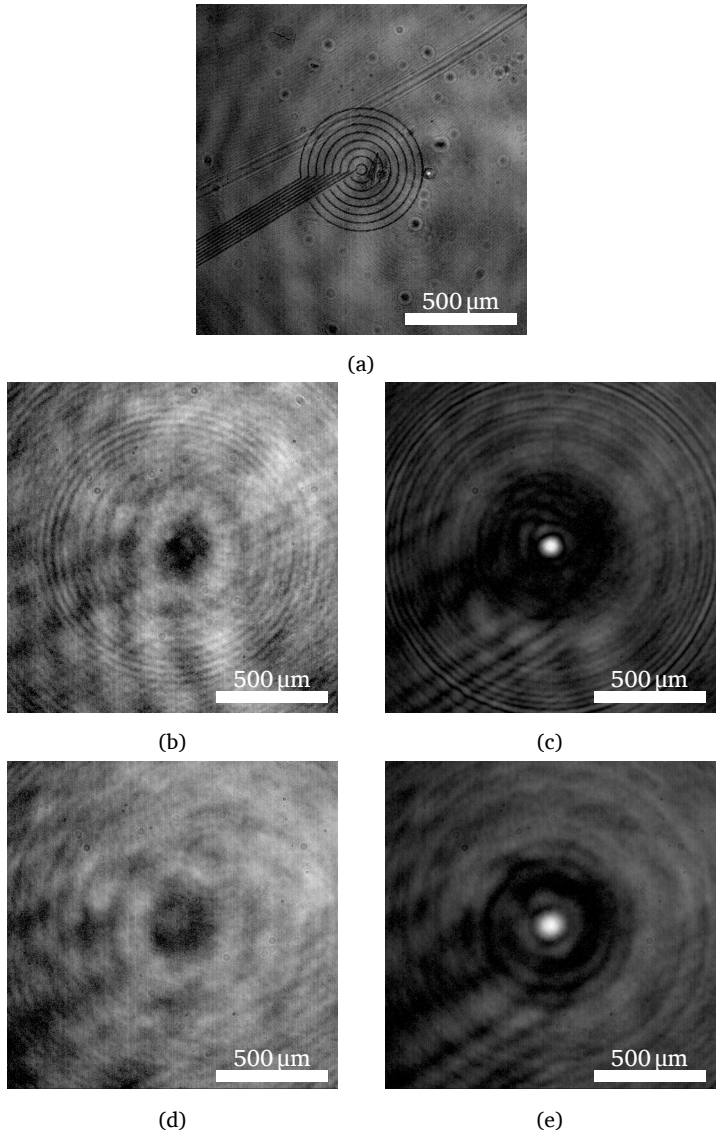

Fig. 5.12: Micrographs of (a) the PZT covered electrode pattern on the LC lens, (b) a plane a distance of 4.4 cm away from the lens with the electrodes all grounded, (c) a plane at the same distance as (b) but with voltages applied from the "strong" profile of figure 5.9, (d) a plane at a distance of 7.4 cm from the lens and (e) the same plane as in (d), but using the set of "weak" voltages from figure 5.9.

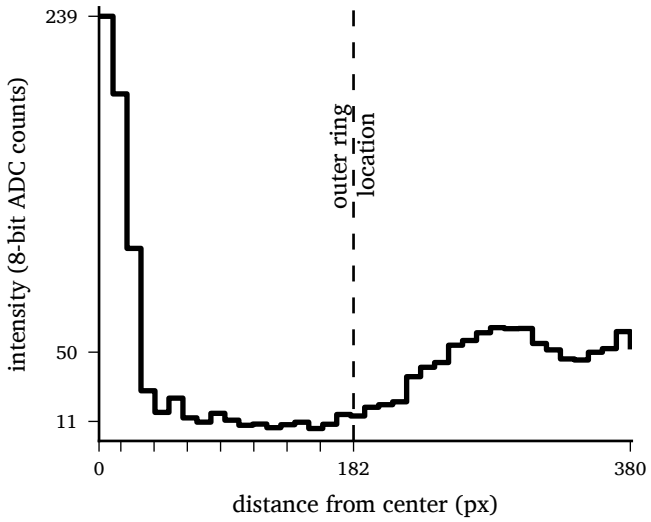

Fig. 5.13: Intensity profile radially integrated around the center of mass in figure 5.12c. The unlabelled ticks mark the locations of the electrodes in figure 5.12a.

5.5 Summary

This chapter continued exploring the benefits of high-κ materials in multi-electrode liquid crystal devices. Using the PZT that is prepared at the university's cleanroom facilities, a liquid crystal director profile is obtained in which the director tilt is more easily affected further away from a series of widely spaced electrodes. This allowed us to construct a lens-like device where a series of concentric electrodes is responsible for tilting the director in order to obtain a quasi-parabolic optical path length profile, similar to an actual lens. Two advantages of this technique are the reduction of the amount of addressing electrodes needed to switch the LC, as well as keeping energy consumption low due to PZT's dielectric nature.

Using one of the fabricated lens devices featuring eight concentric addressing electrodes that are spaced 30 µm apart, the electric tunability of the focal length of this class of devices was demonstrated: a collimated laser beam was focussed to a small spot 4.4 cm away from the lens using one set of voltages and was refocussed to a position 7.4 cm away from the lens by applying a different set of voltages. This variable focus property is of interest to handheld devices like smartphone lenses and in medical tools such as endoscopes.

5.6 References

1. Sato, S., "Liquid-crystal lens-cells with variable focal length", *Japanese Journal of Applied Physics*, vol. 18, no. 9, p. 1679, 1979 (cited on p. 121).
2. Hecht, E., *Optics*, 4th. Addison Wesley, 2002 (cited on p. 123).
3. Vanbrabant, P. J., J. Beeckman, K. Neyts, E. Willman, and F. A. Fernandez, "Diffraction and fringing field effects in small pixel liquid crystal devices with homeotropic alignment", *Journal of Applied Physics*, vol. 108, no. 8, p. 083 104, 2010 (cited on p. 128).
4. **Willekens, O.**, J. P. George, K. Neyts, and J. Beeckman, "Ferroelectric thin films with liquid crystal for gradient index applications", *Opt. Express*, vol. 24, no. 8, pp. 8088–8096, 2016. [Online] (cited on p. 129).
5. Saleh, B. E. and M. C. Teich, *Fundamentals of photonics*. John Wiley & Sons, 2007 (cited on p. 132).
6. Goodwin, E. P. and J. C. Wyant, "Field guide to interferometric optical testing", SPIE, 2006 (cited on p. 132).
7. Lakshminarayanan, V. and A. Fleck, "Zernike polynomials: A guide", *Journal of Modern Optics*, vol. 58, no. 7, pp. 545–561, 2011 (cited on p. 132).
8. Neal, D. R., R. J. Copland, D. A. Neal, D. M. Topa, and P. Riera, "Measurement of lens focal length using multicurvature analysis of shack-hartmann wavefront data", in *Optical Science and Technology, the SPIE 49th Annual Meeting*, International Society for Optics and Photonics, 2004, pp. 243–255 (cited on p. 132).

6

Conclusions and Outlook

6.1 Conclusions

Liquid crystals are fascinating materials and their applications cover a whole range of interesting and useful devices. In the work presented in this thesis, three liquid crystal devices are studied: two devices allow light to be deflected over small angles, the third can focus a beam of light to a narrow spot and the focal length can be changed electrically. The former two are categorized as variable blaze beam-steering devices, while the latter is known as a variable focal length liquid crystal lens.

New technologies, such as photoalignment, were used in the fabrication of these liquid crystal beam-steerers and lenses. They show that there is "plenty of room at the bottom" to improve current liquid crystal technologies and increase the application potential of liquid crystals. Non-contact liquid crystal alignment technology is of particular interest to microstructured substrates and sensitive electronics.

The angular steering range of liquid crystal (LC)-based technologies can be easily doubled by working in reflection, as discussed in chapter 3. The possibility of using liquid crystals to selectively switch between tunable angular deflection or total internal reflection could open up new applications.

Two particular technologies stand out in this thesis. The first is the use of hot-embossed microstructured substrates, which provides an interesting route for upscaling industrial processing, because the substrates can be easily replicated using soft-embossing and do not require complicated photolithography, nor complex electric addressing. Second, the introduction of materials with a high dielectric permittivity into liquid crystal multi-electrode devices is a very interesting development: in this thesis, visual examples are given

that illustrate the improvement of the director profile by adding a thin layer of lead zirconate titanate (PZT) on top of widely spaced electrodes. Because of it, the electric field distribution is smoothened between these electrodes, which leads to a more gradual change in the director tilt. This illustrates that these high-κ materials could be used in certain liquid crystal applications as a replacement for transparent conductive oxides, such as the commonly used indium tin oxide (ITO). The addressing electrodes used in the LC lens of chapter 5 are 6 µm wide, but their widths could be reduced to sub-micron sizes, while maintaining a relatively large area over them where the electric potential is quasi-constant. Better conductors than ITO could be used to make such small electrodes. The four guidelines to improve the electric field distribution when high-κ materials can be used, formulated in chapter 4, can be used when designing these next-generation electro-optical devices.

6.2 Future work

Throughout the design and manufacturing of the liquid crystal devices, a number of improvement opportunities arose. Some were acted upon, like using the available space on electrode masks more efficiently, while others have not been (fully) explored.

For starters, the devices demonstrated in this thesis use a nematic liquid crystal to introduce a gradient in the retardation of light. Because of this material choice, the devices are inherently polarization dependent. The recently developed polymer stabilized blue phase [1], a mesophase existing between the isotropic and chiral nematic phase, is an interesting alternative to tackle the polarization dependence problem, provided the voltages required for switching the blue phase can be further reduced. I had the opportunity to work several times during my thesis with blue phases [2–4], and was interested in using it for the lenses. Because the average refractive index as a function of applied voltage for a blue phase planar LC cell is very different from that of nematics, the phase profile resulting from using blue phase in a liquid crystal multi-electrode lens should be examined.

This leads me to a second point where I believe future work is required: examination of the phase profile. I have regretted not being able to characterize the image formation possibilities of the fabricated tunable LC lens. Measurement of the phase profile using the interferometric setup from B-Phot

would be very useful in this characterization. As shown in section 5.3.2, the measurement result was not ideal and estimation of the focal length was incorrect. Two approaches could be undertaken to solve this. The lens shown in chapter 5 could be fabricated again, this time using only transparent electrodes, which would allow light to pass through the lens at all positions and thus enable a more complete reading on the phase, which might lead to a better estimation of the focal length. The alternative approach would be to reduce the width of the electrodes to achieve a similar effect.

The electrode width in many of the masks that I have designed was chosen to be 6 µm, which leaves a safety margin for the lithography processing. This seemed necessary at first, because the processed samples from many lithography rounds using the Micro Controle MG1410 mask aligner from SET showed many failures on patterns with a minimum feature size of about 2 µm. At a later stage, the Karl Suss MA6 mask aligner was used, which resulted nearly always in perfectly patterned substrates, using the same mask. The resist materials were the same in both lithography paths, processing parameters were modified but not in the same extent as the modifications made in the optimization rounds using the MG1410.

Finally, one of the lensing masks I designed features a series of “floating electrodes”, electrodes that are not connected to any other. Researchers from Kent State University have demonstrated that floating electrodes in a layer that is vertically offset from the addressing electrode layer improves the potential profile across the liquid crystal lens aperture [5]. The fabrication of electrodes in multiple layers is challenging. In the mask I have designed, the floating electrodes are in the same layer as the addressing electrodes. The combination of PZT with these floating electrodes could provide an interesting research track to obtain an even smoother electrical field gradient, but I did not get around to doing it.

Tempus fugit.

6.3 References

1. Kikuchi, H., M. Yokota, Y. Hisakado, H. Yang, and T. Kajiyama, "Polymer-stabilized liquid crystal blue phases", *Nature materials*, vol. 1, no. 1, pp. 64–68, 2002 (cited on p. 140).
2. Joshi, P., J. De Smet, X. Shang, **Willekens, O.**, D. Cuypers, *et al.*, "Long term stability of polymer stabilized blue phase liquid crystals", *Journal of Display Technology*, vol. 11, no. 9, pp. 703–708, 2015 (cited on p. 140).
3. **Willekens, O.**, J. Beeckman, and K. Neyts, "Electrically tunable and polarization independent liquid crystal lens", in *14th FEA PhD Symposium*, 2013 (cited on p. 140).
4. Claus, H., **Willekens, O.**, O. Chojnowska, R. Dąbrowski, J. Beeckman, *et al.*, "Inducing monodomain blue phase liquid crystals by long-lasting voltage application during temperature variation", *Liquid Crystals*, vol. 43, no. 5, pp. 688–693, 2016 (cited on p. 140).
5. Li, L., D. Bryant, T. V. Heugten, and P. J. Bos, "Near-diffraction-limited and low-haze electro-optical tunable liquid crystal lens with floating electrodes", *Opt. Express*, vol. 21, no. 7, pp. 8371–8381, 2013. [Online] (cited on p. 141).

A

Appendix A

In section 3.1, the angle at which light emerges from the transmissive liquid crystal blazed grating is calculated using Snell's law and some geometrical considerations. The angle of incidence is assumed positive and the ray is incident on the device from the upper right quadrant of the figure.

The ray could also be incident from the upper left quadrant, as shown in figure A.1. Assuming all indicated angles are once again positive in value, the angle at which light emerges is given by a different formula than equation (3.3).

The geometrical considerations that lead to the emergence angle are:

$$\begin{aligned} &\text{In } \triangle ADB: && (\pi/2 - \delta_1 - \alpha) + \beta = \pi/2 && \Leftrightarrow && \delta_1 = -\alpha + \beta \\ &\text{In } \triangle BCE: && (\pi/2 - \gamma) + \delta_2 + (\pi/2 + \alpha) = \pi && \Leftrightarrow && \gamma = \delta_2 - \alpha \end{aligned}$$

In comparison to equation (3.1), the only difference is that α has obtained a minus sign. Equation (3.3) for the emergence angle therefor becomes:

$$\theta_o = \arcsin\left[\frac{n_2}{n_3}\sin\left(\arcsin\left\{\frac{n_1}{n_2}\sin\left[-\alpha + \arcsin\left(\frac{n_0}{n_1}\sin\theta_i\right)\right]\right\} + \alpha\right)\right]$$

Note that this result can also be obtained by simply substituting θ_i by $-\theta_i$ and θ_o by $-\theta_o$ in equation (3.3). The sign merely indicates at which side of the substrate normal the beam is propagating.

The influence of this sign change on the deflection angle is small, as figure A.2 illustrates. Note that in figure A.2, the refractive indices of the substrate and the liquid crystal are the same as those in figure 3.3, so that the two figures can be compared easily. The angle of incidence, θ_i, in both figures is positive, but has a different meaning though: in figure A.2, the ray is incident from the upper left quadrant, whereas in figure 3.3 it is incident from the upper right quadrant of the figure.

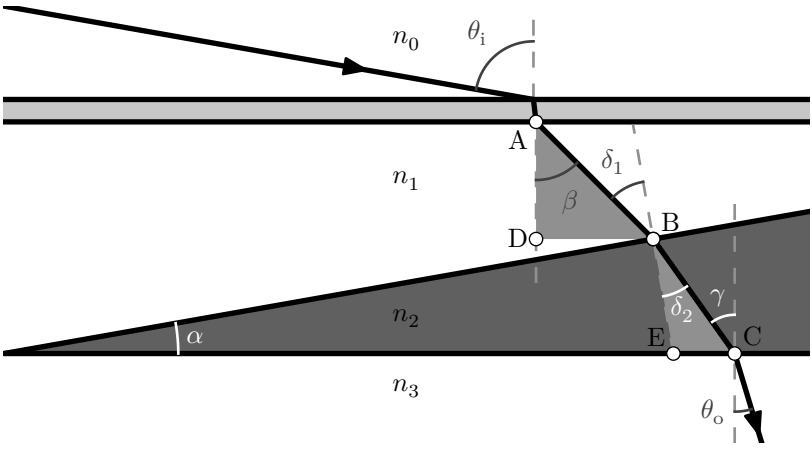

Fig. A.1: Ray diagram showing the transmission of a beam of light through a structure with an inner wedge.

Two differences stand out when comparing the first two columns of both figures: the first is that $\Delta\theta_o$ has obtained a negative sign. Given the definition of $\Delta\theta_o$ in equation (3.4), a positive value means that a ray emerging from the device will be directed at an angle, measured from the substrate normal, that is larger when the ray experiences the extraordinary refractive index of the LC than when the ray experiences the ordinary refractive index. The appearance of the minus signs to the deflection angles in figure A.2, compared to figure 3.3, therefor only indicates that the orientation sense is preserved when the experienced refractive index of the liquid crystal changes from n_e to n_o, no matter if the ray emerges to the left of the substrate normal or to the right.

The second observable difference between the two left columns of figure A.2 and figure 3.3 is that when light is incident to the device from the left of the upper device normal, the influence of the angle of incidence is slightly reduced.

Because there is only a sign change when considering light incident from the left of the upper substrate normal, and that sign change only indicates the direction from which light is coming relative to the normal or into which direction light is propagating after emerging from the device, only positive values of θ_i are considered in section 3.1.

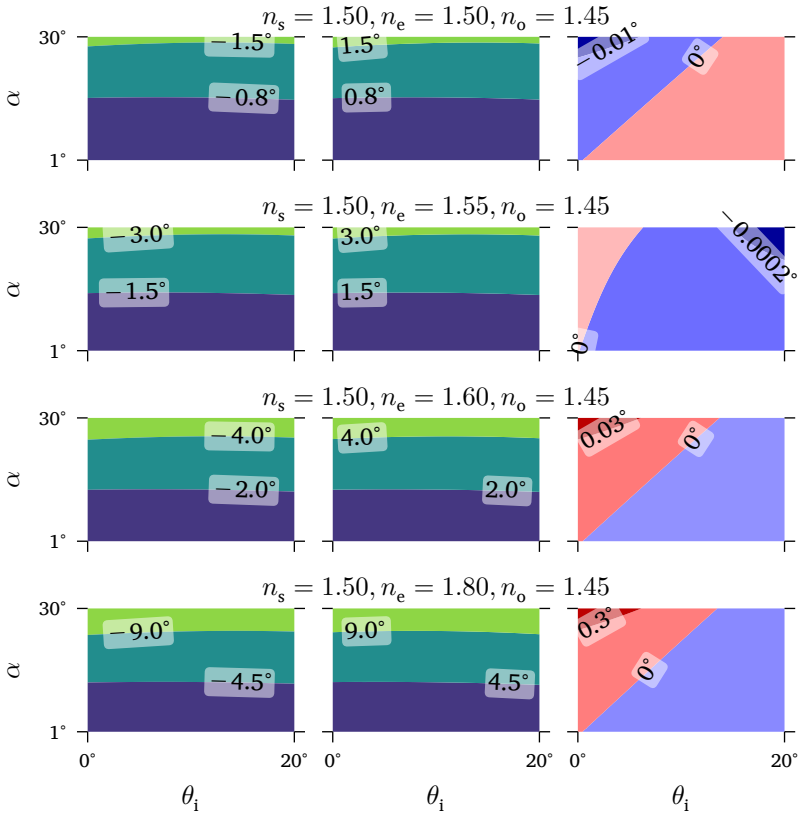

Fig. A.2: Comparison of the achievable deflection angle between the situation where light travels from the LC to the grating substrate (left column: $\Delta\theta_o^{LC\to s}$) and vice versa (middle column: $\Delta\theta_o^{s\to LC}$). The column to the right shows $|\Delta\theta_o^{LC\to s}| - |\Delta\theta_o^{s\to LC}|$, with negative values indicated in blue, positive values in red. The figure differs from figure 3.3, because the light ray here is incident from the left of the upper substrate normal.